Università degli Studi di Napoli *Federico II*

DOTTORATO DI RICERCA IN
FISICA FONDAMENTALE ED APPLICATA

Ciclo XXVII
Coordinatore: Prof. R. Velotta

Primary mass discrimination with the Auger Experiment: the energy spectrum of light elements.

Settore Scientifico Disciplinare FIS/01

Dottorando:
Roberta Colalillo

Tutor:
Dr. F. Guarino

Anni 2012/2015

Contents

Introduction

The main aim of this PhD thesis is the measurement of the energy spectrum of light cosmic rays primaries at the energies of interest for the Pierre Auger Observatory. The Observatory is located near Malargüe, Argentina, and consists of a surface detector array (SD) of 1660 water Cherenkov stations spread over an area of 3000 km^2 and overlooked by 27 air fluorescence telescopes (FD). The combined use of these two detectors allows to study different aspects of the extensive air showers produced by the interaction of cosmic ray (CR) primaries with the atmosphere. In particular, the FD observes the longitudinal profile of the showers, while the SD is sensitive to the distribution of shower particles at the ground.
Studying the all particle cosmic ray energy spectrum, the Auger Observatory has observed clearly both the ankle at $10^{18.7}$ eV and the strong flux suppression at the highest energies. However with present data it is not yet possible to tell if the suppression is related to the lack of sources which are able to accelerate CR up to these energies or to the loss of energy due to interaction of cosmic rays with CMB (GZK effect). The information on the energy-dependent elemental composition of cosmic rays is one of the most fundamental inputs needed to distinguish among different classes of theories and models, which start from different assumptions. This task is particularly difficult, since the development of the extensive air showers is strictly related to the hadronic cross sections, that cannot be measured at the Auger Observatory energies, but only extrapolated from the accelerators measurements at lower energies.
For the determination of the energy spectrum of light elements, I used hybrid showers, i.e. showers measured by at least one fluorescence detector and one SD station, collected by the Pierre Auger Observatory from January 2004 to December 2013. The light elements, protons and helium nuclei, were selected with a cut in the depth of shower maximum, X_{max}, that is very sensitive to mass composition. Showers initiated by light primaries develop more deeply in the atmosphere, so I established the cut selecting the 20% of the deepest showers in X_{max} distributions of CONEX proton-induced showers. The showers used to optimize the cut were simulated at fixed time, while for the exposure calculation we need time dependent simulations that take into account the changes in the detector configurations and in the boundary con-

ditions that affect the data taking. At the highest energies, the statistics of hybrid events is low, moreover the X_{max} cut by definition selects only up to 20% of the events, so in the last part of the light energy spectrum (E>10^{19} eV) the fluctuations are very large and the details of the spectrum shape cannot be easily measured. Details are given in the third chapter.
The surface detector has a 100% duty cicle, while it is about 15% for the fluorescence detector, so the statistics of SD events is higher. I tried to reconstruct the light spectrum using the SD data and the universality concept. The *Shower Universality* states that the general features of an air shower are determined by only a few measurable quantities despite the very large number of particles it contains and the vast number of different interactions to which these particles are exposed. Several universality models of the signal in the water Cherenkov detectors have been developed in the Collaboration, and thanks to these models it is possible to estimate the X_{max} for SD events with energies above $10^{18.8}$ eV. Therefore, in principle, an SD light energy spectrum can be reconstructed at the highest energies with the same method used for the hybrid light spectrum. A first application of this technique is described in the fourth chapter.
In addition to X_{max}, the muonic component of the showers and the depth of the maximum of the muon production depth (MPD) distribution are very sensitive variables to mass composition. Present Auger SD stations are sensitive to the muonic component, but they do not provide a direct measurement of the muons, so the Auger Collaboration is defining a detector upgrade to achieve a reliable direct measurement of this component.
Another goal of my PhD work was to define the requirements to the muon detector in terms of sampling area, time resolution and dynamics. I performed a study on CORSIKA showers to estimate the time resolution required for an accurate MPD reconstruction taking into account all the detector effects and experimental uncertainties. Moreover, I studied the performances of two muon detector layouts proposed by the Auger Collaboration for the upgrade in the discrimination between proton and iron primaries and in the search for photon primaries using the measured muonic component. The analyses are described in the fifth chapter.
Both these simulation studies for the upgrade and the SD universality analysis make extensive use of simulated showers. During this work a large library of CORSIKA showers and fully simulated events in the detector with various versions of the Auger Collaboration Offline software has been developed and made available to the whole Collaboration.

Chapter 1

Cosmic Rays

Cosmic rays are particles coming from the outer space that continuously hit the Earth [1, 2]. They were discovered by Victor Hesse in 1912. During several ascends with hydrogen-filled balloons up to altitudes of 5 km, he found an increase of ionizing radiation with increasing height and he concluded that this radiation penetrates from outer space into the atmosphere. In 1930, Pierre Auger discovered the Extensive Air Showers (EAS) produced by the interaction of cosmic rays with the Earth atmosphere using Wilson chambers and Geiger–Müller tubes separated by large distances and operated in coincidence. On February 22, 1962, at Volcano Ranch, an array of particle detectors in New Mexico, Linsley observed the first air shower with an energy greater than 10^{20} eV.
In its early years, particle physics was practiced primarily through the study of cosmic rays. Positrons, muons, pions, kaons, and so on were discovered observing cosmic rays. Today we have the large accelerators, but the most powerful accelerator, LHC, reaches the maximum energy of 10^{17} eV in the laboratory frame. This energy is several orders of magnitude lower than that of the most energetic cosmic ray. So, the Ultra High Energy Cosmic Rays (UHECR - E$>10^{14}$ eV) are very important to understand physics beyond the Standard Model. Moreover, a lot of things are known about cosmic rays at lower energies, but the origin and composition of the UHECRs are an opened chapter yet.

1.1 The Cosmic Ray Energy Spectrum

The cosmic ray energies extend from the MeV range to at least 10^{20} eV. The differential energy spectrum of all cosmic-ray particles is depicted in fig. 1.1. It falls steeply as function of energy. The cosmic ray flux decreases from more than 1000 particles per second and square meter at GeV energies to about one particle per m^2 and per year at a PeV, and further to less than

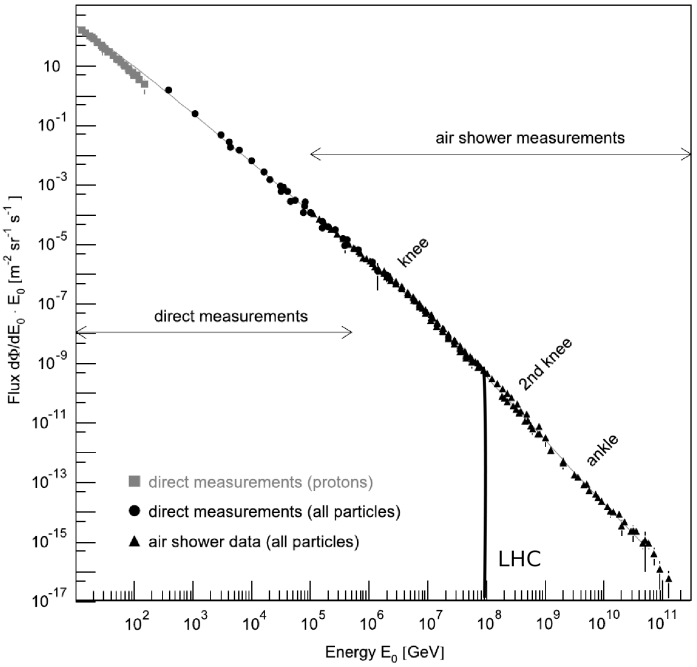

Figure 1.1: Energy spectrum of cosmic rays. The vertical black line indicates the maximum energy reached by LHC.

one particle per km^2 and per century above 100 EeV. It follows a power law

$$\frac{dN}{dE} \propto E^{\gamma}$$

over a wide energy range, indicating non-thermal acceleration processes. The spectrum shows several features which correspond to a change in the spectral index γ. The spectral index is $\gamma \approx -2.7$ at energies up to around 3 $\times$ 10^{15} eV, where the *knee* is observed. Until the *second knee*, that occurs at around 4 $\times$ 10^{17} eV, $\gamma \approx -3$. Below the energy of the *ankle*, E $\approx$ 4 $\times$ 10^{17}, $\gamma \approx -3.2$; above the *ankle*, the spectrum again becomes harder, and a suppression of the flux is observed above 5 $\times$ 10^{19} eV [3]. At low energies, cosmic rays have been studying since their discovery using detectors placed on air balloons and satellites, and thanks to the high statistics, their origin and composition are known. But at higher energies (E $>$ 10^{14} eV), the flux is too low and cosmic rays can be only detected indirectly, studying the EAS. The secondary particles that form the shower are detected by large detectors located at ground. Information about the particle which initiated the shower, called primary cosmic ray, must be reconstructed. The development of the shower is strictly related to the hadronic cross sections, that at these energies cannot be measured, but only extrapoleted by the measurements at lower energies, so it is very difficult to interpret the UHECR observa-

tions. Understanding the origin of the characteristic features of the cosmic ray flux is a key to identify their galactic and extragalactic sources and the corresponding particle acceleration and propagation mechanisms. The knee could stems from features of diffusive shock-acceleration processes, and, in this case, the fluxes of individual elements should exhibit knee-like features that are shifted in energy according to magnetic rigidity, E/Z. In contrast, particle physics scenarios lead to a scaling with mass number E/A. The ankle is often interpreted as the transition between galactic and extragalactic sources, but can be also seen as the imprint of e^+e^- pair production. The suppression of the flux at high energies, instead, can be related to the GZK effect or to the the maximum energy at which particles are injected. Information on the energy-dependent elemental composition of cosmic rays is one of the most fundamental inputs needed to distinguish among these different classes of theories and models, which start from different assumptions. In the following, we will analyze some of these models to see the effect that the different assumptions have on the interpretation of the Auger cosmic ray spectrum and on mass composition.

- **Maximum-energy scenario:** it assumes that the maximum energy at which the particles can be accelerated from the sources is proportional to their charge, so the proton component around $10^{18.5}$ eV is naturally related to similar components of heavier elements, each shifted in energy by the charge number Z [4, 5]. The upper end of the all-particle spectrum would then be dominated by heavy elements of the iron group and the observed suppression would be caused by the cutoff of the source spectrum (assumed to be exponential) rather than energy loss processes during propagation. The mass composition is assumed similar to that of Galactic cosmic rays with fluxes having the same spectral index in energy per nucleon and an enhancement of heavy elements. Moreover, according to this model, the protons in the energy range of the ankle are injected by the same extragalactic sources that also produce the flux at the highest energies.

- **Photo-disintegration scenario:** assuming that the sources accelerate nuclei to a maximum energy above the energy threshold for photo-disintegration, the light elements could then be fragments of heavier nuclei that disintegrated during propagation and the suppression of the all-particle flux could be originated mainly from photo-disintegration processes, which cause energy loss. Lighter elements appear at energies shifted by the ratio of the daughter to parent mass numbers [6, 7]. Again the protons at the ankle energy are naturally linked to the particles at the highest energy of the spectrum and are of extragalactic origin.

- **Proton-dominance model:** this model, called also dip model, is the

model that interpret the ankle as the imprint of e^+e^- pair production in extragalactic propagation [8, 9]. In it, the all-particle flux consists mainly of extragalactic protons at all energies higher than 10^{18} eV and the suppression is attributed to pion-photoproduction (GZK effect).

Fig. 1.2 shows possible descriptions of the latest Auger flux data [83] within the maximum-energy and photodisintegration models. Different fluxes of several mass groups are requested to describe the spectrum and the kwnoledge of cosmic ray mass composition could help to distinguish between these two models.

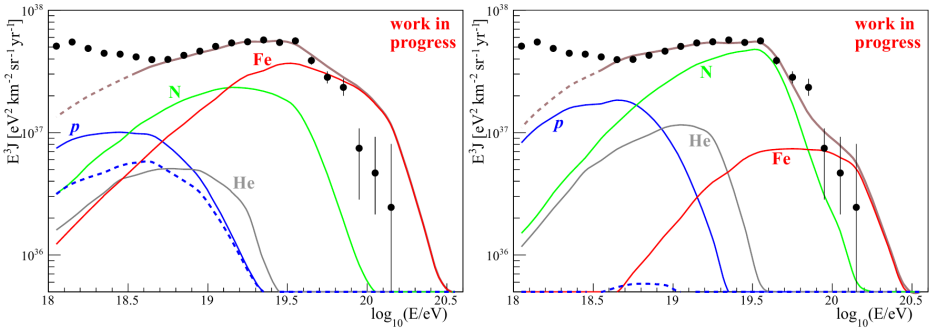

Figure 1.2: Fluxes of different mass groups for describing the Auger spectrum. Shown are the fluxes of different mass groups based on the maximum-energy scenario (left panel) and on the photo-disintegration scenario (right panel). The blue dashed line shows the flux of protons originating directly from the source. The difference between the solid and dashed blue curves corresponds to protons produced due to nuclear disintegration.

1.2 Composition of the UHECR

At the lowest energies starting in the MeV range, cosmic rays are produced within the solar system. The flux is strongly dominated by proton and helium, although all isotopes of the periodic table up to uranium have been measured. Abundances as obtained by several experiments at about 1 GeV/n compared with the abundance of elements in the solar system are depicted in fig. 1.3. The two distributions look very alike. The differences that exist reveal information about the acceleration and propagation of cosmic rays. The light elements lithium, beryllium, and boron, as well as the elements below iron (Z = 26) and below lead (Z = 82), are more abundant in cosmic rays than in the solar system. They are assumed to be produced in spallation processes of the more abundant particles of the CNO, iron, and lead groups during the journey of cosmic rays through the Galaxy.
At higher energies (E>10^{14} eV) cosmic rays are of galactic or extragalactic origin and their mass composition is unknown. The interpretation of data is related to the hadronic interaction models used to simulate the extensive

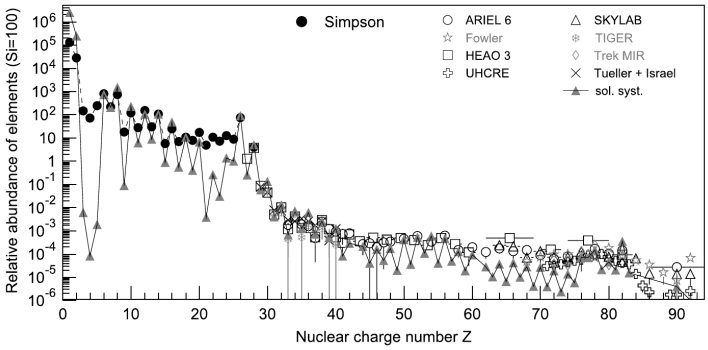

Figure 1.3: Abundance of elements in cosmic rays as a function of their nuclear charge number Z at energies around 1 GeV/n, normalized to Si = 100. It is compatible with the abundance of elements in the solar system.

air showers. Variables sensitive to the mass composition, as we will see in section 1.7, are, for example, the number of electrons and muons in a shower. The KASKADE collaboration measured the energy spectra of individual elements, and to distinguish among showers initiated by different elements, established cuts on simulated showers using these two variables. Fig. 1.4 shows as the obtained spectra, so the mass composition, are different changing the hadronic model used to simulate the showers.

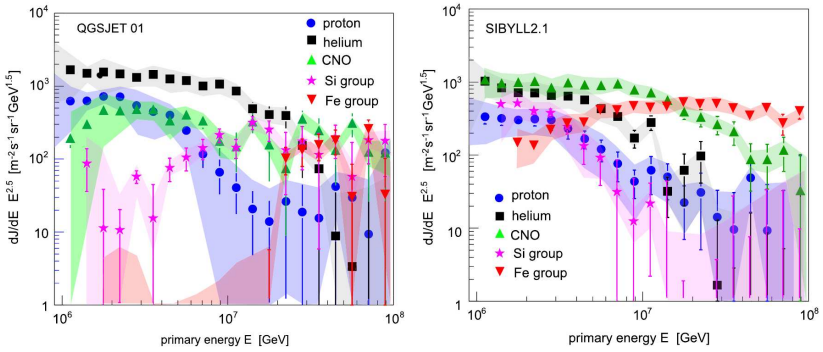

Figure 1.4: Cosmic-ray energy spectrum for five groups of elements as reconstructed by the KASCADE experiment using the hadronic interaction models QGSJET 01 (left) and SIBYLL 2.1 (right) to interpret the measured data [10].

Another variable very sensitive to the primary mass is the depth of shower maximum, X_{max}, and several experiments use the mean value of X_{max} as function of primary energy, called elongation rate, to study mass composition. In fig. 1.5 the elongation rates measured by HiRes, Telescope Array, Auger and Yakutsk around and above the ankle are shown. The measurements from Yakutsk, HiRes and TA experiments are consistent with the

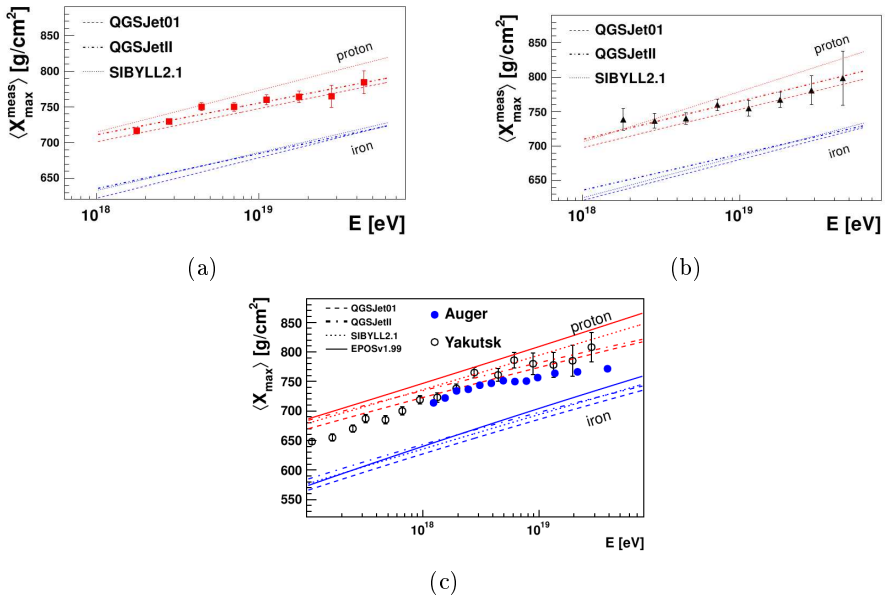

Figure 1.5: Elongation rate measured by HiRes (a), Telescope Array (b), Auger and Yakutsk (c) [11].

QGSJet predictions for a constant proton composition at all energies above 10^{18} eV, whereas the Xmax measurements from the Pierre Auger Observatory are significantly shallower than these predictions above a few EeV. The Auger measurements suggest a heavier composition at energies above 10^{19} eV.

1.2.1 Photons

Photons are also possible primary cosmic messengers in the flux of particles with energy larger than 10^{18} eV. They are not deflected in magnetic fields, so the study of UHE photons is important in searching for astronomical sources, and the presence or lack of UHE photons could have an impact on the measurements of the energy spectrum, cross sections, mass composition of cosmic rays, and on fundamental physical processes. Moreover, the observation of GZK photons is important to constrain several models that start from different assumptions on cosmic rays sources, mass composition, and so on. More details will be given in section 1.6.

1.3 Cosmic Ray Sources

The sources of charged particles are divided in two classes of models. The first are *bottom-up* scenarios where charged particles are accelerated continuously from rest within a small region of space. The Hillas plot [12], depicted

in fig. 1.6, shows possible sources of cosmic rays as function of the size of the source and its magnetic field. The maximum energy E_{max} a particle can

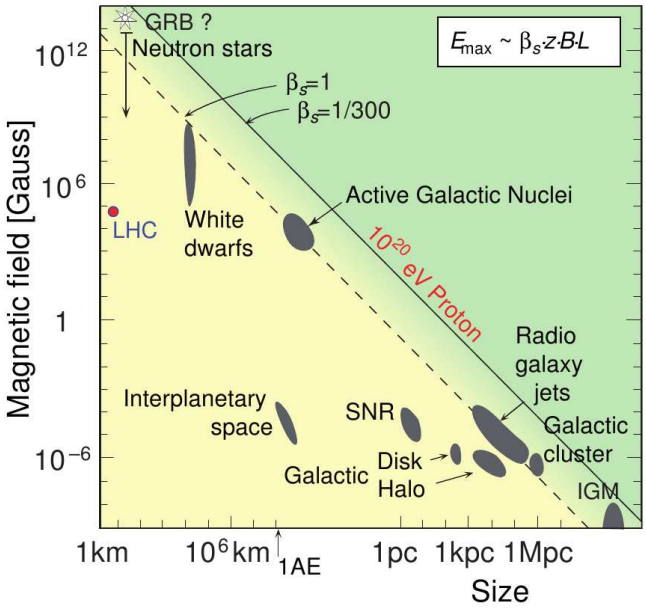

Figure 1.6: Hillas plot shows possible sources for the acceleration of UHECR. Objects below the solid (dashed) line are not able to accelerate protons (iron nuclei) up to 10^{20} eV.

attain in the source is given by:

$$E_{max} \simeq 10^{18} eV \cdot Z\left(\frac{R}{kpc}\right)\left(\frac{B}{\mu G}\right)$$

where Z is the charge of the particle, B is the magnetic field strength, R the size of the accelerating region.
Galactic supernova explosions are very good candidates for the acceleration of cosmic rays up to the knee region. Particles from the interstellar medium gain energy by repeated reflection from the front and back surfaces of the expanding shell of the supernova remnant. The acceleration mechanism will be explained better in section 1.4. With increasing number of reflections and therefore with increasing energy, a particle is more probable to leave the acceleration site. The achievable energy in this process is limited by the lifetime of the shell ($\approx 10^5$ years) and by its size. Common supernova remnants can provide energies up to 10^{15} eV. If the matter density is high enough and the amplification of the magnetic field in the shock by cosmic rays is taken into account, even maximum energies up to 10^{17} eV are possible.
Once a particle leaves the acceleration site, it is deflected by the galactic magnetic field. This means that cosmic rays cannot be traced to their sources

at these energies and an isotropic flux is observed. The radius of the circular motion of a charged particle with mass m and charge q in a magnetic field, called *Larmor radius*, is given by:

$$r_L = \frac{mv_\perp}{|q|B},$$

where B is the magnetic field strength and $v_\perp$, the component of the particle velocity orthogonal to the magnetic field. For protons in the galactic magnetic field this reads as:

$$r_L = 1.08pc\frac{E/PeV}{Z \cdot B/\mu G}.$$

With increasing rigidity ($\propto$ E/Z), the Larmor radius exceeds the size of the galaxy and the particles can no longer be confined. The first particles to escape from the galaxy are protons and so on with increasing the charge Z. Above the knee, the Larmor radius becomes larger than the thickness of the galaxy, so the sources of cosmic rays are presumably located outside of our galaxy. In principle, only few astrophysical sources as active galactic nuclei, hot spots of radio-galaxies, gamma ray bursts, and compact objects like neutron stars are capable of accelerating protons and heavy nuclei up to 10^{20} eV. For example, the jets produced by AGNs extend over distances of 1 pc and have magnetic fields of several Gauss. The cores of AGNs are much smaller but have magnetic fields over several thousand Gauss.
The second class of sources are *top-down* scenarios. In these models, cosmic rays are produced in decays of exotic super-heavy particles (at least 10^{23} eV to 10^{24} eV). Candidates can be X bosons predicted by grand unified theories (GUT) [13], relic particles from the inflationary epoch in the expansion of the universe or topological defects [14], super heavy dark matter particles [15] and so on. According to these models, while super-heavy particles decaying to standard model particles, a large number of ultra-high energy photons and neutrinos are produced. So far, no ultra-high energy photons and neutrinos have been detected, and so the *top-down* models are strongly disfavored. The strongest limits on photon search are set by the Pierre Auger Observatory and these limits are shown on the left of fig. 1.7 compared with the results from other experiments and with predictions obtained with different theoretical models. The sensitivity is not sufficient to exclude models that predict photons created by the GZK effect, described in sections 1.5 and 1.6. The limits on neutrino search are shown on the right of fig. 1.7. Auger and Ice Cube put the strongest limits.
Light particles with energies above EeV range are expected to not be largely deflected from their original path by the magnetic field, so they should point back to the source. The Pierre Auger Observatory found an anisotropy in the arrival directions of high energy cosmic rays [19, 20, 21]. Data recorded with the surface detector between 1 January 2004 and 31 December 2009 with

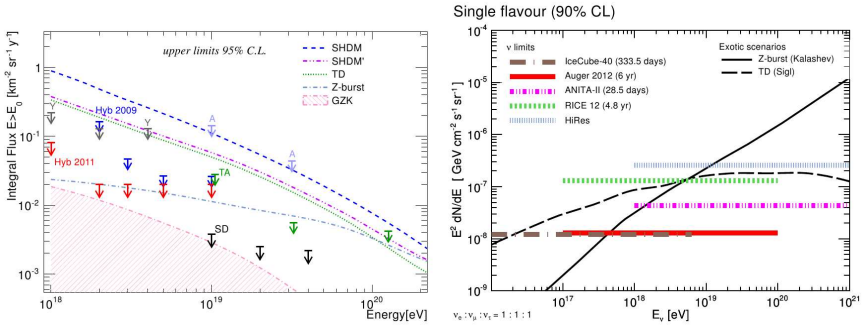

Figure 1.7: Limits on the flux of photons [16, 17] and neutrinos [18] obtained from the Pierre Auger Observatory. The data are shown together with the current limits from other experiments [22, 23, 24, 25, 26, 27] and some examples of predicted fluxes.

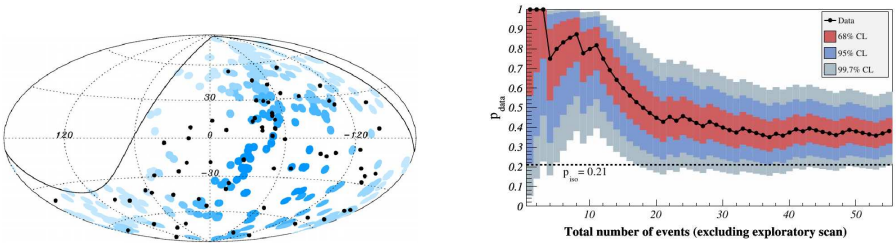

(a) (b)

Figure 1.8: **(a)** The 69 arrival directions of CRs with energy E≥55 EeV detected by the Pierre Auger Observatory up to 31 December 2009 are plotted as black dots in an Aitoff-Hammer projection of the sky in galactic coordinates. The solid line represents the border of the field of view of the Southern Observatory for zenith angles smaller than 60°. Blue circles of radius 3.1° are centred at the positions of the 318 AGNs in the VCV catalog that lie within 75 Mpc and that are within the field of view of the Observatory. Darker blue indicates larger relative exposure. The exposure-weighted fraction of the sky covered by the blue circles is 21%. **(b)** The most likely value of the degree of correlation pdata = k/N is plotted with black dots as a function of the total number of time-ordered events (excluding those in period I - 1 January 2004–26 May 2006). k is the number of correlating arrival directions and N is the number of CRs measured. The 68%, 95% and 99.7% confidence level intervals around the most likely value are shaded. The horizontal dashed line shows the isotropic value $p_{iso} = 0.21$.

zenith angles $\theta \leq 60°$ and reconstructed energy E≥55 EeV were compared with AGNs in the VCV (Veròn-Cetty Veròn) catalog. A cosmic ray is defined as correlated event if its arrival direction is less than 3.1° from the position of an AGN within 75 Mpc. The analysis sample consists of 69 events, while the number of correlated events is 29. All these events are shown on the Aitoff projection map in fig. 1.8 (a). The degree of correlation with objects in the VCV catalog as a function of the total number of time-ordered events observed between May 2006 and December 2009 is shown in fig. 1.8 (b). The horizontal dashed line ($p_{iso} = 0.21$) corresponds to the probability that

an individual event (with E $>$ 55 EeV) coming from an isotropic flux arrives within $\psi_{max} = 3.1°$ and D $<$ 75 Mpc.
The correlation suggests a light mass composition at the highest energies, but this is not necessarily in contradiction to the Xmax measurement (fig. 1.5 (c)), because although the Xmax data suggests a trend to heavier masses, it allows for 10% to 15% protons.

1.4 Cosmic Ray Acceleration

The most popular acceleration mechanism which explains the acceleration of charged particles at very high energy was proposed by Enrico Fermi in 1949 [28]. The original version of Fermi model, known as "second order" Fermi mechanism, is depicted on the left of fig. 3.23. According to this model,

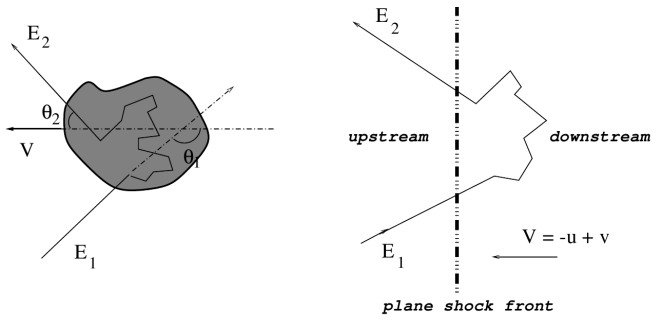

Figure 1.9: Left: acceleration by a moving cloud. Right: acceleration at a plane shock front.

macroscopic kinetic energy of magnetized moving plasma is transferred to individual charged particles. The spectrum obtained after several interactions, because of which the particles gain and lose energy, has a nonthermal energy distribution. A relativistic particle with energy E_1 moving in a cloud of plasma diffuses by scattering on the irregularities of the magnetic field. In the moving gas rest frame the energy of the particle can be written as:

$$E_1' = \gamma E_1(1 - \beta cos(\theta_1)), \tag{1.1}$$

where γ and $\beta \equiv |V|/c$ are the Lorentz factor and velocity of the cloud, respectively. The interaction inside the clouds are elastic, so the energy of the particle before escaping from the cloud is $E_2' = E_1'$, and going back to the laboratory system

$$E_2 = \gamma E_2'(1 + \beta cos(\theta_2')). \tag{1.2}$$

Substituting equation 1.1 into equation 1.2, the relative energy variation ξ due to a single interaction is obtained:

$$\xi = \frac{\Delta E}{E_1} = \frac{1 - \beta cos(\theta_1) + \beta cos(\theta_2') - \beta^2 cos(\theta_1) cos(\theta_2')}{1 - \beta^2} - 1 \tag{1.3}$$

Particles can either gain or lose energy in a given interaction, depending on the angles. By performing the angular averages, the net gain of the processes is:

$$\xi \propto \beta^2.$$

This model can reproduce the power law behaviour of the energy spectrum, but it is a very slow process ($\beta \sim 10^{-2}$) and predicts γ values which are not compatible with the experimental values.
The other Fermi's model, shown on the right of fig. 3.23, is based on large and plane shock wave which propagates with a certain velocity $-u$ through a medium greater than the sound speed in that medium, and which contains a gas of high energy particles. The shocked gas flows away from the shock with velocity v relative to the shock front, and $|v| < |u|$. Thus, in the laboratory frame the gas behind the shock moves to the left with velocity $V = -u + v$. Considering $\beta = |V|/c$ as the velocity of the shocked gas ("downstream") relative to the unshocked gas ("upstream"), the equation 1.3 can be used also in this case to describe the energy variation due to a single crossing the shock. In this configuration, $cos(\theta_2')$ is always positive and $cos(\theta_1)$ is always negative, so angular averaging leads to a "first order" net energy gain for this model:

$$\xi \propto \beta.$$

Before being shocked, particles form a gas isotropically distributed. Some of them pass through the shock front and are isotropised by scattering on the irregularities behind the shock, thus gaining energy. A percent recrosses the shock, being again isotropised by upstream particles gas. This makes this configuration very effective. Also in this case, the model leads to a power law energy spectrum and to a spectral index ≈ -2. A steeper spectrum can result from energy losses and from further modifications to the theory with more realistic assumptions on shock-waves and leakage out of magnetic field confinement.

1.5 Cosmic Ray Propagation

GZK effect

At the highest energies, cosmic rays are expected to interact with the background radiation, mainly with the cosmic microwave background (CMB), infrared background (IR) and radio background (RB). Greisen [29], Zatsepin and Kuzmin [30] predicted that the spectrum of cosmic ray protons would have shown a cutoff at about 5×10^{19} eV due to the photopion production on the CMB. The processes that involve protons are:

$$\begin{aligned} p + \gamma_{CMB} \rightarrow \Delta^+ &\rightarrow p + \pi^0 \\ &\rightarrow n + \pi^+ \end{aligned} \tag{1.4}$$

Their threshold is about 10^{20} eV and the mean free path for a proton of about 10^{20} eV can be estimated as ∼8Mpc. The energy loss per interaction is ∼20%, thus giving an attenuation length of the order of some tenth of Mpc (GZK horizon), beyond which the proton energy falls below the GZK threshold. Therefore, the extreme high energy cosmic rays observed at ground should have been produced and accelerated within a sphere of radius limited by the GZK horizon.

Pair Production

At lower energies, protons interact with CMB by the Bethe-Heitler pair production process:

$$p + \gamma_{CMB} \rightarrow p + e^+ + e^-$$

The threshold of this reaction is $\sim 4.8 \times 10^{17}$ eV. The mean free path is about 1 Gpc and the attenuation length tends to become constant and equal to the energy loss due to the expansion of the universe, ∼4 Gpc.

Propagation of Nuclei

Nuclei of mass A are subject to photo-disintegration and pair production, both on the CMB and on IR:

$$\begin{aligned} A + \gamma_{CMB,IR} &\rightarrow (A-1) + N \\ &\rightarrow (A-2) + 2N \\ &\rightarrow A + e^+ + e^- \end{aligned} \tag{1.5}$$

The photo-disintegration process leads to the ejection of one or several nucleons from the nucleus, but at higher energies, the photo-erosions processes become dominant. One of these, the Giant Dipole Resonance (GDR), with the smallest threshold ($\sim 10^{20}$ eV) leads the emission of one or 2 nucleons and α particles. At energies above $\sim 3 \times 10^{21}$ eV, the photopion production starts to become relevant. The pair production and other processes are negligible on most of the energy range.
The energy threshold of the interaction processes is higher and the attenuation length of nuclei above 10^{19} eV is smaller than that ones for protons. The attenuation lengths for iron nuclei, instead, are similar to protons up to 3×10^{20} eV. But the energy loss processes are different and, because of the ejection of nucleons, a given nucleus does not remain on the same attenuation length during its propagation. According to all these observations and to the known distribution of possible cosmic ray sources, nuclei should not contribute significantly to the high energy spectrum.

Lorentz Invariance

At the highest energies there might be a violation of the strict Lorentz invariance and a term related to this violation would increase the energy threshold

for the formation of the Δ resonance in the GZK processes. The inelastic collisions of nucleons with microwave background photons are suppressed or forbidden, so the UHECR energy spectrum may extend above 10^{20} eV without the predicted GZK cutoff and with the sources of these particles at cosmological distances. But current limits to the photon fraction in the ultra-high energy cosmic ray flux and the observation of the suppression in the energy spectrum at the highest energies by the Auger Collaboration, confirmed also by other experiments, put significantly constraints to the LIV (Lorentz Invariance Violation) dispersion factors.

Photon Propagation

Also the UHE photons, propagating in the interstellar medium, interact with the background radiation. The dominant processes at high energies are the Inverse Compton Scattering (ICS) and the Pair-Production (PP). A $\gamma - ray$, interacting with a CMB or RB γ, produce an electron-positron pair. The energy threshold of this reaction is $E_{th} \simeq 2.6 \times 10^{11} \left(\frac{\epsilon}{eV}\right)^{-1}$ eV, where $\epsilon \leq 10^{-6}$ eV if the interaction is with a γ_{RB} and $\epsilon \sim 10^{-4}$ eV if it is with a γ_{CMB}. Due to this process, photons of energies about 10^{20} eV cannot reach us from distances beyond some tenths of Mpc.
The electrons and positrons produced through PP interactions can lose energy because of the emission of synchrotron radiation while traversing the extra-galactic magnetic fields or via Inverse Compton Scattering (ICS), $e\gamma_{bck} \rightarrow e\gamma$. HE$\gamma$ produced by the ICS process starts a new cycle of PP+ICS and leads to the development of an "electromagnetic cascade". The cascade development accelerates at lower energies, until most of the photons fall below the PP threshold ($Eth \sim 10^{11}$ eV) on the low energy photon background (IR/Optical, $\epsilon \leq 1$ eV). At this point, the interaction between photons and infrared background (IR) dominates, ending up at about 100 GeV, where the photon flux has been constrained by results of EGRET experiment [33].

1.6 GZK Photons

The GZK processes (reactions 1.4) produce a flux of photons in the decay of the neutral pions. Photon energy is about 10% of that of the original nucleon that activated the photopion production. Even if GZK is typically referred to proton interaction models, it is commonly used also for nuclei interacting on CMB. Photons produced during the propagation of nuclei are called “primary photons”. They in turn propagate through the Universe, eventually inducing an electromagnetic cascade. The number of UHE photons produced during nuclei propagation, as well as their production sites and their expected energy spectrum at Earth, depends on the assumptions about the sources. The injection mechanism of nuclei is unknown, as well as the chemical composi-

tion at the source, the relative flux normalization for each primary type, the true distribution of sources and their redshift evolution. In fig. 1.10, several differential photon flux at Earth are shown. The normalization of the fluxes is obtained by scaling the corresponding all-nuclei flux at $10^{18.85}$ eV to the most recent value measured by the Pierre Auger Observatory [83]. The pan-

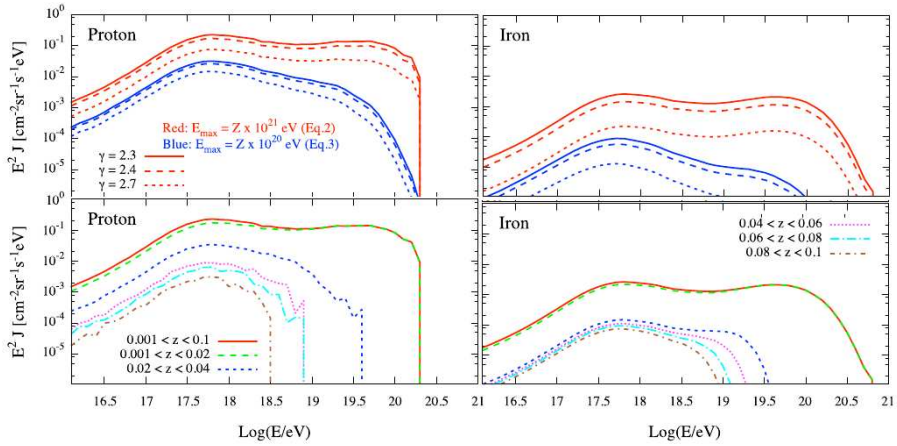

Figure 1.10: Top: Differential photon flux for different spectral indices and for proton and iron. Bottom: Differential photon flux for several distances of the sources of UHECRs [31].

els at the top of the figure 1.10 show the impact of the injection mechanism of UHECRs, varying both the spectral index and the maximum energy at the source. The panels at the bottom, instead, are useful to investigate the impact of the source distance. For both cases, the scenarios with sources accelerating proton and iron were considered. Indicative values for the GZK photon fraction in cosmic rays are between 0.03% and 1-3% at 10^{19} eV, and between few percent to even 50% at 2×10^{20} eV, assuming a proton energy spectrum of index $\gamma = -2.7$ and $\gamma = -1.5$ respectively.

1.7 The Extensive Air Showers

When a cosmic ray enter the Earth's atmosphere, it interacts with a nucleus from the air, mainly nitrogen, oxygen, and argon, at a typical height of 15 to 35 km and produces a shower of secondary particles [32]. Charged and neutral pions are produced in large quantities. Neutral pions ($c\tau$ = 25 nm) immediately decay into two photons, charged pions ($c\tau$ = 7.8 m), instead, interact again forming the hadronic shower core, that consists of longlived secondary hadrons, i.e. baryons, charged pions, and kaons. Finally, charged pions decay into muons and neutrinos ($\pi^{\pm} \rightarrow \mu^{\pm} + \nu_{\mu}/\overline{\nu}_{\mu}$) when $E_{\pi} \leq 30GeV$. Photons from π^0 decay initiate the electromagnetic cascade; moreover produce hadrons or muons through photoproduction or muon pair

production, but these processes are infrequent. The muon component of an air shower, of which 90% is produced by the decays of pions and kaons in the hadronic cascade, propagates through the atmosphere with small energy losses and reaches the surface of the Earth almost unattenuated. For the inclined showers, which are the showers crossing more atmosphere having large zenith angles ($\theta > 60°$), the particles at ground are mostly muons and electromagnetic (EM) particles produced in the decay of muons. These EM particles form the so called "halo". Fig. 1.11 shows an overview of an extensive air shower with its three components: the electromagnetic, the hadronic and the muonic component; while fig. 1.12 shows the distribution of the particles at ground (transverse profile to the shower axis) (left) and along the shower axis (right) for each of these components, simulated with CORSIKA (section 1.9) [34] for proton-induced showers of 10^{19} eV. The

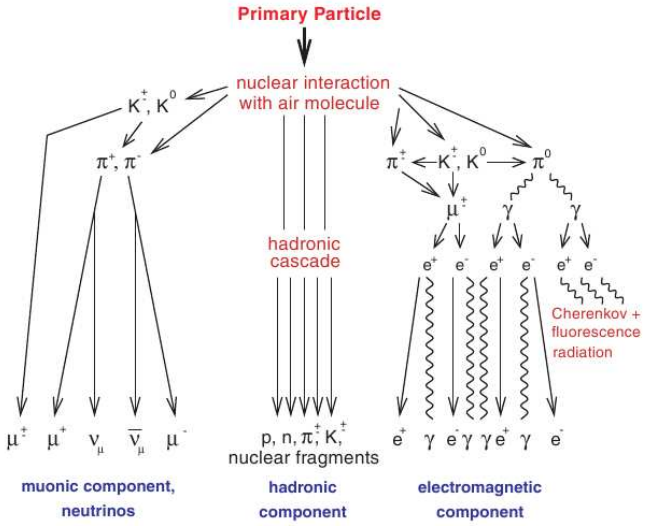

Figure 1.11: Schematic overview of the main components of an EAS.

shower axis indicates the axis of motion of the particle which initiated the shower. The impact point of the shower axis on the ground is called shower core. The shower reaches the ground in the form of a giant "saucer" travelling nearly at the speed of light, that is called shower front. An EAS with its main characteristics is shown in fig. 1.13.
In the following we will study the mainly characteristics of electromagnetic showers and hadronic showers, the latter studied as an extension of the EM ones.

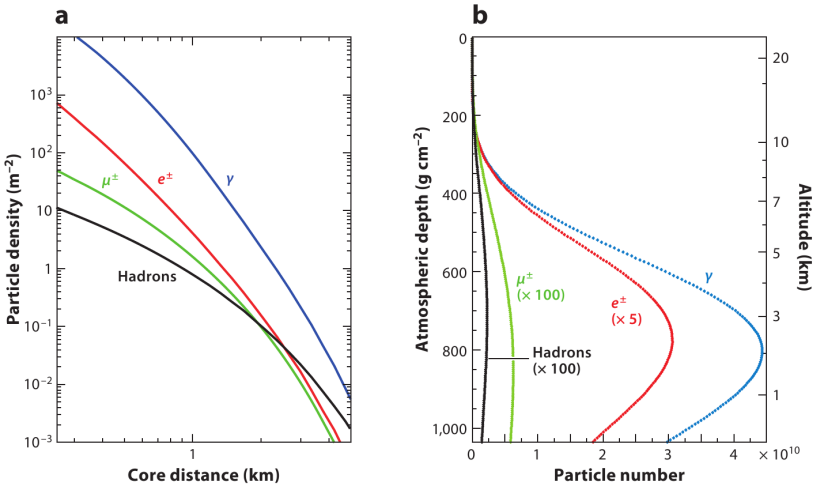

Figure 1.12: Average lateral (a) and longitudinal (b) shower profiles for vertical, proton-induced showers at 10^{19} eV. The lateral distribution of the particles at ground is calculated for 870gcm^{-2}, the depth of the Pierre Auger Observatory.

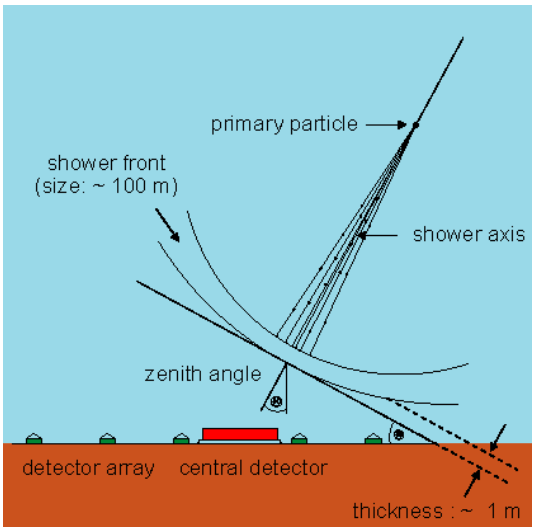

Figure 1.13: Overview of an extensive air shower.

Electromagnetic Showers

The two dominant processes in the development of the electromagnetic cascades are $e^{\pm}$ pair production by photons and bremsstrahlung by $e^{\pm}$. Electrons are also subject to ionization-energy loss. The total energy loss of electrons can be written as

$$dE/dX = -\alpha(E) - E/X_0.$$

X is the traversed column density or slant depth defined as $X = \int \rho(l)dl$, where ρ is the density of air and the integral must be taken along the shower trajectory. $\alpha(E)$ is the ionization-energy loss and X_0 is the radiation length in air ($X_0 \approx 37 g cm^{-2}$). The energy at which energy loss due to ionization equals that due to bremsstrahlung is known as the critical energy and $E_c = 86 MeV$ in air.
An elecromagnetic shower can be described using a simple model, called the Heitler model [35], that is confirmed by cascade theory and detailed numerical simulations. In this model, only one particle type of energy E is considered, and any interaction leads to two new particles with energy E/2. There is an interaction every time the particle has traversed a depth λ_e as shown in fig. 1.14 (a). The number of particles at a given depth, $X = n \cdot \gamma_e$,

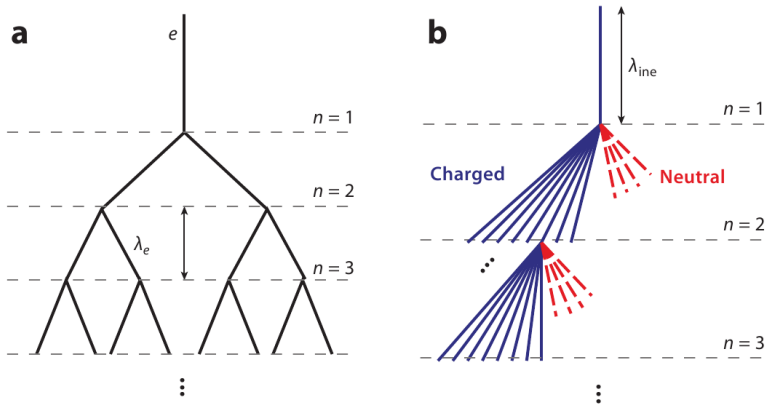

Figure 1.14: Heitler model for the electromagnetic showers (a) and generalized Heitler model for the hadronic showers (b). In this second case, only the hadronic component is shown. Dashed lines represent neutral particles (π^0), and solid lines represent charged particles ($\pi^{\pm}$). Only one charged hadron interaction is shown for each generation.

is related to the number of consecutive interactions or generations, n, using the formula:

$$N(X) = 2^n = 2^{X/\lambda_e}$$

and the energy of a particle of generation n is

$$E(X) = \frac{E_0}{N(X)} = \frac{E_0}{2^{X/\lambda_e}},$$

where E_0 is the energy of the primary particle. The development of the shower continues until ionization-energy losses dominate over radiative losses, so the maximum number of the particles in a shower is reached at $E = E_c$:

$$N_{max} = \frac{E_0}{E_c} \quad \text{and} \quad X_{max}^{EM}(E_0) \sim \lambda_e ln\Big(\frac{E_0}{E_c}\Big)$$

The number of particles is proportional to E_0, while X_{max}, that is the depth at which the shower reaches its maximum development, depends logarithmically on the primary energy E_0.
The lateral spread of the shower particles is related to Multiple Coulomb scattering of electrons off air atoms. It is characterized by the Molière radius:

$$r_1 = \Big(\frac{21MeV}{E_c}\Big)X_0 \approx 9.3gcm^{-2} \approx 80m$$

Another parameter that can describe some features of the EM cascade is the "shower age" s:

$$s = \frac{3X}{X + 2X_{max}}$$

The shower age is defined such that $s = 0$ at the boundary of the atmosphere and $s = 1$ at shower maximum. The number of particles $N(X)$ at a given depth X is described by a Gaisser-Hillas profile:

$$N(X) = N_{max}\Big(\frac{X - X_0}{X_{max} - X_0}\Big)^{\frac{X_{max}-X}{\Lambda}} exp\Big(\frac{X_{max} - X}{\Lambda}\Big)$$

The distribution of the particles at ground is described by:

$$\frac{dN_e}{rdrd\Phi} = C(s)N_e(X)\Big(\frac{r}{r_1}\Big)^{s-2}\Big(1 + \frac{r}{r_1}\Big)^{s-4.5}$$

where $C(s)$ is a normalization constant depending on the shower age and Φ denotes the polar angle in the plane perpendicular to the shower axis.

Hadronic Showers

Hadronic showers are characterized by very complex hadronic multiparticle productions, so it is not possible the derivation of analytic expressions for them, but with the increasing computing power, they can be calculated numerically.
The simple way to describe an hadronic shower comes from the generalization of the Heitler model. The interaction of a hadron with energy E is assumed to produce n_{tot} new particles with energy E/n_{tot} , two-thirds of which are charged particles n_{ch} (charged pions) and one-third of which are neutral particles (neutral pions). The generalized Heitler model, called

Heitler-Matthews model [36], is depicted in fig. 1.14 (b). The neutral particles (π^0) immediately decay into EM particles, that initiate the electromagnetic cascade, instead, the charged particles interact again with air nuclei after traveling the mean hadronic interaction length λ_{ine} if their energy is greater than the typical decay energy E_{dec}. Once the energy of the charged hadrons is smaller than E_{dec}, they decay producing one muon per hadron. After n generations, the energies for hadronic and EM particles are respectively

$$E_{had} = \left(\frac{2}{3}\right)^n E_0 \quad \text{and} \quad E_{EM} = \left[1 - \left(\frac{2}{3}\right)^n\right] E_0$$

With $n \approx 6$, approximately 90% of the initial shower energy is carried by EM particles and deposited as ionization energy in the atmosphere [37] (see fig. 1.12 (b); EM particles outnumber all the other contributions). The depth of the shower maximum of a hadronic shower is expressed by:

$$X^{had}_{max}(E_0) \sim \lambda_{ine} + X^{EM}_{max}[E_0/2n_{tot}] \sim \lambda_{ine} + X_0 ln\left(\frac{E_0}{2n_{tot}E_c}\right)$$

Therefore, a hadronic shower reaches its maximum before than an EM shower with the same energy. The number of electrons at the shower maximum of a hadronic shower corresponds to that of an EM shower with reduced energy, while the number of muons follows from that of charged hadrons:

$$N_\mu = n^n_{ch} = \left(\frac{E_0}{E_{dec}}\right)^\alpha,$$

where $\alpha = \frac{ln(n_{ch})}{ln(n_{tot})} \sim 0.82...0.94$ and it is related to the total particle multiplicities of hadronic interactions. The number of muons is also related to the primary energy and the air density through E_{dec}.
The lateral distribution of a hadronic shower is wider than that one of an EM showers because secondary hadrons are produced at a typical, almost energy-independent transverse momentum $p_\perp \sim 350 - 400MeV$ and this leads to a large angle of low-energy hadrons relative to the shower axis. The lateral distribution of muons is wider than that of EM particles (see fig. 1.12 (a)) because muons are produced mainly in the decay of low-energy pions.

Nuclei and the Superposition Model

In a nucleus, the binding energy per nucleon (~ 5 MeV) is much smaller than the typical interaction energies, so a nucleus of mass A can be approximately considered as A independent nucleons. Follows from this that a shower initiated by a nucleus of mass A is seen as the superposition of A showers initiated by a nucleon with energy $E_h = E_0/A$, where E_0 is the nucleus

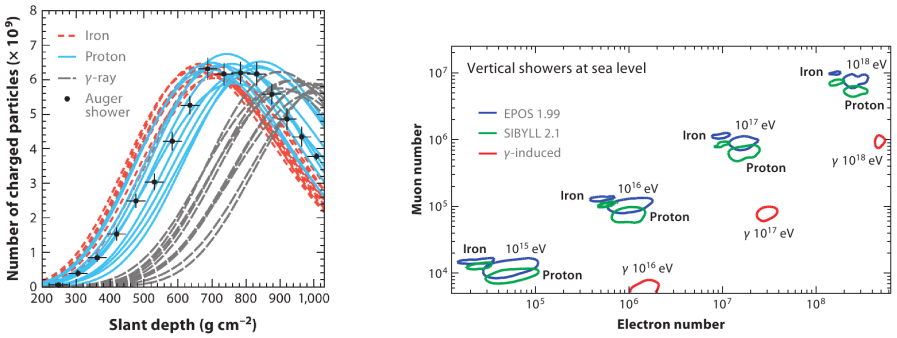

(a) (b)

Figure 1.15: **(a)** Longitudinal shower profiles of 10 proton-, iron-, and photon-induced showers of 10^{19} eV, simulated with SIBYLL. The data points correspond to one shower of approximately the same energy that was measured by the Pierre Auger Observatory. **(b)** Predictions for the correlation between the number of electrons and the number of muons at sea level. The simulations were performed with CORSIKA always for showers of 10^{19} eV.

energy. According to the superposition model:

$$N^{(A)}_{EM,max} = (E_0) = A \cdot N^{(p)}_{EM,max}(E_h) \sim N^{(p)}_{EM,max}(E_0)$$
$$X^{(A)}_{max}(E_0) = X_{max}(^{(p)}E_0/A)$$
$$N^{(A)}_{\mu} = A \cdot \left(\frac{E_0/A}{E_{dec}}\right) = A^{1-\alpha} \cdot N^{(p)}_{\mu}(E_0)$$

The label (p) and (A) are referred to proton- and nucleus-induced showers, respectively.
Heavier the nucleus, more muons are expected for a given primary energy and the depth of shower maximum is shallower. Iron showers contain approximately 40% more muons than proton showers of the same energy, and they reach their maximum 80-100 gcm^{-2} higher in the atmosphere. Moreover, the uncertainty on X_{max} of nucleus-induced showers is smaller than that of proton-induced showers because the first interaction points in the atmosphere fluctuates less. It is averaged over many showers.

1.7.1 Temporal Distribution of Shower Particles

The arrival time of the particles in the shower front is spread out because of geometrical effects, different particle speeds, and delay produced by multiple scattering and geomagnetic deflections. The spread is several hundred nanoseconds at about 100 m from the shower axis and increases with the distance. The core of the shower can be seen as a "fire ball" with a slowly increasing radius, moving at the speed of light. The shower front is slightly curved. Muons are more concentrated in the forward part of the shower

front. They are generally ultra-relativistic and tend to arrive earlier than electromagnetic particles because they suffer much less interactions into the air. The electromagnetic halo can be considered as the result of a diffusive process continously produced from the core. It shows a mean temporal dispersion roughly proportional to the distance from the shower axis. As the shower propagates, the curvature of the shower front and its thickness decrease as shown in fig. 1.16. The accuracy of the shower direction recon-

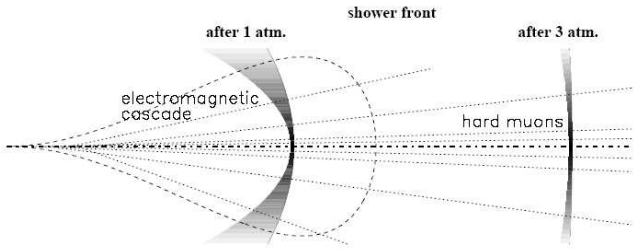

Figure 1.16: Evolution of the shower front shape and thickness during its propagation.

struction is related to the front thickness, so it is important to understand well the temporal development of the shower. It influences also the integration time of the electronics and the method used to record the number of the observed particles. Moreover, as muons arrive at ground earlier, showers initiated by heavier primaries that are richer of muons produce a signal shorter in time, and so the characteristics of the shower front are useful parameters to study cosmic ray mass composition.

1.8 Detection Technique for UHECR

1.8.1 Cherenkov Detectors

Many particles of the shower travel with relativistic velocities through the atmosphere. About one third of the charged particles emit Cherenkov light in the forward direction; the emission angle in air at sea level is only 1.3°. Electrons and positrons are the most abundant charged paticles in air showers and have a low Cherenkov threshold, $\sim$ 21 MeV at the sea level, so they contribute mostly to the Cherenkov light produced by air showers. The Cherenkov ligth is detected with two different techniques: integrating detectors, and imaging detectors or telescopes. They can operate only during clear moon-less nights to obtain reliable data, so their duty cycle is about 10%.
The basic idea of integrating detectors is to measure the lateral distribution of the Cherenkov light with an array of photomultipliers, looking upwards in the sky, distributed over a large area at ground level. To enlarge the collection area, the PMTs are installed inside light collecting cones (Winston

cones). From the Cherenkov measurements, both, energy and mass of the primary particle can be derived. Examples of Cherenkov arrays are AIROBICC [38], BLANCA [39] and TUNKA [40].
The imaging Cherenkov detectors are composed of large area collection mirrors and a camera with segmented read-out. Cosmic-ray events within the field of view of a telescope produce a focal plane image related to the direction and intensity of Cherenkov light coming from the air shower. When the direction of the shower, and so the distance of the shower axis from the telescopes are known, simple geometry can be used to reconstruct the light received from each altitude of the shower. This light is strongly correlated with the number of electrons in the shower, so it is used to estimate the shower size as a function of depth in the atmosphere and the location of the shower maximum. This procedure is essentially geometrical and has the advantage of being almost independent of numerical simulations except for the calculation of the angular distribution of Cherenkov light around the shower axis. Large Cherenkov telescopes are used to reconstruct air showers initiated by primary gamma rays in TeV γ-ray astronomy. The presently largest installations are the H.E.S.S. [41], MAGIC [42], and VERITAS [43] telescopes. The Dual Imaging Cherenkov Experiment (DICE) [44], instead, is optimized for the reconstruction of hadron induced showers, that are background for the γ-ray telescopes.

1.8.2 Fluorescence Detectors

At very high energies (E$\geq 10^{17}$ eV), the more used technique to measure the longitudinal profile of an air shower is based on the fluorescence light. This light is emitted from the de-excitation of the nitrogen molecules of the atmosphere which had been excited by the passage of charged particles of the shower. The fluorescence light spectrum of air is shown on the left of fig. 1.17. The fluorescence yield, that is the number of photons produced per unit

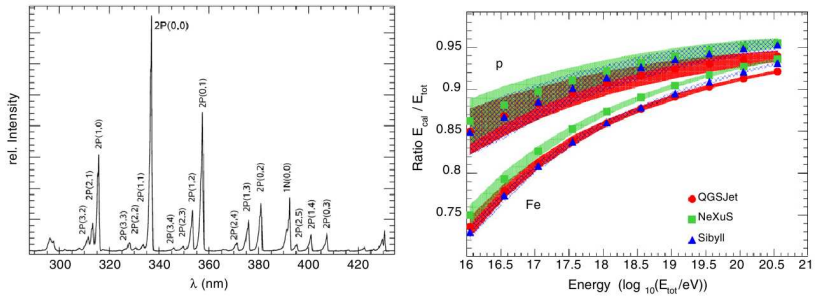

Figure 1.17: Left: The fluorescence light spectrum of air as measured by the AIRFLY experiment [45, 46] with an electron beam of 3 MeV. Right: Ratio of calorimetric to total shower energy [137]. Shown here are predictions calculated with CONEX [47] and different high-energy interaction models. The shaded bands represent 1σ fluctuations.

length, and depends on the gas mixture in the atmosphere and atmospheric conditions, is currently known only to a low precision. But it is independent of the energy of the exciting particle, so if the atmospheric dependence of the fluorescence yield is taken into account, the fluorescence technique allows a calorimetric measurement of the energy deposited in the atmosphere. About 90% of the total shower energy is converted to ionization energy and, hence, is accessible for detection. Fig. 1.17-right shows the average ratio between the energy deposited in the atmosphere and the primary particle energy. It depends on the primary particle type, the energy, and the hadronic model used in the simulations, but, in each case, the most of the shower energy is transferred to EM particles. In the case of a gamma-ray as a primary, about 99% of the energy is deposited in the atmosphere. The determination of the geometry of the shower axis, the determination of the Cherenkov light fraction, and the correction for the wavelength dependent atmospheric absorption of light are also necessary to a complete reconstruction of a shower profile. The Cherenkov light signal of air showers is a highly asymmetric background for the fluorescence light. The Cherenkov light contribution to the detected signal can be estimated using parametrized models that taking into account the electron energy distributions as function of the angular distribution of the emitted Cherenkov ligh. Fluorescence detectors require continuous monitoring of atmospheric conditions, in particular the measurement of the wavelength dependent Mie scattering length, the detection of clouds, and the temporal variations of the density profile of the atmosphere. Photons produced by fluorescence or by Cherenkov mechanisms are scattered by air molecules, *Rayleigh Scattering*, and by small particle in the atmosphere, whose size is comparable to the wavelength of the light itself, *Mie Scattering*. The measured light must be corrected for the attenuation related to these two phenomena. They are sketched in fig. 1.18.

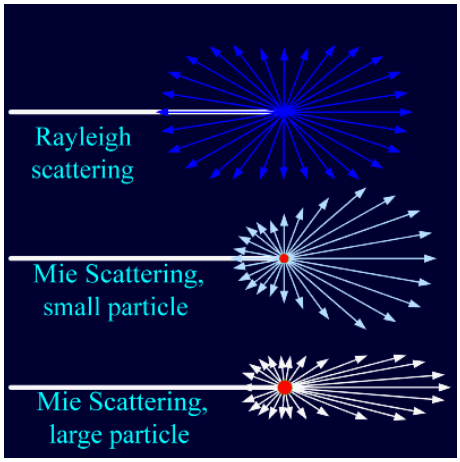

Figure 1.18: Sketch of Raileigh and Mie scattering.

The fluorescence detectors consist of mirrors that collect the light and send out it to an array of photomultipliers. The first experiments to use the fluorescence technique were Fly's Eye [48] and its successor HiRes [49]. Telescope Array (TA) [50] and Auger experiment, that will be described in detail in the next chapter, are using this technique combined with a surface array.

1.8.3 Ground Arrays

The classical set-up to measure the lateral distribution of an EAS is an array of detectors at ground consisting of scintillator or water Cherenkov stations. In each detector the density of charged particles of the shower, that are mainly electrons and positrons at ground, are measured. This measurement allows to reconstruct the position of the shower core and the total number of particles in the shower. From the arrival times of the particles, it is possible to reconstruct the shower axis. Due to the large number of secondary particles, it is usually sufficient to cover only a small fraction of the total area with detectors. Examples of scintillator arrays in the knee region are EAS-TOP [51] and KASKADE [52]. At higher energies, there was AGASA [53] and there are still functioning KASKADE-Grande [54] and TA. The Pierre Auger Observatory, instead, is an example of water Cherenkov array. Various techniques are applied for the detection of muons in air showers. Frequently, particle counters are covered with absorbers of lead, iron, or soil with enough thickness to suppress the electromagnetic component or are located in underground laboratories, well shielded by rock, soil, water, or ice absorbers with a thickness corresponding to several 1000 m w.e (meter water equivalent). But muons can also be identified via their trajectories in tracking devices. The Pierre Auger Collaboration is studying an upgrade of its surface detector to measure the muon component of the shower.

1.9 Monte Carlo Calculations

Corsika is a detailed Monte Carlo program to study the evolution and properties of extensive air showers in the atmosphere. It allows to simulate interactions and decays of nuclei, hadrons, muons, electrons, and photons in the atmosphere up to energies of some 100 EeV and gives type, energy, location, direction and arrival times of all secondary particles that are created in an air shower and pass a selected observation level. As hadronic interaction models are the most uncertain part of CORSIKA, a range of hadronic interaction models is available in the code to allow tests of systematics. Moreover, CORSIKA provides options for production of showers with extreme long CPU times. In the thin-sampling mechanism, only few particles are statistically selected and followed in detail. They represent a large number of particles identified by a weight. In CONEX, instead, the differential cascade equations which describe the shower development after the very first interactions

are solved numerically.
The hadronic multiparticle production is governed by the theory of the strong interaction, the Quantum chromodynamics (QCD). But, even though the LHC measurements have helped to understand better the predictions of QCD, we are still not able to calculate the bulk of particle-production processes at high energy. Therefore, it is necessary to combine results from perturbative QCD and general theoretical constraints with phenomenological modeling to describe multiparticle production at accelerator energies and to make predictions about how to extrapolate the measured distributions into unmeasured phase-space regions and to much higher energies. The most used models in air shower simulations at high energies are the several versions of DPMJET [55, 56], EPOS [57, 58], QGSJET [59, 60, 61], and SIBYLL [62, 63, 64]. They must be complemented with low-energy models that cover interaction energies from the particle-production threshold up to $E \approx 200$ GeV. The most used low-energy models are GHEISHA [65], FLUKA [66], and UrQMD [67]. All these models are based on very similar concepts but differ in the degree of detail in the implementation of these concepts and also in the assumptions that go beyond these common ideas.

Chapter 2

The Pierre Auger Observatory

The Pierre Auger Observatory [68] was designed to study cosmic rays with energies above 10^{17} eV. The main scientific goals of the Auger Project are the discovering of the sources of ultra high energy cosmic rays, the studying of their mass composition and their energy spectrum. The Auger Observatory is located in the Argentinian pampa, near Malargüe (Mendoza) at a mean altitude of 1400 m asl ($\sim$ 880 g/cm^2, that is about the depth of the shower maximum mean value of the showers detected by the Pierre Auger Observatory), it was started in 2002 and completed in 2008, but the data taking started in 2004. It consists of a surface detector array (SD) [69][70] of 1660 water Cherenkov stations, called *tank*, spread over an area of 3000 km^2 and overlooked by 27 air fluorescence telescopes (FD) [71]. Fig. 2.1 shows the planimetry of the Auger Observatory. The black dots represent the ground stations, the blue and orange lines are the view sectors of the fluorescence detector and the red points show sites with specialized equipment. The FD observes the longitudinal profile of the showers, while the SD is sensitive to the distribution of shower particles at ground. The combined use of these two detectors is the main characteristic of the experiment. The surface detector has a 100% duty cycle, but the measurement of the energy of the primary particle is dependent on the hadronic interaction models used to simulate the cosmic ray showers, while the fluorescence detector performs a calorimetric energy measurement weakly dependent on the models. So, thanks to the "hybrid" events, which are the showers detected by at least one surface station and one fluorescence telescope, it is possible to have a calibration of the energy scale for the SD events and accurate measurements of energy and direction of the primary particle. The aperture of the Auger Observatory is the biggest one respect to the other existing experiment and the present exposure is about 30000 km^2 sr yr. Fig. 2.2 shows the Central Campus building in Malargüe from where all data taking and maintenance activities are coordinated and where there are the assembly center and the CDAS (Central Data Acquisition System).

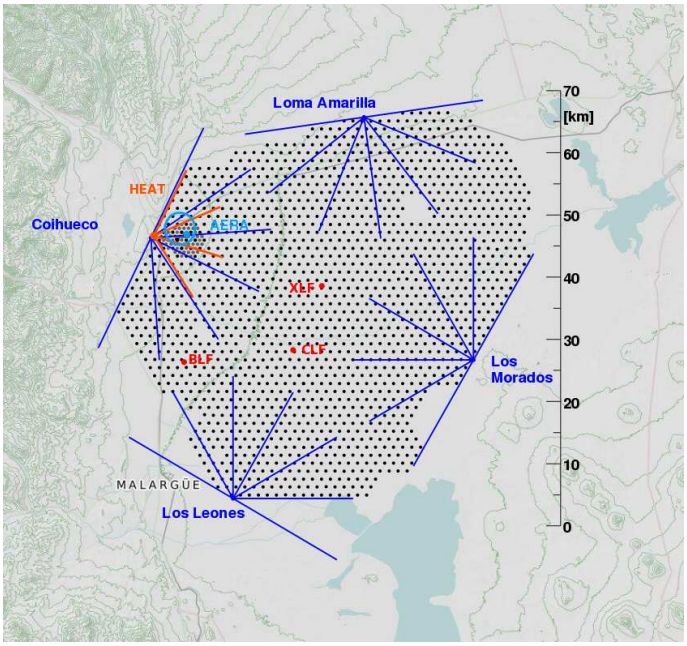

Figure 2.1: Planimetry of the Pierre Auger Observatory.

Figure 2.2: The Central Campus building in Malargüe.

2.1 The Surface Detector

A surface detector meaures the density of secondary particles at ground level with a 100% duty cycle. The Auger SD consists of 1600 water-Cherenkov detectors on a triangular grid of 1.5 km spacing covering an area of approximately 3000 km^2. The water-Cherenkov detector was chosen because of its robustness and low cost. Furthermore, water-Cherenkov detectors exhibit a rather uniform exposure up to large zenithal angles and are sensitive to charged particles as well as to energetic photons. The spacing between the detector stations is the result of a compromise between cost considerations and the energy threshold. The surface detector is fully efficient for energies above 3×10^{18} eV. A SD stations consist of a 3.6 m diameter tank containing a sealed liner with a reflective inner surface. This one is filled with 12000 l of pure water. The shower particles pass through the water and produce Cherenkov light, that is collected by three nine-inch-diameter photomultiplier tubes that are symmetrically distributed at a distance of 1.20 m from the center of the tank and look downwards through windows of clear polyethylene into the water. The station has also a solar power system, which provides an average of 10 Watts for the PMTs, and electronics package consisting of a processor, GPS receiver, radio transceiver and power controller. Fig. 2.3 shows a water-Cherenkov detector. The height

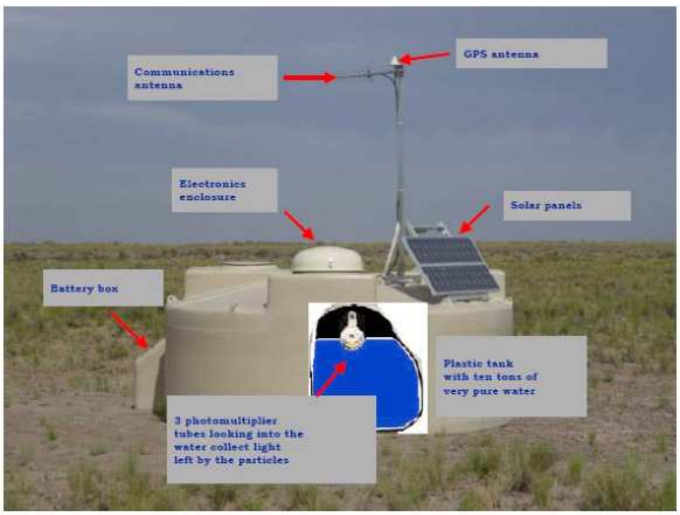

Figure 2.3: A schematic view of a surface detector station in the field, showing its main components.

of the water-Cherenkov detector was chosen to get a clear muon signal and optimize the separation of the muon and electromagnetic contributions to the signal. A vertical height of 1.2 m of water is sufficient to absorb 85% of the incident electromagnetic shower energy at core distances larger than

100 m, and gives a signal proportional to the energy of the electromagnetic component. Muons passing through the tank generate a signal proportional to their geometric path length inside the detector and rather independent of their zenith angle and position.

2.1.1 SD Electronics and Calibration

Each PMT provides two signals, which are digitized by 40 MHz 10-bit Flash Analog to Digital Converters (FADCs). One signal is directly taken from the anode of the PMT, and the other signal is provided by the last dynode, amplified and inverted within the PMT base electronics to a total signal nominally 32 times the anode signal. Two channels are necessary to provide a sufficient dynamic range to cover with good precision both the signals produced in the detectors near the shower core and those produced far from the shower core. When a trigger signal arrives, the information from the three PMTs is sent to the Central Data Acquisition System (CDAS). The total bandwidth used for this purpose is too small to allow a remote calibration, so the calibration of each detector is performed locally and automatically. It relies on the measurement of the average charge collected by a PMT from the Cherenkov light produced by a vertical and central through-going muons, Q_{VEM}. The water-Cherenkov detector in its normal configuration is not able to select only vertical muons, but the distribution of the light of atmospheric muons produces a peak in the charge distribution, Q^{peak}_{VEM} shown in fig. 2.4, and a peak in that of the pulse height, I^{peak}_{VEM}, which are proportional to those produced by a vertical through-going muon. The

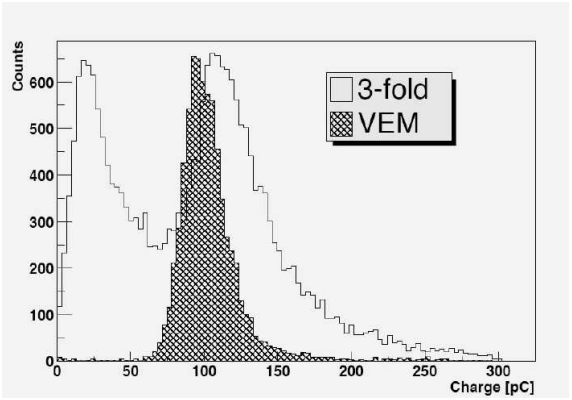

Figure 2.4: Muon peak for surface detector calibration.

value of Q^{peak}_{VEM} must be determined to high accuracy because it provides the unit of measure, called Vertical-Equivalent Muon (VEM), for the signals detected by the surface detector. The gains of each of the three PMTs are tuned to match a reference event rate, so the PMTs in the SD stations

will not have equivalent gains, including PMTs in the same tank. It is also necessary to estimate the dynode/anode ratio to intercalibate the two channels of the PMTs. The calibration parameters are determined with 2% accuracy every 60 s and returned to the CDAS with each event. It contains information about the state of each SD station in the minute preceding the trigger, allowing for an accurate calibration of the data.

2.1.2 SD Triggers

The trigger for the surface detector array is hierarchical. The front-end implements three types of trigger functions. The first two trigger stages are at the station level, instead the T3 trigger, that initiates data acquisition and storage, combines T2 triggers from several stations studying spatial and temporal correlations.

Single Detector Triggers (T1 and T2)

Two independent trigger modes are implemented as T1 in order to detect, in a complementary way, the electromagnetic and muonic components of an air-shower. The first T1 trigger, called single-bin threshold (ST) trigger, requires that the threshold of each PMT will be above 1.75 I_{VEM}^{peak} and it is used to select large signals that are not necessarily spread in time. Very inclined showers that have crossed a large amount of atmosphere and are consequently dominated by the muonic component produce such signals. ST trigger reduces the rate due to atmospheric muons from ≈3 kHz to ≈100 Hz. The second T1 trigger mode, called "Time-over-Threshold" trigger (ToT), allows to select signals from vertical showers, for which the electromagnetic component is dominant and the arrival of particles and photons at the detector is dispersed in time. It requires at least 13 bins (i.e. >325 ns) in 120 FADC bins of a sliding window of 3μs will be above a threshold of 0.2 I_{VEM}^{peak} in coincidence in 2 out of 3 PMTs. Since the average signal duration of a single muon is only about 150 ns, the time spread of the ToT (325 ns) is very efficient at eliminating the random muon background, in fact the ToT rate at each detector is < 2 Hz.
As the total bandwidth available for data transmission from the detectors to the CDAS is only 1200 bits per second, the T2 trigger must reduce the event rate to 20 Hz. All ToT-T1 triggers are promoted to the T2 level, whereas ST-T1 triggers are requested to pass a further higher threshold of 3.2 I_{VEM}^{peak} in coincidence among the three PMTs.

SD T3 Trigger

The third level trigger is formed at the CDAS and it is also realized in two modes. The first mode requires the coincidence of at least three detectors

that have passed the ToT condition arranged in a 3ToT compact configuration, i.e. one of the detectors must have one of its closest neighbours (C1) and another one of its closest neighbours (C1) or one of its second closest neighbours (C2) triggered. An example of this is shown in fig. 2.5 on the left. The rate of this T3 trigger mode with the full array in operation is

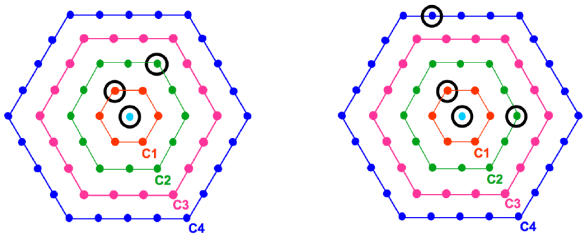

Figure 2.5: Example of T3 configurations: 3ToT on the left and 4T2 on the right. C1, C2, C3, C4 indicate the first, second, third and fourth sets of neighbours, respectively at 1.5, 3, 4.5 and 6 km from a given detector.

around 1600 events per day, meaning that each detector participates in an event about 3 times per day. This trigger is extremely pure since 90% of the selected events are real showers and it is mostly efficient for showers below 60°. For inclined events, instead, the second T3 configuration, called 4T2, is used. It is more permissive and requires a four-fold coincidence of any T2 with a moderate compactness. Among the four fired detectors, within appropriate time windows, at least one must be in the first set of neighbours from a selected station (C1), another one must be in the second set (C2) and the last one can be as far as in the fourth set (C4) as shown in fig. 2.5 on the right. With the full array configuration, this trigger selects about 1200 events per day, out of which about 10% are real showers.
A selection of physics events and of detectors belonging to each event is made after data acquisition. The way to identify real showers with zenithal angle between 0° and 60° is described in the following paragraphs.

Physics trigger - T4

The physics trigger is based on space and time configurations of the detector stations that passed particular trigger conditions. The first configuration making up the T4 trigger is called 3ToT and requires 3 nearby stations, passing the T2-ToT, in a triangular pattern as shown at the top of the fig. 2.6. Moreover, the times of the signals in the 3 stations must fit to a plane shower front moving at the speed of the light. The events passing this trigger level are less than one per day over the full array because of the low rate of T2-ToT trigger. Due to their compactness, events with zenith angles below 60° are selected with high efficiency, i.e. more than 98%.
The second T4 trigger, called 4C1, requires 4 nearby station passed one of

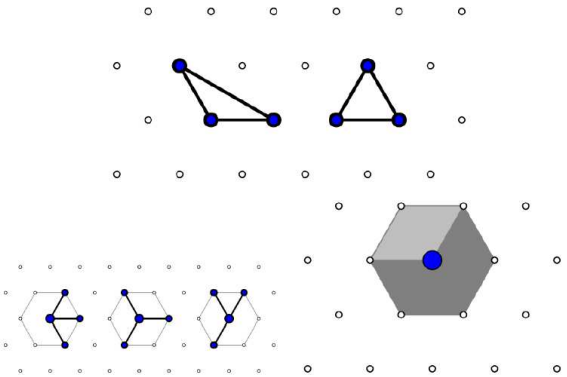

Figure 2.6: Offline SD triggers. Top: triangular configurations required by the 3Tot trigger. Bottom-left: 4C1 compact configurations. Bottom-right: T5 trigger that requires at least 6 active stations around the central one.

the two T2 trigger modes. In this case also, it is required that the times of the signals in the 4 stations fit to a plane shower front moving at the speed of the light. The efficiency for showers below 60° is about 100%. 4C1 configurations are shown at the bottom of the fig. 2.6, on the left. The two T4 criteria are complementary: the 3ToT configuration selects events with a median energy around 6×10^{17} eV and with small zenith angles, while for the 4C1 trigger, the events have a median energy around 3×10^{18} eV and larger zenith angles.

Fiducial trigger - T5

The fiducial trigger T5 requires that the real events passing the T4 level trigger are contained within the array boundaries, ensuring that the shower core, and so the energy, are properly reconstructed. To realize this condition, the detector with the highest signal must have all its 6 closest neighbours working at the time of the event, i.e. it must be surrounded by an hexagon of triggered tank as shown in the lower part of fig. 2.6, on the right. For events passing T5 trigger, the maximum statistical uncertainty in the reconstructed S_{1000} due to event sampling by the array is about 3%. The T5 condition could reject events well contained in the array, but that fall close to a non-working detector. For a detector large as SD Auger detector, about 1% of the detectors are expected to be not functioning at any moment, even with constant detector maintenance, so the request to have a working hexagon reduces the effective area by 10% with respect to the nominal one. Moreover, the SD acceptance saturate above a certain primary energy because of conditions on event containment.
For arrival-direction studies a less strict cut can be used (5T5 or even 4T5).

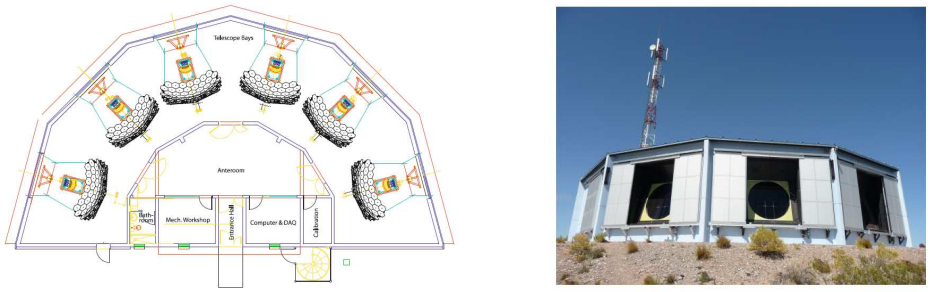

(a) (b)

Figure 2.7: **(a)** Schematic layout of an FD building. **(b)** FD building at Los Leones during day whit shutters opened because of maintenance.

2.2 The Fluorescence Detector

A fluorescence detector measures the longitudinal profile of an air shower in a calorimetric way. The number of emitted fluorescence photons is proportional to the energy deposited in the atmosphere. This measurement is independent of the hadronic models used to describe the development of a shower. The FD is composed of four observation sites, called "eyes". Their names are *Los Leones*, *Los Morados*, *Loma Amarilla*, and *Coiheuco*. They are located on small hills on the perimeter of the SD array. This configuration was optimum to detect showers produced by primaries with energy above 10^{18} eV and to have 100% FD triggering efficiency above 10^{19} eV over the whole area of the surface detector as required by the original project. Each eye consists of six independent telescopes, everyone with field of view (FOV) of $30° \times 30°$ in azimuth and elevation. Fig. 2.7 (a) shows the arrangement of the six telescope in the clean climate-controlled building where they are housed, while FD bulding at Los Leones is displayed in fig. 2.7 (b). The fluorescence detector cannot work during full-moon nights and data taking is stopped for some telescopes when moon light fall into their FOV, so the duty cycle of the fluorescence detector is about 15%.

2.2.1 Optical System

The optical system is composed of a filter at the entrance window of each FD telescope, a circular aperture, a corrector ring, a mirror and a camera with photomultipliers as shown in fig. 2.8. It is based on Schmidt optics to correct spherical aberration and eliminate coma aberration. The size of the aperture is optimized to keep the spot size due to spherical aberration within a diameter of 15 mm, i.e. 90% of the light from a distant point source located anywhere within the FOV of a camera falls into a circle of this diameter. This corresponds to an angular spread of 0.5°. The aperture area of the telescope is almost doubled without modifying the spot size thanks to the introduction

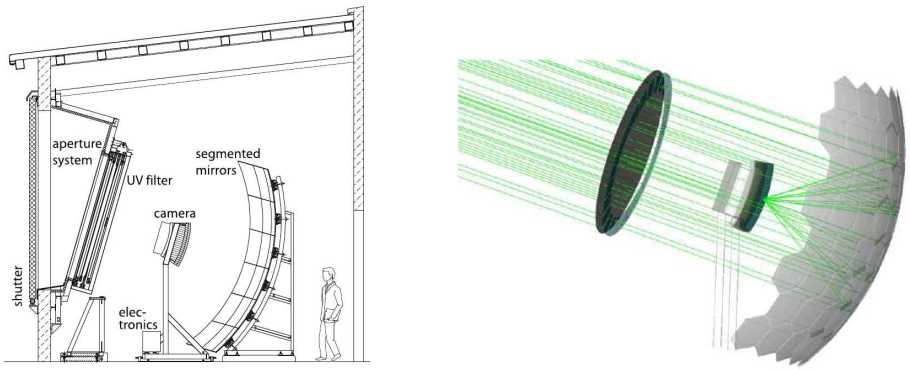

(a) (b)

Figure 2.8: **(a)** Schematiche view of a fluorescence telescope. **(b)** Simulation of the optical system developed using Geant4 [72, 73].

of the corrector ring. It is an annular lens divided in 24 sectors with an inner radius of 850 mm and an outer radius of 1100 mm. The corrector ring further reduces the spherical aberration.
The filter at the entrance window transmits UV photons from ∼290 nm up to ∼410 nm wavelength, that are almost the all wavelenghts of the nitrogen fluorescence spectrum, while absorbs the visible light. The fluorescence light is focused by a spherical mirror. It has an area of about 13 m^2 that is very large, so to reduce the cost and weight of the optical system, it was necessary to segment the mirror. Two different configurations and mirror types are used: a tessellation of 36 rectangular anodized aluminum mirrors for Los Leones and Los Morados, and a structure of 60 hexagonal glass mirrors of four shapes and sizes with vacuum-deposited reflective coatings for Coihueco and Loma Amarilla. For both configurations, the radius of curvature of the mirrors is ∼3400 mm and the average reflectivity of cleaned mirrors at λ=370 nm is more than 90%.

2.2.2 Telescope Camera

The camera is composed of 440 pixels, which are arranged in a matrix of 22 rows by 20 columns, and located on the focal surface of the telescope, that is a sphere of 1.743 m radius. The components of each pixel are a photomultiplier and a light collector. The imprint of a cosmic ray on the camera is a line of activated pixels with a track-like geometrical pattern and a clear time sequence. The pixels are hexagonal with a side to side distance of 45.6 mm, that corresponds to an angular size of 1.5°. The photomultipliers used to instrument the camera are the model XP3062 manufactured by Photonis. Their dependence of the quantum efficiency on the wavelength is shown in fig. 2.9. The nominal gain for standard operation of the FD is set to 5 ×

10^4.

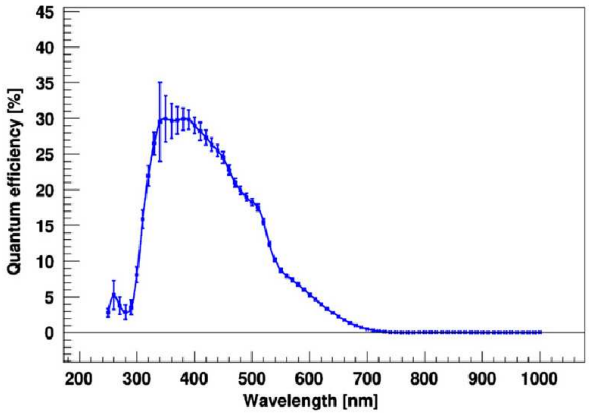

Figure 2.9: The measured dependence of the quantum efficiency on the wavelength of the Photonis XP 3062 photomultiplier unit.

The light collectors serve to prevent photons from landing in the dead spaces between the PMT cathodes. The basic element of the light collector is the *mercedes*, a plastic structure covered by highly reflective material. Each *mercedes* has three arms oriented 120° apart, and is positioned on each pixel vertex as shown in fig. 2.10 (a). The light collection efficiency increases from

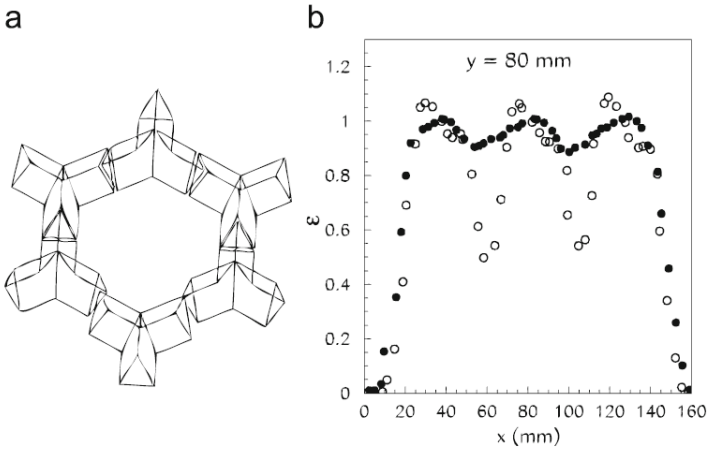

Figure 2.10: **(a)** Light collector realized by six *mercedes* located on the pixel vertexes. **(b)** Measurement of the light collection efficiency for three adjacent pixels. The full (open) dots represent the measurements performed with (without) *mercedes*.

50% to 90% adding mercedes and the transition between adjacent pixels is sharper (fig. 2.10 (b)).

2.2.3 FD Calibration

To recostruct the longitudinal profile of a shower and to determine its total energy, it is necessary to convert ADC counts to a light flux at the telescope aperture for each channel that receives a portion of the signal from a shower. Methods for evaluating the response of each pixel to a given flux of incident photons from the solid angle covered by that pixel, including the effects of aperture projection, optical filter transmittance, reflection at optical surfaces, mirror reflectivity, pixel light collection efficiency and area, cathode quantum efficiency, PMT gain, pre-amplifier and amplifier gains, and digital conversion must be considered. In Auger, a method in which the cumulative effect is measured in a single end-to-end calibration is employed. This is an absolute calibration; moreover relative calibrations, performed each data-taking night, are used to monitor the changes of the detector response as a function of the time.

The Absolute Calibration

The absolute calibration of the FD uses a calibrated light source, called "drum", positioned at the entrance of the telescope under calibration, filling the aperture. The drum, shown in fig 2.11 , consists of a pulsed UV LED, emitting in a narrow band around 365 nm, mounted in a cylindrical shell of Teflon, illuminating the interior of the 2.5 m diameter cylindrical drum, 1.4 m deep. The sides and back surfaces of the drum are lined with Tyvek, while the front face is made of a thin sheet of Teflon, which transmits light diffusively. The drum provides same flux of light to each pixel. The drum

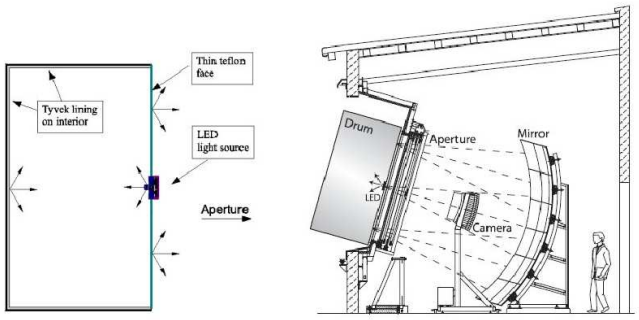

Figure 2.11: Calibrated light source, called "drum", use for the absoulute calibration of the surface detector.

light source intensity is calibrated to a precision of better than 4% in a dark room, using a NIST-calibrated photodiode as a calibration reference. Absolute calibration constants are obtained from the ratio of the known pulsed flux of photons emitted by the drum and the corresponding ADC pulse inte-

grals of the camera pixels. The average response of the FD is approximately 5 photons/ADC bin. Each telescope is drum calibrated once per year. Calibration takes one night per two telescopes, so 3 days per building. The photon flux in photons per m^2 perpendicular to the arrival direction for observed physics events is obtained multiplying the calibration constant by the integrated ADC number and dividing by the area of the aperture.
The telescopes are sensible to different wavelengths, so a xenon flasher is mounted at the back of the drum, with a filter wheel containing 5 notch filters for selection of wavelengths. Relative drum intensity measurements at wavelengths of 320, 337, 355, 380 and 405 nm are performed and combining these measurements with the results from the laboratory, the curve of relative camera response shown in fig. 2.12 is formed.

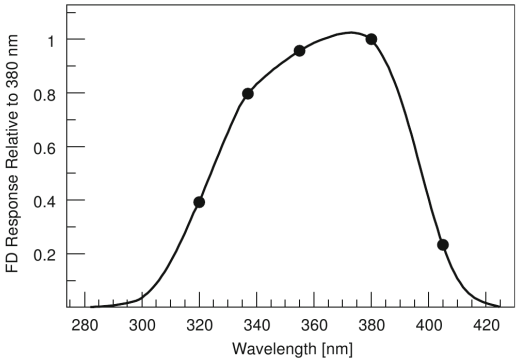

Figure 2.12: The curve of the multi-wavelengths FD camera response.

Another indipendent calibration is sometimes performed using vertical shots from a portable laser in the field. It shots at 337 and 355 nm and, its beam is depolarized, and the pulse-to-pulse intensity monitored to a precision of 5%. The laser is located at a distance of 4 km from the telescope, so the Mie-scattered light is minimized, and the Rayleigh-scattered light is then used to calibrate the fluorescence telescope.

The Relative Calibration

The optical system to monitor the short (daily) and long (seasonal) term changes in detector response consists of three light sources coupled to optical fibers, that distribute light signals to three destinations on each telescope. Fig. 2.13 shows the position of the three light sources. Three calibration steps are performed each night after the data taking, the first step is performed also at the beginning of the night. During this step, called **calibration A**, signals from a pulsed LED light source are brought to a Teflon diffuser at the center of the mirror with the light directed towards

the camera and in this way, the PMT behaviour is monitored. The light source for the **calibration B** is a xenon flash lamp, whose fibers are split near each camera and terminate at 1 mm thick Teflon diffusors located at the sides of the camera, with the light directed at the mirror. The reflectivity of the mirror and the gain of PMTs are checked. Also for the **calibration C**, a xenon flash lamp is used. Signals coming from it are sent to the sides of the entrance aperture where the light is directed toward reflective Tyvek targets mounted on the telescope doors from which it is reflected back into the telescopes to monitor the filter, the mirror, and the camera.

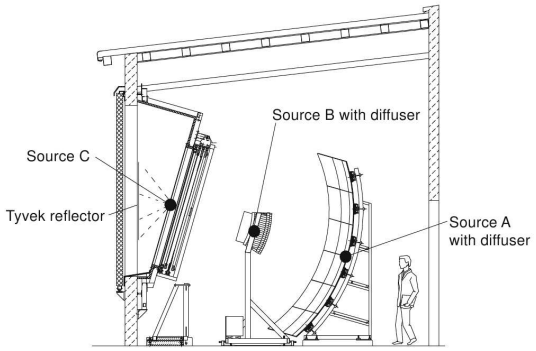

Figure 2.13: Positions of light sources for three different relative calibrations of the telescope.

2.2.4 Electronics and Data Acquisition System

The fluorescence signals have a widely varying intensity and the light background continuously changes so the design of the electronics and data acquisition system (DAQ) of the FD detector must provide a large dynamic range and strong background rejection to accept any physically plausible air shower. Moreover, the DAQ must be suitable to guarantee robust, and low-cost remote operations for the FD telescopes, and the absolute FD-SD timing offset must be sufficiently accurate to enable reliable hybrid reconstruction. The organization of the electronics and DAQ is hierarchical, and it is shown in fig. 2.14 for one FD eye. For each camera, there are a front-end sub-rack and an associated Mirror-PC. The Mirror-PCs are connected with an Eye-PC, which in turn is related to the Observatory Central Data Acquisition System in Malargüe. The FD electronics filters, digitizes, and stores signals from the PMTs. At the end of the process, the data are passed through three trigger stages, and the remaining high-quality shower candidates are collected by an event builder for offline shower reconstruction. For each shower candidate, a trigger is sent online to the CDAS to search coincidences with at least one triggered surface detector station. If there is a

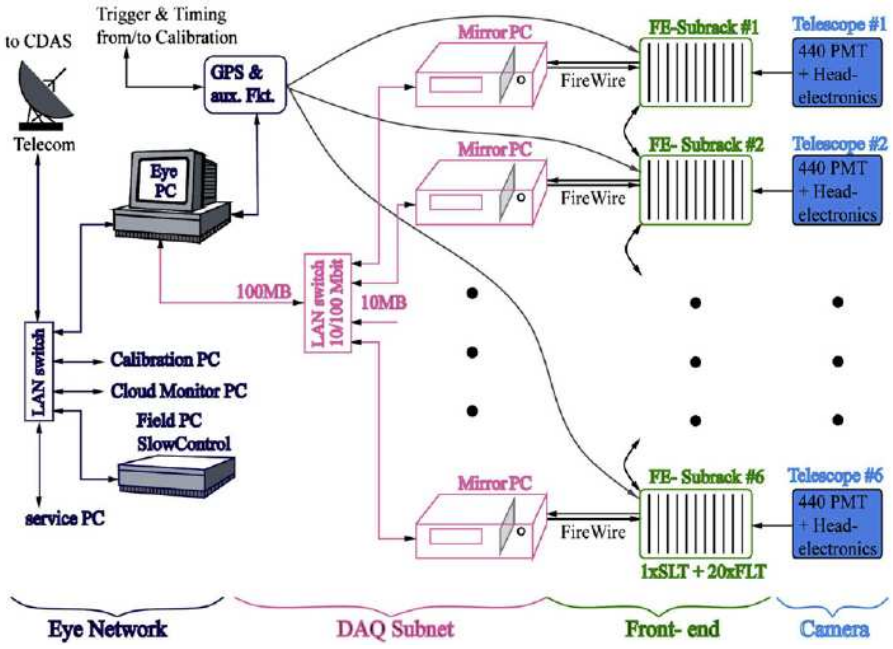

Figure 2.14: Readout scheme of an FD site. The flow of recorded data is right to left.

coincidence, a hybrid trigger is generated and data of even a single station is readout.

2.2.5 FD Trigger

The first two trigger levels are hardware triggers. The First Level Trigger (FLT) checks the intensity of the signal of each pixel, while the Second Level Trigger (SLT) studies particular configurations of pixels which respect the FLT requestes. The last trigger level is a software trigger and it cuts background events that could congest the readout system.

The First Level Trigger (FLT)

The First Level Trigger boards are 20, one for each row of the FD camera and they are contained in the front-end sub-rack. The main task of the functions implemented on these FPGAs is to generate the pixel trigger (FLT) using a threshold cut on the integrated ADC signal. The rate of pixel triggers, called the "hit rate", is measured in parallel by counters for each channel. It is used to adjust the threshold in order to the hit rate is kept constant at 100 Hz under variable background light conditions. The pixel triggers are stored in memory for about 20 μs to be red into the Second Level Trigger (SLT) board. Also the multiplicity, that is the number of pixels triggered simultaneously within 100 ns for each FLT and for the full camera, is stored and

the chronological sequence of multiplicity values carries information about the temporal development of the camera image.

The Second Level Trigger (SLT)

The Second Level Trigger (SLT) board is programmed for track identification within the camera image. If the pattern of triggered pixels follows one of the tracks represented in fig. 2.15 or a their rotation or reflection, an internal trigger is generated. The theoretical algorithm searches for at least five

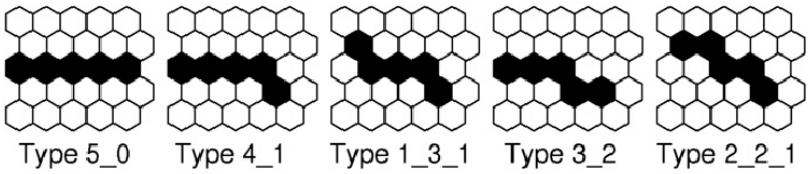

Figure 2.15: The 5 fundamental patterns for the SLT trigger.

aligned pixels, but to take into account contingent hardware problems, i.e. some tracks will not pass through every pixel center, and therefore some PMTs along the track may not record enough light to trigger, also four-fold patterns originating from the five-pixel track segments in fig. 2.15 are accepted. In the end, the evaluated pattern classes are 108. This trigger step produces an event rate contained in the frequency range 0.1-10 Hz. The full scan of the camera lasts 1 μs, and the pixel trigger information scanned during this time is stored in the pixel memory of the SLT. This memory provides complementary information about the spatial and temporal size of the event because also the FLT multiplicities are stored in it.

The Software Trigger (TLT and T3)

When the events passed the first two level triggers reach the Mirror-PCs, they are processed by the software trigger, that is divided in two steps.
The Third Trigger Level (TLT) is optimized for the fast rejection of triggers caused by lightnings, by muons impact on the camera, and by randomly triggered pixels. In good atmospheric conditions, the SLT will detect one to two events per minute per telescope, but, with the lightnings, the rate of events can reach also several 10s of events per second, and if they are not filtered, the 64-event buffers in the FLT and SLT boards will be congested and the dead time of the FD readout will increase. The TLT algorithm reads out only the FLT multiplicities and the total number of triggered pixels and with befitting cuts, rejects approximately 99% of all lightning events during a short decision time of about 50 μs. The fraction of true showers rejected by the trigger is below 0.7%.

Events passing the TLT in each telescope are sent to the EyePC, where an event builder software merges the coincident events from adjacent telescopes and sends an hybrid trigger, called a T3, to the CDAS. The T3 is used as external trigger for the surface detector, that alone does not usually generate an independent trigger at energies below 3×10^{18} eV. At these energies, hybrid events occur within 20 km of the FD buildings and usually do not trigger more than one or two SD stations, but also one station is enough to have an high-quality hybrid reconstruction. The T3 algorithm calculates a preliminary shower direction and ground impact time with a simple online reconstruction. When these data arrive at the CDAS, the signals recorded by the SD stations near the T3 impact time are used for a more detailed reconstruction.

2.3 Enhancement of the Original Detector

After completion of the Observatory, two significant enhancements have been incorporated into baseline detectors to extend the sensitivity down to 10^{17} eV, in keeping with the hybrid detection strategy of the original Observatory. The HEAT (High Elevation Auger Telescopes) fluorescence detectors together with an infill array, part of AMIGA (Auger Muons and Infill for the Ground Array), were added to measure showers with energies include in the range from below the second knee up to the ankle, where the transition from galactic to extra galactic cosmic rays is assumed to occur. The two main experimental requirements are good energy resolution in order to obtain the spectrum and primary type identification since the galactic (heavy primaries) to extra galactic (light primaries) source transition is directly linked to primary composition.

2.3.1 HEAT

At energies below 10^{18} eV the fluorescence light of the air showers is detected only at distances up to 10 km and the showers reach their maximum rather high in the atmosphere, so a large part of the shower profiles falls outside the field of view of the FD telescopes, which is limited to about 30° above the horizon. In these cases, a reliable reconstruction of the shower profile is often not possible. HEAT, consisting of three fluorescence telescopes with an elevated field of view, solves this problem. The HEAT telescopes were built about 180 m in front of the building at Coihueco and are very similar to the original fluorescence telescopes but can be tilted by 29° upward with an electrically driven hydraulic system. The layout of HEAT consists of three telescope enclosures and one container for DAQ, slow control, and calibration hardware. The three enclosures in the tilted-up (upward) data taking position are shown in fig. 2.16, on the left. HEAT works independently of other FD sites, it is the fifth eye of the Observatory. The right part of the fig.

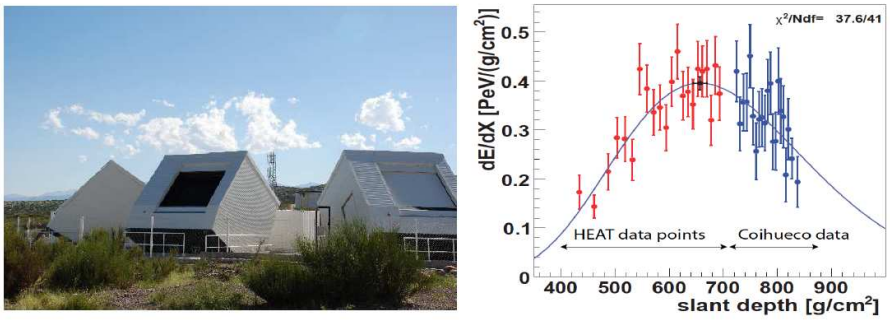

Figure 2.16: Left: The three HEAT telescopes in data-taking mode in tilted orientation. Right: Data points of the first air shower detected by HEAT in January 2009 in coincidence with telescopes in the Coihueco FD building.

2.16 shows data points of the first air showers detected by HEAT in January 2009 in coincidence with Coihueco telescopes. HEAT allowed to reconstruct the first part of the longitudinal profile of the shower, Coihueco the tail. In the horizontal (downward) mode, HEAT is used for cross-calibration with Coihueco telescopes.

2.3.2 AMIGA

HEAT works in combination with an infill array of water-Cherenkov detectors on a 750 m grid close to the HEAT and Coihueco site to extend the energy range of high quality hybrid air shower measurements. AMIGA enhancement spans an area of 23.5 km^2 and it consists of buried scintillator detectors in addition to the denser array. The infill area is much smaller than the regular SD, but the flux of cosmic rays increases steeply with decreasing energy, so this area is sufficient to have a significant statistics. The infill array is fully efficient for air showers with energies that start from 3×10^{17} eV and with zenith angle $\leq 55°$. The SD infill array was completed in September 2011 while the first prototype hexagon of buried scintillators, the *Unitary Cell*, is fully operative by the end of 2014. The Unitary Cell and the denser array nested within the 1500 m array are shown in fig. 2.17 (a). The Unitary Cell consists of 7 water-Cherenkov detectors paired with 30 m^2 scintillators segmented in two modules of 10 m^2 plus two of 5 m^2 in each position. In addition, two positions of the hexagon are equipped with twin detectors (extra 30 m^2 scintillators) and one position has 20 m^2 extra scintillators buried at a shallower depth to analyze the shielding features. The buried scintillators are placed under about 540 g/cm^2 of vertical mass corresponding to a depth of 2.3 m in the local soil and allow to detect the muonic component of air showers. For the Infill array, the same tools and methods optimized for the full SD array are used. The angular resolution for E $\geq$ 4

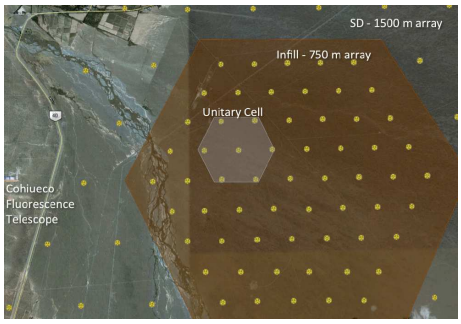

(a)

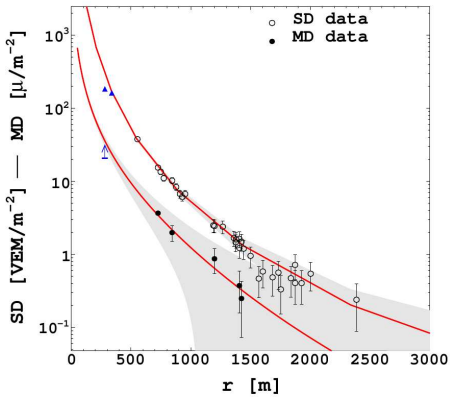

(b)

Figure 2.17: **(a)** Unitary Cell of buried scintillators to detect the muonic component of air showers and the Infill array with 750 m spacing nested within the 1500 m array. **(b)** An example of observed lateral distribution functions obtained with AMIGA prototype hexagon and with the Infill array for a shower with a zenith angle of 39.9° and an energy of $10^{19.1}$ eV. Surface Infill (open circles) and buried scintillator (full circles) station signals are shown together with their corresponding fits.

$\times$ 10^{17} eV is better than 1° and the energy reconstruction is based on the lateral density of shower particles at the optimal distance of 450 m from the core. An example of observed lateral distribution functions obtained with AMIGA prototype hexagon and with the Infill array is shown in fig. 2.17 (b).

The observation of air shower radio emission could be another way to have information about cosmic ray primaries. Radio signals are not absorbed nor deflected on their path, the amplitude of the signal is proportional to the energy of the incoming event and radio detection can operate at 100% duty cycle, so the Auger Observatory, thanks to the AERA project, is testing the possibility of determining the primary energy, the arrival direction, and the mass of cosmic rays from radio signals with accuracies which are equal to or better than those obtained by other techniques and the possibility of building for an affordable price a huge surface-detector array based on

the radio-detection technique. Moreover, it could be also possible to use microwave radiation to detect extensive air showers. Three R&D programs, AMBER, MIDAS and EASIER were installed at the Observatory.

2.4 The Atmospheric Monitoring

The Auger Observatory uses the atmosphere as a giant calorimeter, so it is essential to know the atmospheric characteristics at the Auger site and their variations under changing weather conditions. The atmospheric state variables, including temperature, pressure, and humidity, are needed to assess the longitudinal development of extensive air showers as well as the amount of the isotropically emitted fluorescence light induced by the air showers. The SD observations are also altered by the variation of the atmospheric conditions because the Molière radius, and so the lateral distribution of the shower, changes. Moreover, aerosol and clouds must be studied very well. Their presence and concentration continuosly change and the optical transmission properties of the atmosphere, and so the reconstruction of the light generated along the shower axis, are influenced by them. An extensive system of atmospheric monitoring devices shown in fig. 2.18 has been installed at the Observatory.

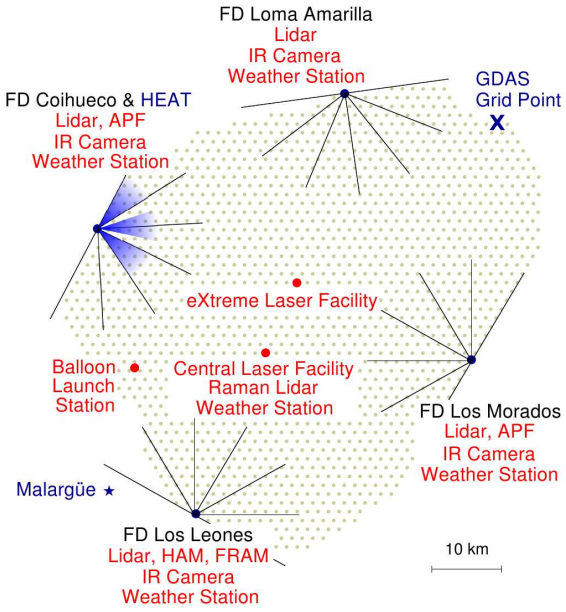

Figure 2.18: Schematic overview of the atmospheric monitoring devices installed at the Pierre Auger Observatory.

The devices used for the monitoring of the atmospheric state variables are:

- *Ground-based weather stations*: there is a weather station for each eye. They are used for operational control of the nearby installations, but the data from them and from CLF (Central Laser Facility) also serve as atmospheric ground information in several parts of the air shower reconstruction. The weather stations are commercial products equipped with temperature, pressure, humidity, and wind speed sensors recording data every 5 minutes;

- *The Balloon Launching Station (BLS)*: helium filled weather balloons, which carried meteorological radiosondes, was lauched from August 2002 to December 2010. In 2005, a dedicated Balloon Launching Station was installed at a suitable position to optimally cover the large area above the surface detector array and in the field of view of the FD telescopes, so from this fully equipped station, more regular launches could be managed, in particular during the night. These measurements are very important to reconstruct the shower profile because ground-based atmospheric data are not enough. Atmospheric profiles of the state variables temperature, pressure, and humidity up to about 20 to 25 km a.s.l. are necessary and from these directly measured values, the derived quantities air density and atmospheric depth are calculated. Monthly models of atmospheric conditions at the Pampa Amarilla were derived in December 2008 using the locally measured atmospheric profiles and now these models are implemented in CORSIKA. Moreover, these measurements are used to validate the utility of data from the Global Data Assimilation System (GDAS) for the Auger Observatory. The GDAS is a global atmospheric model predicated on meteorological measurements and numerical weather predictions [74].

The following devices were installed to study the atmospheric transmission:

- *Aerosol Optical Depth Profiles and Clouds - CLF and XLF (eXtra Laser Facility)*: Laser tracks from CLF and XLF are recorded by the 4 FD sites. They are used to obtain hourly measurements of the aerosol optical depth profiles. These are important in the reconstruction of FD air shower events because they allow to determine the aerosol transmission factor. The vertical aerosol optical depth is defined as the integral of the aerosol extinction from the ground to a point at a given altitude observed at a given elevation angle. Sets of 50 vertical shots are measured every 15 minutes by the FD telescopes throughout each night. CLF has been working since 2004 and in 2013 it was upgraded, while XLF was installed in 2008. Two techniques are adopted to obtain the aerosol optical depth profile for each FD site: the 50-shot averages are compared to averages collected under clear conditions (Data Normalized Analysis [75]), and to simulations generated in different aerosol attenuation conditions (Laser Simulation Analysis [75]). CLF

and XLF also provide information about clouds directly above them;

- *Aerosol Phase Function (APF) monitors*: the atmospheric scattering of light from extensive air showers varies with scattering angle. The scattering angular distribution (phase function) can be estimated analytically for the atmospheric molecular component, but for the aerosol component, it depends on the the size and shape of the aerosols and must be measured. APF monitors are at Coihueco and Los Morados and they consist of a collimated Xenon flash lamp, which directs light between 350 and 390 nm horizontally across the FD field of view of eyes. The data from APS monitors are also used to cross check the clear reference periods chosen for the analyses with CLF and XLF;

- *Horizontal Attenuation Monitor (HAM)*: aerosol attenuation depends on wavelength and this dependence is described by a falling power law with exponential factor γ. It is obtained by the Horizontal Attenuation Monitor in Auger. The HAM consists of a high intensity discharge lamp installed close to the FD building Coihueco and a filtered CCD camera, which measures the light from the lamp, located at Los Leones, about 45 km away. Total horizontal atmospheric attenuation is measured over this path at five wavelengths between 350 and 550 nm.

Clouds can distorce the reconstructed longitudinal profile in two different ways. If clouds attenuate or block the light from an air shower, the longitudinal profile shows a dip, but if shower passes through a cloud layer, the cloud can enhance the scattering of the intense Cherenkov light beam and this produces a bump in the profile. To monitor clouds, the Auger Oservatory has several devices:

- *Infra-red Cloud Camera*: clouds are warmer than the surrounding atmosphere and produce an infra-red signal that depends on the cloud temperature and emissivity (or optical depth). Each FD building has an infra-red camera mounted on a pan-and-tilt scanning platform. Every 5 minutes the camera scans the field of view of the telescope, and every 15 minutes a picture of the entire hemisphere is ready. The data from the camera are also mapped on to FD pixel directions to indicate the presence or absence of clouds in each FD pixel;

- *Geostationary Operational Environmental Satellites (GOES)*: GOES-12 imager instrument covers the area of the Pierre Auger Observatory every 30 minutes and provides radiance data in one visible and four infrared bands. Cloud probability maps with a grid of 2.4 km by 5.5 km pixel size are being derived for the area of the Observatory. For the pixels viewing the CLF, the measurements from GOES are compatible with that ones obtained from FD measurements of CLF vertical tracks;

- *FD Lidar Stations*: cloud cover, cloud height and aerosols are also measured by four elastic lidars located next to each FD eye. Lidars have an analog and a photon counting readout system and combining the traces coming from these two parallel readout channels, the range of measure goes from 200 m up to 25-30 km. The lidars are steerable and perform discrete and continuous scanning patterns automatically during the FD operation, but the shots are fired outside the FD FOV to avoid interference with data taking. Only after especially interesting cosmic ray candidates, for example a very high energy event, the lidar fires at the region of the expected arrival direction of the shower. Moreover, horizontal shots are pointed to CLF to measure ground level aerosol horizontal attenuation length;

- *Ph(F)otometric Robotic Atmospheric Monitor (FRAM)*: is an optical telescope conceived to determine the wavelength dependence of Rayleigh and Mie scattering using starlight. It is also used to make automatic observations of light curves of optical transients related to gamma ray bursts. It is a passive instrument, so it can operate in the field of view of the FD.

The atmospheric monitoring data are organized into MySQL databases that are accessed by the Pierre Auger offline analysis package described in section 2.6.

2.5 Hybrid Reconstruction

As already pointed out, the hybrid combination of the FD and the SD has an enormous advantage in the determination of the energy scale. The FD provides a nearly calorimetric energy measurement as the fluorescence light is proportional to the energy dissipation by a shower in the atmosphere. These measurements are performed with a duty cycle of about 15%, as the FD can only operate during clear nights with little moonlight. The SD measures the distribution of particles at ground with a duty cycle of almost 100%, but the estimation of the energy for events detected by the surface detector is strongly dependent on the hadronic interaction models. For showers viewed by the FD in coincidence with the SD, the signal detected by the SD at 1000 m from the shower axis is calibrated against the calorimetric energy measured with the FD, so thanks to the hybrid detector the energy assignment is largely independent of air shower simulations and also more accurate. In fact, a hybrid detector also achieves the best geometrical accuracy by using timing information from all the detector components, both FD pixels and SD stations and the geometry reconstruction is the first step for the energy reconstruction.
The events detected by the Auger Observatory can be classified in three

categories:

1. **FD events**: detected only by the fluorescence telescopes; they are *mono-events* if they are detected by one eye, *stereo* if they are detected by at least two eyes;

2. **SD events**: detected only by the surface detector. The statistics of these events is very high;

3. **hybrid events**: detected by at least one eye and one SD station. If they are detected by one eye and a sufficient number of stations for an indipendent SD reconstruction, they are called *golden events*. They are *stereo-hybrid events* if they are detected also by more than one eye.

In the following, the individual reconstruction steps will be described for all vertical events ($\theta < 60°$).

2.5.1 FD Reconstruction

In the FD, cosmic ray showers are detected as a sequence of triggered pixels in the camera. Fig. 2.19-left shows the track of an event that passes through two adjacent telescopes. The first step of the reconstruction is the determination of the *Shower Detector Plane* (SDP), shown in fig. 2.19-right. It is the plane that includes the location of the eye and the line of the shower axis and it is identified minimizing the following expression:

$$S = \frac{1}{\sum_i q_i} \sum_i w_i \Big(\frac{\frac{\pi}{2} - arccos(\overrightarrow{n}_{\perp}^{SDP} \cdot \overrightarrow{p_i})}{\sigma_{SDP}} \Big)^2,$$

where q_i is the signal collected in each pixel used as weight, $\overrightarrow{n}_{\perp}^{SDP}$ is the vector normal to SDP, and $\overrightarrow{p_i}$ the pixel pointing direction. The pointing uncertainty for the SDP fit, σ_{SDP} , was determined to be 0.35° using CLF laser shots. The shower axis within the SDP is reconstructed using the timing information of the pixels. It is characterized by two parameters: the perpendicular distance R_p from the camera to the track, and the angle χ_0 that the track makes with the horizontal line in the SDP. t_0 is the time when the shower front on the axis passes the point of closest approach R_p to the camera. These three parameters are estimated minimizing the function:

$$\chi^2 = \sum_i \frac{(t_i - t(\chi_i))^2}{\sigma^2(t_i)} + \frac{(t_{SD} - t(\chi_{SD}))^2}{\sigma^2(t_{SD})},$$

where

$$t(\chi_i) = t_0 + \frac{R_p}{c} tan\Big(\frac{\chi_0 - \chi_i}{2}\Big).$$

and represents the angular movement of the shower within the SDP. The sum runs over all pulsed pixels i with time t_i and associated uncertainty

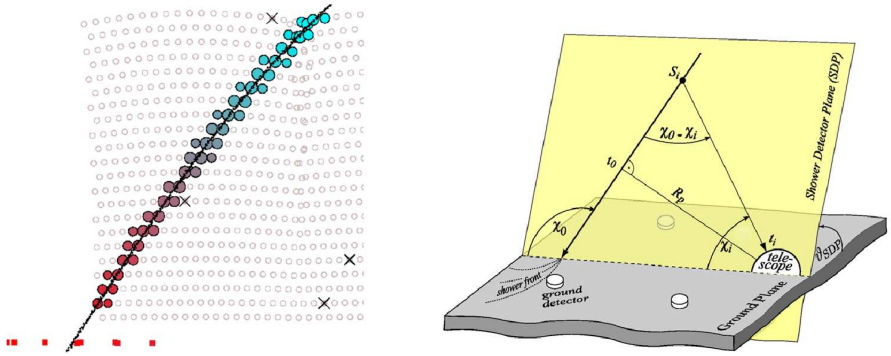

(a) (b)

Figure 2.19: **(a)** Light track of a hybrid event seen by two adjacent fluorescence telescopes. The different colors indicate the timing sequence of the triggered pixels. The full line is the fitted shower-detector plane. The red squares, instead, represent the surface stations also triggered by this shower. **(b)** Illustration of the *Shower Detector Plane* (SDP), that is the plane through the eye which most nearly contains the pointing directions of the FD pixels centered on the shower axis and where the projection of a shower on the camera evolves.

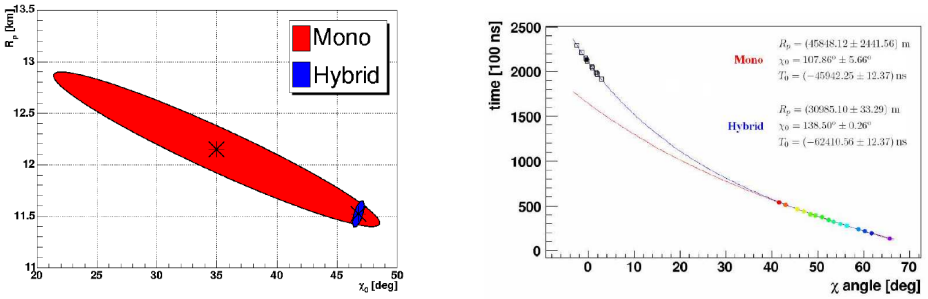

(a) (b)

Figure 2.20: **(a)** Phase space of SDP parameters for the FD monocular reconstruction (red) and for the hybrid reconstruction (blue). **(b)** Correlation of the arrival times of light with pixel elevation taken within the SDP. The color code reflects the pixel trigger time.

$\sigma(t_i)$. χ_i is the angle that the pointing direction of each pixel which observes the track makes with the horizontal line.
To improve the reconstruction, the time t_{SD} with the uncertainty $\sigma(t_{SD})$, related to the SD triggered station with the largest signal, is added. χ_{SD} is the angle at which the shower front hits the station and t_{SD} is corrected for the delay caused by the shower front curvature. In fig. 2.20-left, it is possible to see that the phase space of SDP parameters for hybrid reconstruction (blue) is very smaller than that one for the FD monocular reconstruction (red).
Fig. 2.21 shows an even that has been observed by four telescopes. The

black lines indicate the individual four reconstructions of the geometry using the hybrid approach. In several analyses, the individual reconstructions are merged.

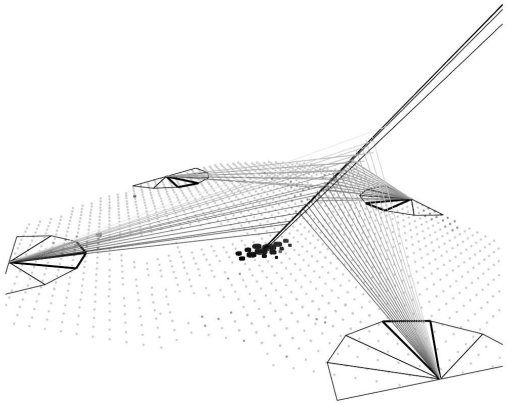

Figure 2.21: Geometry reconstruction of a stereo-hybrid event observed by four FD telescopes and the surface detector.

Once the geometry of the shower is known, the light collected at the aperture as a function of time, that is proportional to the energy released by charged particles propagating through the atmosphere, can be converted to energy deposit by the shower as a function of slant depth (X). The total light at the aperture is obtained by adding the signals of the camera pixels at each time bin i. Only the pixels with pointing directions that are within a certain angular distance ζ to the vector from the telescope to the shower center at time i are included. ζ is chosen so as to maximize the signal to noise ratio. For the conversion, the light attenuation from the shower to the telescope needs to be estimated and all contributing light sources need to be disentangled [76]: fluorescence light, direct and scattered Cherenkov light as well as multiple-scattered light. The total light at the aperture and these several contributions are shown on the left of fig. 2.22. The calorimetric energy of a shower is estimated fitting the reconstructed energy deposit profile with a Gaisser-Hillas function and integrating it. The longitudinal energy deposit profile is expressed by:

$$f_{GH}(X) = \Big(\frac{dE}{dX}_{max}\Big)\Big(\frac{X - X_0}{X_{max} - X_0}\Big)^{\frac{X_{max}-X_0}{\lambda}} e^{\frac{X_{max}-X}{\lambda}}.$$

The maximum of the energy deposit profile $\frac{dE}{dX}_{max}$ is reached at depth $X = X_{max}$, called *depth of the shower maximum*. Λ and X_0 are two shape parameters that are constrained to their average values.
Finally, the total energy is estimated by correcting the calorimetric energy for the "invisible energy" carried away by neutrinos and high energy muons

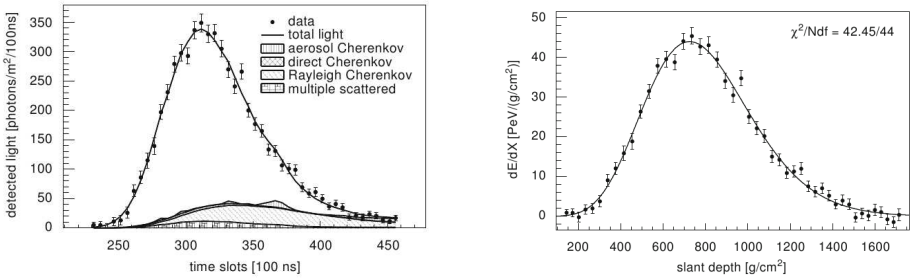

(a) (b)

Figure 2.22: **(a)** Example of a light-at-aperture measurement (dots) and reconstructed light sources (hatched areas). **(b)** Energy deposit profile fitted with a Gaisser-Hillas function.

[77].
The several contributions to the systematic uncertainty affecting energy reconstruction [78] are shown in fig. 2.23.

2.5.2 SD Reconstruction

The reconstruction of the energy and the arrival direction of cosmic rays that produce air showers triggering the SD detector is based on size and time of the signals recorded by the tanks [79].
To reconstruct the geometry of the shower, a planar shower front is assumed. The components of the shower axis $\vec{a} = (u, v, w)$ are obtained minimizing the following expression:

$$\chi^2 = \sum_i \frac{[ct_i - ct_0 + ux_i + vy_i]^2}{\sigma_i^2}, \tag{2.1}$$

where t_i is the signal start time in the station i and t_0 is the time at which the shower passes the signal weighted barycenter of all the stations. This expression can be seen as a set of linear equations and is analytically solved. The obtained approximate solution is used as starting point for more elaborate procedures that consider more realistic curved shower front models. Fig. 2.24 shows a schematic representation of the evolution of the shower front.
The footprint of the air shower at ground, shown in fig. 2.25 (left), is sampled by a limited number of SD stations, so it is necessary a fit to know the impact point and the lateral distribution of a shower (fig. 2.25 - right). It is described by a modified Nishimura-Kamata-Greisen (NKG) function:

$$S(r) = S(r_{opt}) f_{LDF}(r) = S(r_{opt}) \Big(\frac{r}{r_{opt}}\Big)^{\beta} \Big(\frac{r + r_1}{r_{opt} + r_1}\Big)^{\beta+\gamma}, \tag{2.2}$$

where f_{LDF} is the *Lateral Distribution Function* (LDF), $r_1 = 700$ m, r_{opt} is the distance at which the signal at ground is less dependent by the LDF

Systematic uncertainties on the energy scale	
Absolute fluorescence yield	3.4%
Fluor. spectrum and quenching param.	1.1%
Sub total Fluorescence yield	**3.6%**
Aerosol optical depth	3%÷6%
Aerosol phase function	1%
Wavelength depend. of aerosol scatt.	0.5%
Atmospheric density profile	1%
Sub total Atmosphere	**3.4%÷6.2%**
Absolute FD calibration	9%
Nightly relative calibration	2%
Optical efficiency	3.5%
Sub total FD calibration	**9.9%**
Folding with point spread function	5%
Multiple scattering model	1%
Simulation bias	2%
Constraints in the Gaisser-Hillas fit	3.5% ÷ 1%
Sub total FD profile rec.	**6.5% ÷5.6%**
Invisible energy	**3%÷1.5%**
Stat. error of the SD calib. fit	**0.7%÷1.8%**
Stability of the energy scale	**5%**
Total	**14%**

Figure 2.23: Systematic uncertanties on the energy scale.

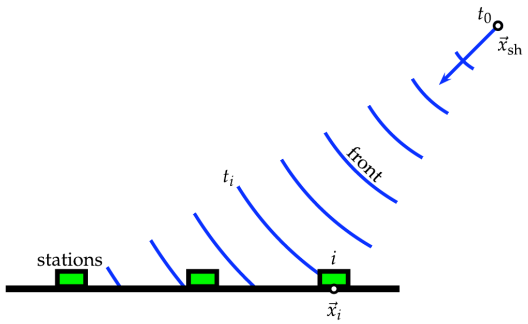

Figure 2.24: Schematic representation of the evolution of the shower front.

parameters, that in turn depend on the hadronic models, and it changes for different arrays. $S(r_{opt})$ is the energy estimator for the events collected only by the surface detector. For the Auger SD array, $r_{opt} = 1000$ m, and so the energy estimator is $S(1000)$. The parameter β depends on the zenith angle and shower size. Events with small zenith angle are observed at an earlier shower age than more inclined ones, and for them, the contribution of the electromagnetic component on the ground is dominant and their LDF is steeper. The reconstruction accuracy of S(1000), $\sigma_{S(1000)}$, is composed

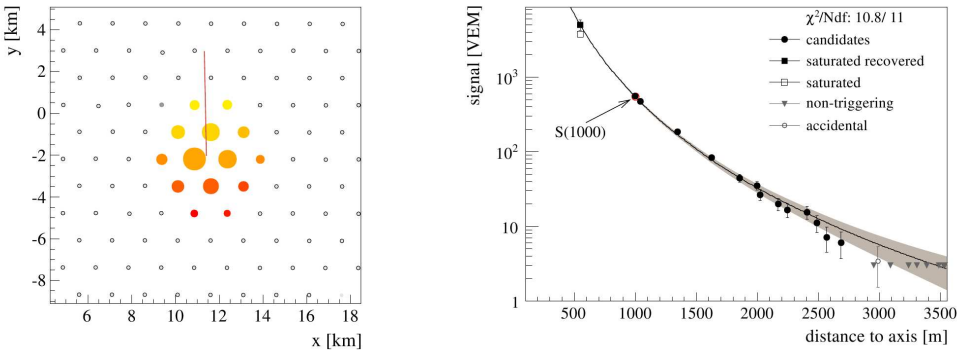

Figure 2.25: Left: footprint of a shower on the ground. At the highest energies, above 10 EeV, it extends over more than 25 km^2. Right: dependence of the signal size on distance from the shower core.

of three contributions: a statistical uncertainty due to the finite number of particles producing signal in a given SD station and the limited dynamic range of the signal detection; a systematic uncertainty due to assumptions on the shape of the lateral distribution function; and an uncertainty due to shower-to-shower fluctuations.
The angular resolution of the whole reconstruction procedure is reconstructed with a single station time variance model [80] that uses the size of the total signal and the time evolution of the signal trace, but the angular resolution improves when the number of the station used in the LDF fit increases. The angular resolution for events with more than 3 stations is better than 1.6°, and better than 0.9° for events with more than 6 stations.

2.5.3 Energy Calibration

S(1000) is dependent on the zenith angle of a shower, in particular S(1000) decreases with increasing zenith angle due to the attenuation of the shower particles and geometrical effects. The Constant Intensity Cut (CIC) method [81] allows to extract the shape of the attenuation curve from the data assuming an isotropic flux of primary cosmic rays at the top of the atmosphere. The attenuation curve $f_{CIC}(\theta)$, shown in fig. 2.26, has been fitted with a

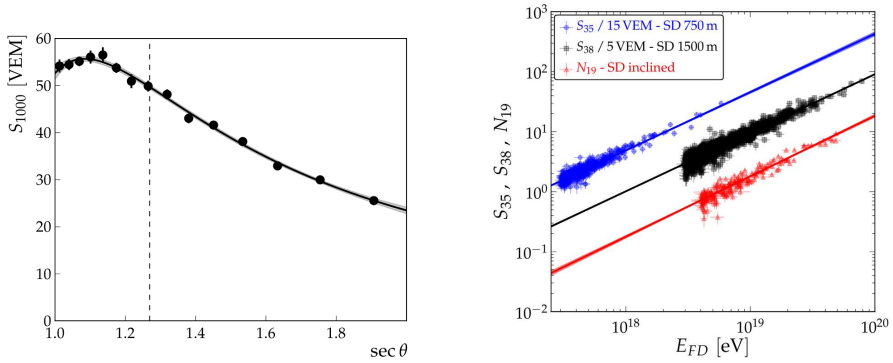

(a) (b)

Figure 2.26: **(a)** Attenuation curve described by a third degree polynomial in $x = cos^2(\theta) - cos^2(\bar{\theta})$ where $\bar{\theta}$=38° (denoted by the dashed vertical line). **(b)** The correlation between the different SD energy estimators S_{38} (full array, vertical showers - $\theta < 60°$), S_{35} (Infill array, vertical showers), N_{19} (full array, inclined showers - $\theta > 60°$) and the calorimetric energy determined by FD.

third degree polynomial

$$f_{CIC}(\theta) = 1 + ax + bx^2 + cx^3,$$

where $x = cos^2(\theta) - cos^2(\bar{\theta})$, $a = 0.98 \pm 0.004$, $b = -1.68 \pm 0.01$, and $c = -1.30 \pm 0.45$. $\bar{\theta}$=38° is the median angle of the great part of showers detected by the Auger Observatory. Thanks to this curve, S(1000) is converted to S_{38}, that is defined as the signal that a shower with size S(1000) would have produced if it had zenith angle equal to 38°.
At this point, the SD energy estimator S_{38} must be calibrated with the calorimetric FD energy, E_{FD}. To estimate the calibration curve, only the events which have triggered independently the FD and SD detector are used. The selected sample is made up by 1475 high quality hybrid events recorded between Jan 2004 and Dec 2012. The correlation between the two variables is obtained from a maximum likelihood method [82, 84] and it is well described by a single power-law function:

$$E_{FD} = A(S_{38}/VEM)^B,$$

where $A = (1.90 \pm 0.05) \times 10^{17} eV$ and $B = 1.025 \pm 0.007$ [83].
In fig. 2.27 are summarized some of the important parameters that characterize the performance of the Observatory. These parameters include the event rate of the detectors and the resolutions of the different observables reconstructed.
Details on the reconstruction of inclined showers (60°<θ<90°) and showers detected by the Infill array are respectivily given in [84, 85], and [86, 87].

SD	
SD Exposure	$\sim$5500 km^2 sr/yr
T3 rate	0.1 Hz
T5 events/yr, $E > 3$ EeV	$\sim$14 500
T5 events/yr, $E > 10$ EeV	$\sim$1500
Reconstruction accuracy (S_{1000})	22% (low E) to 12% (high E)
Angular resolution	1.6° (3 stations)
	0.9° (>5 stations)
Energy resolution	16% (low E) to 12% (high E)
FD	
Uptime	$\sim$15%
Rate per building	0.012 Hz
Rate per HEAT	0.026 Hz
Hybrid	
Core resolution	50 m
Angular resolution	0.6°
Energy resolution (FD)	8%
$X_{\max}$ resolution	<20 g/cm^2

Figure 2.27: Key performance parameters for the Auger Observatory.

2.6 The $\overline{Off}\underline{line}$ Software

The $\overline{Off}\underline{line}$ software of the Pierre Auger Observatory provides both an implementation of simulation and reconstruction algorithms and an infrastructure to support the development of such algorithms leading ultimately to a complete simulation, reconstruction and analysis pipeline. A complete description of the software is available in [88]. The software has been designed to accommodate contributions from a large number of physicists developing C++ applications over the long lifetime of the experiment. The processing *modules* are assembled and sequenced through instructions contained in an XML file. Modules have access to *event* and *detector* structures in order to relay data to one another, accumulates all simulation and reconstruction information related to the detector conditions, calibration constants and atmospheric properties as a function of time. A *Run Controller* invokes the various processing steps within the modules according to a set of user-provided instructions. A *Central Config* object is responsible for pointing modules and framework components to the location of their configuration data and for tracking provenance. The general structure of the $\overline{Off}\underline{line}$ framework is shown in fig. 2.28.

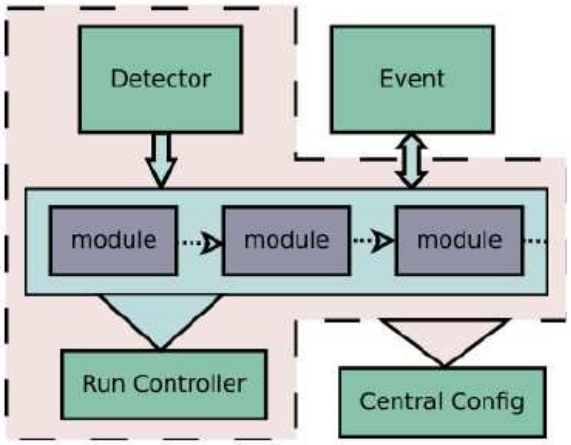

Figure 2.28: General structure of the $\overline{Offline}$ framework.

Chapter 3

The energy spectrum of light elements

The analysis presented in this thesis is focused on the construction of the energy spectrum of light elements. It is interesting to study possible features of the light spectrum and its shape with respect to the total Auger spectrum in order to have information about the cosmic ray mass composition in different energy ranges, that can help to distinguish among several theoretical models starting from different assumptions on cosmic ray composition, sources, acceleration methods, and propagation as seen in section 3.1. The analysis is based on hybrid data with energies greater than 10^{18} eV collected from January 2004 to December 2013. The variable chosen to select light elements is the depth of shower maximum. Above 10^{19} eV, the statistics of the light hybrid events is very low. Therefore, to understand better the last part of the light spectrum, an attempt to use the large amount of showers collected by the surface detector applying on them the universality method was made.

3.1 The Auger Spectrum

The flux of cosmic rays J as a function of energy is given by:

$$J(E) = \frac{d^4 N_{inc}}{dE dA d\Omega dt} \cong \frac{\Delta N_{sel}(E)}{\Delta E} \frac{1}{\varepsilon(E)},$$

where Ninc is the number of cosmic rays with energy E incident on a surface element dA, within a solid angle $d\Omega$ and time dt. $\Delta Nsel(E)$ is the number of detected events passing the quality cuts in the energy bin centered around E and having width ΔE. $\varepsilon(E)$ is the energy-dependent exposure, that is the integral over the instantaneous aperture. The latter represents the product of the solid angle times the area viewed from the incoming particles.

The flux of cosmic rays above 3×10^{17} eV has been measured with unprecedented precision at the Pierre Auger Observatory based on data in the period between 1 January 2004 and 31 December 2012 [83]. It is the combination of spectra measured using vertical hybrid events, vertical and inclined SD events and vertical showers collected by the Infill surface detector. In general, showers with zenith angle $\theta < 60°$ are defined "vertical events" (for the Infill analysis, $\theta < 55°$), while showers with $62° \leq \theta \leq 80°$ are the "inclined events". As already pointed out, the energy reconstruction of vertical SD events is based on the estimation of the lateral distribution of secondary particles of an air shower reaching ground at an optimal distance to the shower core. For the 1500 m and 750 m arrays the optimal distances, determined empirically, are 1000 m and 450 m respectively, and the signals S(1000) and S(450) corrected for their zenith angle dependence is calibrated with the FD calorimetric energy as shown in fig. 2.26 (b). The signal produced by inclined showers is dominated by muons, so their reconstruction is based on the estimation of the relative muon content N_{19} with respect to a simulated proton shower with energy 10^{19} eV. The exposure of the 750 m array, therefore only inclined events from the 1500 m array are included in the spectrum analysis. In the hybrid analysis, the selected events are that ones with energies above 10^{18} eV and that pass the following cuts to ensure a reliable reconstruction: in the plane perpendicular to the shower axis, the reconstructed shower core must be within 1500 m of the station used for the geometrical reconstruction; the contribution of Cherenkov light to the signal collected by the fluorescence telescopes must be less than 50%; the Gaisser-Hillas fit of the reconstructed longitudinal profile must be successful with $\chi^2/Ndof < 2.5$, X_{max} must be observed in the field of view of the telescopes; the uncertainty in the reconstructed energy, which includes light flux and geometrical uncertainties, must be $\sigma(E)/E < 20\%$. Moreover, only time periods with the sky not obscured by clouds and with a reliable measurement of the vertical optical depth of aerosols are used. The most delicate point of this analysis is the precise determination of the detector exposure that is influenced by several factors. They will be described in detail in section 3.1.1. The hybrid exposure and exposures of the SD array (section 4.3.1) for the different datasets are shown in fig. 3.1. Values up to 31 Dec 2012 are given in fig. 3.2 together with their uncertainties and the relevant zenith angle ranges. The hybrid spectrum extends the SD 1500 m spectrum below the energy of full trigger efficiency of 3×10^{18} eV and overlaps with the spectrum of the 750 m array above 10^{18} eV. The latter is fitted up to 3×10^{18} eV and extends the measurement of the energy spectrum below 10^{18} eV. The spectrum of inclined events contributes above its full efficiency threshold of 4×10^{18} eV and provides an independent measurement in this energy range. These measurements are combined into a single energy spectrum. The four individual spectra are depicted on the left of fig. 3.3, while the right panel shows the combined energy spectrum together with the number of observed

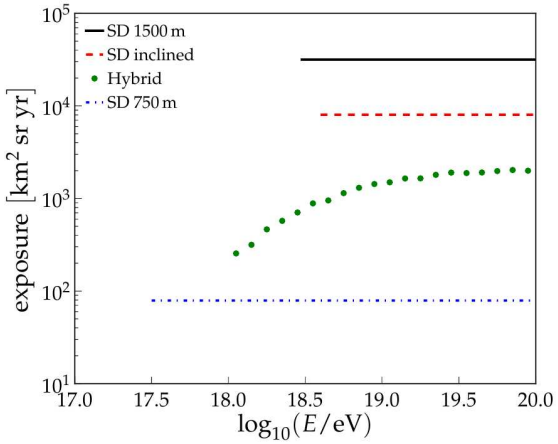

Figure 3.1: The exposure of the different detectors at the Pierre Auger Observatory as a function of energy. The SD exposure in the three cases is flat above the energy corresponding to full trigger efficiency for the surface arrays.

	Auger SD			**Auger hybrid**
	1500 m vertical	**1500 m inclined**	**750 m vertical**	
Data taking period	01/2004 - 12/2012	01/2004 - 12/2012	08/2008 - 12/2012	11/2005 - 12/2012
Exposure $[\mathrm{km}^2\ \mathrm{sr\ yr}]$	31645 ± 950	8027 ± 240	79 ± 4	see Fig. 4.1
Zenith angles [°]	$0-60$	$62-80$	$0-55$	$0-60$
Threshold energy E_{eff} [eV]	3×10^{18}	4×10^{18}	3×10^{17}	10^{18}
No. of events ($E > E_{\mathrm{eff}}$)	82318	11074	29585	11155
No. of events (golden hybrids)	1475	175	414	-
Energy calibration (A) [EeV]	0.190 ± 0.005	5.61 ± 0.1	$(1.21 \pm 0.07) \cdot 10^{-2}$	-
Energy calibration (B)	1.025 ± 0.007	0.985 ± 0.02	1.03 ± 0.02	-

Figure 3.2: Summary of the experimental parameters describing data of the different spectra analyses.

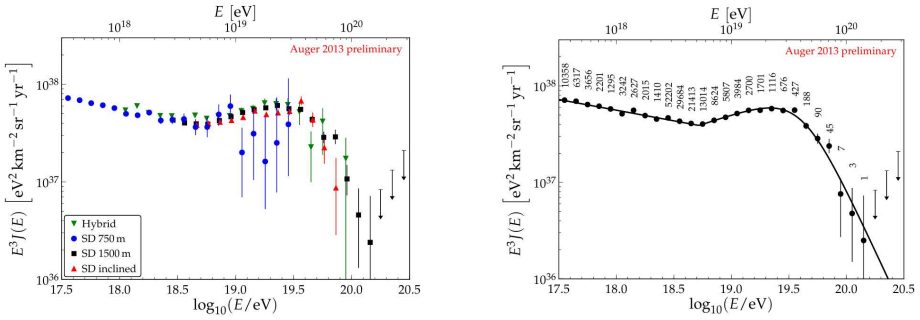

Figure 3.3: **(a)** Energy spectra, corrected for energy resolution, derived from SD and from hybrid data. **(b)** The combined energy spectrum of UHECRs from data collected by different nested detectors located at the Pierre Auger Observatory. The numbers give the total number of events inside each bin. The last three arrows represent upper limits at 84% C.L.

events within each bin. The data are described with a power law below the ankle $J(E) \approx E^{-\gamma_1}$ and a power law with smooth suppression above in order to characterize the spectral features:

$$J(E; E > E_a) \approx E^{-\gamma_2} \left[1 + exp\left(\frac{log_{10}E - log_{10}E_{1/2}}{log_{10}W_c}\right)\right]^{-1}.$$

E_a is the energy at which the ankle is observed, and γ_1 and γ_2 are the spectral indeces below and above the ankle. At $E = E_{1/2}$, the flux has dropped to half of its peak value before the suppression, the steepness of which is described with $log10W_c$. The obtained spectral parameters are listed in the table of fig. 5.25. To match the energy spectra, the SD 750 m spectrum has to be

Parameter	**Result** ($\pm\sigma_{\text{stat}} \pm \sigma_{\text{sys}}$)
$\log_{10}(E_a/\text{eV})$	$18.72 \pm 0.01 \pm 0.02$
γ_1	$3.23 \pm 0.01 \pm 0.07$
γ_2	$2.63 \pm 0.02 \pm 0.04$
$\log_{10}(E_{1/2}/\text{eV})$	$19.63 \pm 0.01 \pm 0.01$
$\log_{10} W_c$	$0.15 \pm 0.01 \pm 0.02$

Figure 3.4: Parameters of the models used to describe the Auger combined energy spectrum.

scaled up by 2%, the inclined spectrum up by 5% and the hybrid spectrum down by 6%.

3.1.1 Hybrid Exposure

The aperture of a cosmic ray detector is related to the observation capability of the instrument. The exposure, that is the time integrated aperture, as a function of the energy of primary particle, can be written as [91]:

$$\varepsilon(E) = \int_T \int_\Omega \int_{S_{gen}} \epsilon(e,t,\theta,\Phi,x,y) cos\theta dS d\Omega dt,$$

where $d\Omega = sin\theta d\theta d\psi$ and Ω are respectively the differential and total solid angles, θ and ψ are the zenith and azimuth angles and $dS = dx \times dy$ is the horizontal surface element. The final selection efficiency ϵ includes the efficiencies of the various steps of the analysis, namely the trigger, reconstruction and selection efficiencies and also the evolution of the detector during the time period T. It has been derived from Monte Carlo simulations that scan an area S_{gen} large enough to enclose the full detector array.
The detector configurations of the Observatory have been continuously changing over the period of data collection for the hybrid spectrum. In 2004, the Observatory wasn't finished, so the number of stations in operation increased over the years. Moreover, some SD stations can be temporarily out of service at any one time. The SD status is monitored by updating each second the list of "active" stations. The FD detector configuration also changed with time during the construction phase, with the number of telescopes changing from 12 to 24, and a correction ring lens was added to each telescope during the first two years of data taking. During nightly operations, individual telescopes are sometimes deactivated because of increasing sky brightness, bad weather conditions or hardware failures, and the signal collected by the telescopes is influenced by the atmospheric conditions. All these changes are considered thanks to a sample of events simulated with the *Time Dependent Detector Simulation* method, and given a set of N simulated events generated on an area S_{gen} within the time interval T, the exposure can be calculated numerically via

$$\varepsilon(E_{sim}) = 2\pi S_{gen} T \sum_i \frac{n(E_{sim}, con\theta_i)}{N(E_{sim}, con\theta_i)} cos\theta_i \Delta cos\theta_i,$$

where n is the number of events that fulfill the selection criteria. At the present time, the exposure is calculated as a function of reconstructed energy, E_{sim}, and after a correction to considere the resolution of the energy reconstruction is applied.
The efficiency of fluorescence and hybrid data taking is influenced by many effects. To perform the time dependent detector simulation we have to take into account all known disturbances and then derive the *on-time* of the hybrid detection mode. As a compromise between accuracy and stability, the complete detector status down to the single pixel is derived for time intervals

T_{bin} = 10 min. For each time t in a given time slot of duration T_{bin} , the fraction of operational time $f(i,t)$, for the telescope i belonging to the FD site s, can be written as:

$$\begin{aligned} f(i,t) =& \epsilon_{shutter}(i,t) \cdot \epsilon_{DAQ}(i,t) \cdot \delta_{tel}(i,t) \\ & \cdot \epsilon_{Lidar}(s,t) \cdot \langle \epsilon_{T3_{veto}}(s,t) \rangle \cdot \delta_{CDAS}(t). \end{aligned} \tag{3.1}$$

Even if the DAQ is running, the shutters of the telescope might be closed due to bad weather alarms from the slow control system or other failsafe mechanisms. $\epsilon_{shutter} = T_{open}/T_{bin}$ is related to the status of the shutters. T_{open} denotes the time (for a given telescope) for which the mean variance over the whole camera is larger than 8 ADC^2. Muons hitting the pixel camera is the main source of the noise triggers and they alone produce a mean variance of about 3.5 ADC^2. If background data are not available, $\epsilon_{shutter}$ is not calculated, and the status flag δ_{tel} is then set to 0. The deadtime due to the finite readout speed of the DAQ system must also be taken into account. $\epsilon_{DAQ} = 1 - (T^{dead}_{DAQ}/T_{DAQ})$, where T^{dead}_{DAQ} is the deadtime in a certain time interval, and T_{DAQ} is the total running time of the DAQ in the same time interval. There are several sources of inefficiency related to the data taking at the FD-site level. One of this is due to the atmospheric monitoring system. The Lidar system sets an FD veto when it shoots in the field of view of a FD detector. The cumulative Lidar veto time, called T^{dead}_{Lidar}, is converted into an efficiency by $\epsilon_{Lidar} = 1-(T^{dead}_{Lidar}/T_{DAQ})$. This efficiency is calculated for each FD site s. The FD triggers are sent to and processed by the CDAS, which in turn sends a signal to the surface detector to extend the SD trigger threshold to lower energies. In the CDAS, a protection algorithm to prevent the acquisition of long periods of excessive event rates is also implemented, FD events are not recorded by the CDAS, and this causes a loss of hybrid events. An estimate of the event loss probability in a given time interval is calculated by comparing events from the FD data files and from the final merged hybrid files, which only include those sent to CDAS. This mechanism is energy dependent as it is related to the SD trigger probability, and is accounted for on an average basis. $\langle \epsilon_{T3_{veto}}(s,t) \rangle$ is the resulting average efficiency for each FD site s and time t. Moreover, time periods with trigger related problems are excluded in the hybrid on-time via the CDAS status flag δ_{CDAS}. The on-time fraction, defined as the ratio of the overall on-time to the time duration of each interval, over 3 years during the construction phase of the observatory is shown in fig. 3.5.

For the calculation of the hybrid exposure, the size of the simulated event sample is crucial for acceptable statistical and systematic uncertainties. Therefore, full Monte Carlo simulations are performed for specific studies, while fast simulations, validated with the full Monte Carlo method, are used when high statistics are required.

To study the trigger efficiency and the detector performances, a complete

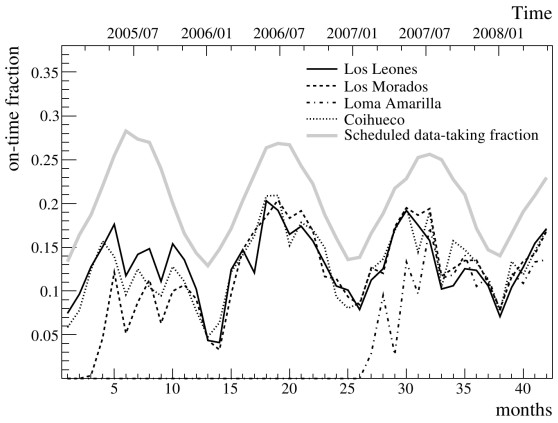

Figure 3.5: Time evolution of the average hybrid on-time fraction during the construction phase of the Pierre Auger Observatory. Gray line represents the scheduled data-taking time fraction limited to the nights with moon-fraction lower than 60%.

Monte Carlo hybrid simulation is necessary. The simulation sample consists of CORSIKA [**?**] showers with energies ranging between 10^{17} and $10^{19.5}$ eV. The FD simulation chain reproduces in detail all the physical processes involved in the fluorescence technique. The surface detector response is simulated using Geant4 within the framework provided by the Auger Offline software. The hybrid trigger efficiency is flat and equal to 1 at energies greater than 10^{18} eV.
To follow and reproduce the time dependence of the hybrid exposure, each detector configuration must be taken into account and a large number of simulations is required. Therefore, CONEX showers are used. CONEX generator solves the cascade numerically after the simulation of the first few ultra-high energy interactions. Moreover, it does not generate ground level particles, and so the SD trigger is reproduced using the "Lateral Trigger Probability" (LTP) parameterisation functions. The SD timing information needed in the hybrid reconstruction is provided by a simplified simulation, *SdSimpleSim*, implemented in the Offline simulation framework. This method also includes the simulation of noise triggered stations, which could spoil the reconstruction of the event. CONEX simulation is extremely fast, and provides the most important features reproduced by full Monte Carlo simulations, including shower to shower fluctuations.
CONEX showers with energies from 10^{17} up to 10^{21} eV and simulated with several high-energy hadronic interaction models are used to calculate the exposure for the total hybrid energy spectrum. Proton and iron particles are taken as cosmic ray primaries. Events really considered in the calculations are those passing the quality cuts described in section 3.1. Furthermore, to provide a robust calculation of the exposure, independent of the trigger threshold, mass composition and energy scale uncertainty, the fiducial cuts

have to be applied to data. The limited field of view of the fluorescence detector and the requirement that the shower maximum falls in the FOV can lead to a different selection efficiency for different primary masses. Protons develop deeper into the atmosphere and for vertical events, they have a smaller selection efficiency because their maxima fall below the observation level in several cases. The exposure for protons and iron nuclei after the quality cuts is shown in the left panel of fig. 3.6. At low energies, where

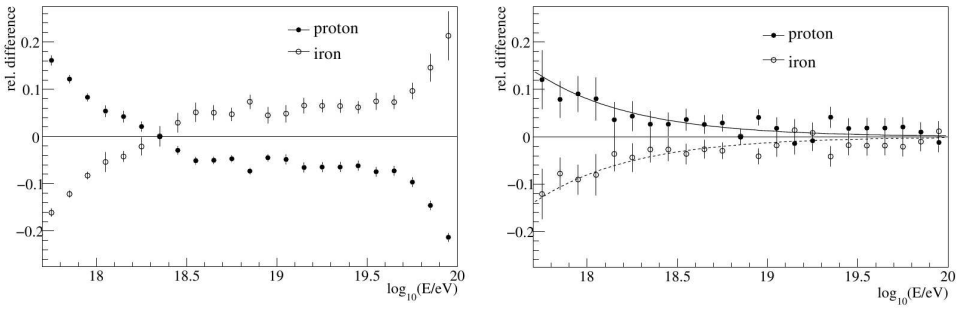

(a) quality selection (b) quality and fiducial volume

Figure 3.6: Relative difference between proton and iron exposure with respect to a mean composition exposure, as obtained from the Time Dependent Detector Simulation. Left panel: exposures after the quality cuts. Thea are strongly dependent on the mass composition. Right panel: This dependence is reduced by the apllication of the fiducial cuts.

events are only detected close to the detector, proton primaries have the bigger efficiences, while at higher energies iron primaries are dominant. To reduce these differences, the following cut is applied:

$$\begin{aligned} X_{up}[g/cm^2] &\geq 900 + 6 \cdot (\epsilon - 18) \\ X_{low}[g/cm^2] &\leq \begin{cases} 550 - 61 \cdot (\epsilon - 19.6)^2 & \text{for } \epsilon < 19.6 \\ 550 & \text{for } \epsilon \geq 19.6 \end{cases} \end{aligned} \tag{3.2}$$

ϵ=log(E/eV), and X_{up} and X_{low} are the upper and lower boundaries of the telescope field of view which depend on the shower geometry. The exposure for protons and iron nuclei after these fiducial cuts is shown in the right panel of fig. 3.6. The exposure dependence on the cosmic ray primary is reduced and this is very important for the all masses energy spectrum because the exposure is calculated assuming a mixed composition of 50% proton and 50% iron nuclei. These cuts have been optimized over time and the parameters are slightly changed.

The fluorescence detector trigger is fully efficient for short distances between the shower and the detector. At larger distances the trigger probability decreases. The trigger threshold and the exposure can be altered by a systematic shift in the assignment of the shower primary energy. A set of fiducial

volume cuts can be used to limite the available detection volume to a region in which the fluorescence trigger is saturated even if the energy scale is changed within the known systematic uncertainties:

$$D_{max}[km] \leq \begin{cases} 24 + 14(\epsilon - 18.7) & \text{for } \epsilon \leq 18.5 \\ 24 + 14(\epsilon - 18.7) + 6(\epsilon - 18.5) & \text{for } \epsilon > 18.5 \end{cases} \quad (3.3)$$

The displayed parameters are those corresponding to the new energy scale. Different hadronic interaction models predict different fractions of shower energy converted into visible light producing different energy assignments and Xmax predictions. These differences might affect the selection efficiency and lead to a model dependence in the exposure. Some tests were performed. The effect is lower than 2% averaged over the whole energy range, so the exposure has been calculated averaging the Monte Carlo samples simulated with the different interaction models for the total energy spectrum.
SD data are unaffected by the distance to the FD-site, light attenuation or clouds, so the FD trigger and selection efficiency can be measured directly from a set of high quality SD showers with at least one FD-site taking data. A normalization factor is observed between simulation and data of 0.92 ± 0.02 assuming a mixed composition of 50% proton and 50% iron nuclei. This could be related to an uncertainty in the on-time, or caused by the poorer energy resolution of the SD. This factor is considered in the calculation of the spectrum.

3.2 The Energy Spectrum of Light Elements

The first step to construct an energy spectrum of light elements is to select them. In this analysis, protons and helium nuclei are considered light elements. In the following section, the method chosen to select them will be explained.

3.2.1 Selection Method

The depth of the shower maximum is a variable very sensitive to the mass composition, in fact the air showers initiated by light elements reach their maximum deeper in the atmosphere, while the heavier nuclei-induced showers have a shallower maximum. In fig. 3.7, the X_{max} distributions for proton-, helium-, CNO(Carbonium-Nitrogern-Oxygen)-, and iron-induced showers are shown. For this analysis, this variable was chosen to distinguish between light and heavy primaries. On X_{max} distributions of simulated proton-induced air showers, a cut that selects the 20% of the deepest showers making up the tail of the distributions was established. X_{max} is energy dependent, so even a cut decided on this variable will have the same dependence. In each energy bin width 0.1 log(E/eV), the X_{max} cut was established, and its

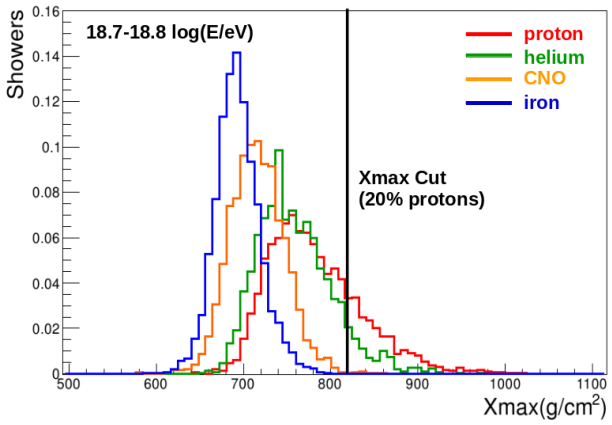

Figure 3.7: X_{max} distributions for proton-, helium-, CNO(Carbonium-Nitrogern-Oxygen)-, and iron-induced in the energy range $18.7 - 18.8$ log(E/eV), respectivily in red, green, yellow, and blue. The showers are simulated with CONEX and Sibyll as hadronic interaction model at high energies, and are reconstructed with the $\overline{Offline}$ [?].

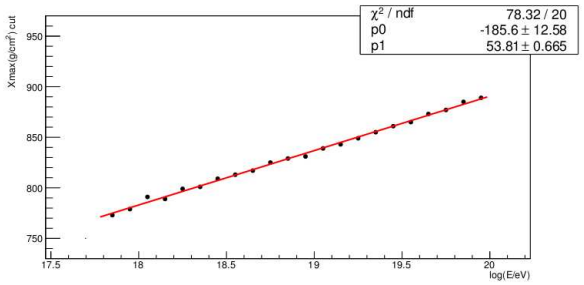

(a)

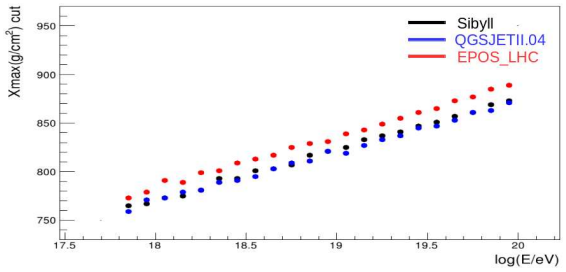

(b)

Figure 3.8: **(a)** X_{max} cut as function of the energy of primary particle. **(b)** Dependence of the X_{max} cut on the hadronic interaction models.

dependence on the energy of primary particle was fitted with a first degree polynomial (figure 3.18 (a)) to limit the fluctuations. They can be due to the uncertainty on the method used to determine the 20% of the distribution, to the low statistics in the tail, and to the uncertainty on X_{max}. For the hybrid

events reconstructed by the Pierre Auger Observatory, the X_{max} resolution is about 20 g/cm^2, so, remembering that the difference in X_{max} between the two limit cases, proton- and iron-induced showers is about 80-100 g/cm^2, the cut was established only on proton distributions so as to be in the most conservative case. The chosen percentage is the best compromise between an adequate statistics and a negligible contamination of elements heavier than protons and helium nuclei. Assuming cosmic rays are made up of the same quantities of protons, helium nuclei, and CNO, this cut selects the 20% of protons by construction, about the 7% of helium nuclei and about the 0.3% of CNO.
As already pointed out, the development of air showers, and so the depth of its maximum, is stronly dependent by the hadronic model used for the simulation. In this analysis, three different hadronic models were considered: Sibyll2.1 and the two models, EPOS_LHC and QGSJET-II.04, in which the LHC measurements were added. Fig. 3.18 (b) shows the X_{max} cut as function of energy for these three hadronic models. ...aggiungere che uso CONEX a tempo fisso simulati secondo E^-1...

3.3 The Hybrid Light Spectrum

The set of cuts used in this analysis [92] is different from that one used for the all particle spectrum analysis. There are additional cuts to assure the best reconstruction of X_{max}, that is of fundamental importance in this case being X_{max} the variable used to select light elements. In fig. 3.9, the cuts are summerized. The number of events after each cut is shown, and also the selection efficiency with respect to the previous cut. The numbers are are related to the data sample from the 1st of December 2004 to the 31st of December 2012. The pre-selection cuts are requests related to the hardware status and to the atmospheric conditions. Moreover, the request on the energi threshold, E>$10^{17.8}$, is considered a pre-selection cut. After this first selection, only events with at least one triggered station of the SD remain in the data set. To avoid a possible mass-composition bias due to the different trigger probabilities for proton- and iron-induced showers, events are only accepted if the average expected SD trigger probability is larger than 95%. This cut removes about 5% of events, mainly at low energies. The classical quality cuts are applied and it is required the X_{max} falls in the FOV of the FD telescopes. Moreover, three requirements on the quality of the profiles are applied. Events with gaps in the profile that are longer than 20% of its total observed length are excluded. Such gaps can occur for showers crossing several cameras. A cut to reduce the effect of residual cloud contamination and horizontal nonuniformities of the aerosols is applied. Finally, a minimum observed track length of >300 g/cm^2 is required. The fiducial cuts are similar to those described in the previous section. As we can see in the table shown

cut	events	ε [%]
pre-selection:		
air-shower candidates	2573713	-
hardware status	1920584	74.6
aerosols	1569645	81.7
hybrid geometry	564324	35.9
profile reconstruction	539960	95.6
clouds	432312	80.1
$E > 10^{17.8}$ eV	111194	25.7
quality and fiducial selection:		
P(hybrid)	105749	95.1
$X_{\max}$ observed	73361	69.4
quality cuts	58305	79.5
fiducial field of view	21125	36.2
profile cuts	19947	94.4

Figure 3.9: Event selection criteria, number of events after each cut and selection efficiency with respect to the previous cut.

in fig. 3.9, the efficiency of this cut with respect to the previous cut is very low, about 36%.

3.3.1 Hybrid Light Exposure

For the estimation of the energy spectrum of light elements, a different set of cuts used for the mass composition analyses was applied as already pointed out. The hybrid exposure between January 2004 and December 2012 for proton and iron primary particles calculated with these cuts is shown in fig. 3.10. In the mass composition analyses, for the same reasons described above, fiducial volume cuts are used (fig. 3.10-left). They greatly reduce the number of events, and also the cut used to select light elements is very strong, so the final statistic for light elements is very low, in particular at energies above 10^{19} eV. Until this energy, the exposures for protons and iron nuclei are very similar also removing the fiducial cuts as shown in the right panel of fig. 3.10, and this is the energetic range in which the hybrid energy spectrum can be studied. At higher energies, the fluctuations are too big due to the low statistics also without the fiducial cuts. So, these cuts will be removed for the calculation of the energy spectrum of protons and helium nuclei and the exposure calculated from simulated proton-induced showers to which were applied the new set of cuts including the X_{max} cut for the selection of light elements will be used. We are interested only at the exposure for light elements, and considering the small difference between exposures for protons

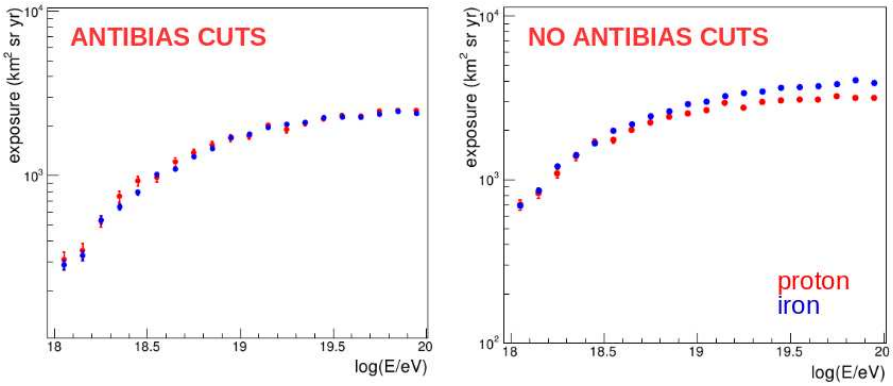

Figure 3.10: Hybrid exposure between January 2004 and December 2012 for proton and iron primary particles calculated with the cuts described in [92] in the left panel. The same exposures calculated without fiducial cuts are shown in the right panel.

and iron nuclei in the range of interest, we can assume that exposure for protons is representative also of the exposure for helium nuclei. Fig. 3.11 shows the exposure used for the calculation of all masses energy spectrum with the mass composition set of cuts in black, the exposure for protons simulated with Sibyll obtained applying the X_{max} cut, called light exposure, in red and the equivalent exposure for protons simulated with EPOS_LHC in blue. The X_{max} cut is model dependent as fig. 3.18 shows, so also the

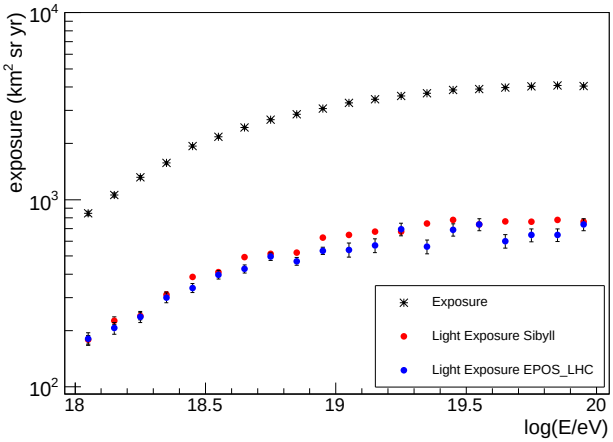

Figure 3.11: Black: exposure used for the calculation of the all masses energy spectrum, that is the mean of the exposure for protons and iron primary particles. Red: exposures for protons simulated with Sibyll used for the spectrum of light elements. Blue: exposure for protons simulated with EPOS_LHC.

exposures obtained applying this cut are different. In the following, we will

see the effect that these different cuts and exposures have on the spectrum of light elements.

3.3.2 The Auger Hybrid Light Spectrum

The energy spectrum of hybrid events measured by the Pierre Auger Observatory in the period January 2004 - December 2012 with this set of cuts was calculated and it is depicted in fig. 3.12 compared with the last published Auger combined spectrum. The agreement between them is very good. In the same picture, in blue, the energy spectrum of light elements obtained with the X_{max} cut optimized on Sibyll simulation is shown. The number of

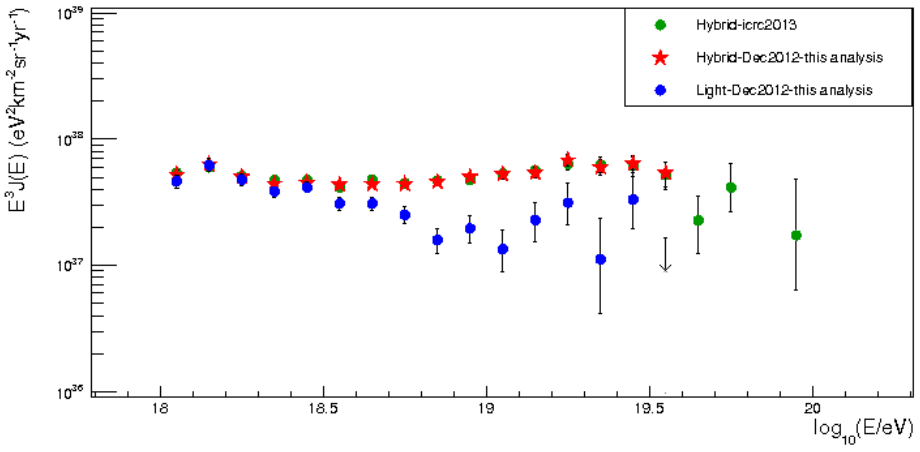

Figure 3.12: Hybrid energy spectrum from events collected between January 2004 and December 2012 on which the cuts described in [92] are applied is shown in red. It is compared with the last published Auger combined energy spectrum (green). In blue, the energy spectrum of light elements obtained with the X_{max} cut optimized on Sibyll simulation is shown.

events that pass the cuts is listed in table 3.1 for the different energy bins.

Until $10^{18.5}$ eV, the total spectrum is dominated by the light spectrum. These two spectra are very similar, their difference is about 0 as fig. 3.13 shows (blue). After this energies the light spectrum decrease. At higher energies, E>10^{19} eV, The statistic is too low to understand the shape of the light spectrum.
At this point, we will try to increas the statistics and to reduce the fluctuations removing th fiducial cuts. The distribution of the difference between the reconstructed and simulated X_{max} for proton-induced showers with and without fiducial cuts is shown in fig. 3.14. The resolution is slightly worse

energy (log(E/eV))	events	energy (log(E/eV))	events
18.0-18.1	484	18.8-18.9	21
18.1-18.2	459	18.9-19.0	18
18.2-18.3	343	19.0-19.1	8
18.3-18.4	246	19.1-19.2	10
18.4-18.5	208	19.2-19.3	8
18.5-18.6	104	19.3-19.4	2
18.6-18.7	81	19.4-19.5	4
18.7-18.8	47	19.5-19.6	0

Table 3.1: Number of events that pass the complete set of cuts and X_{cuts} cut to selects the light elements.

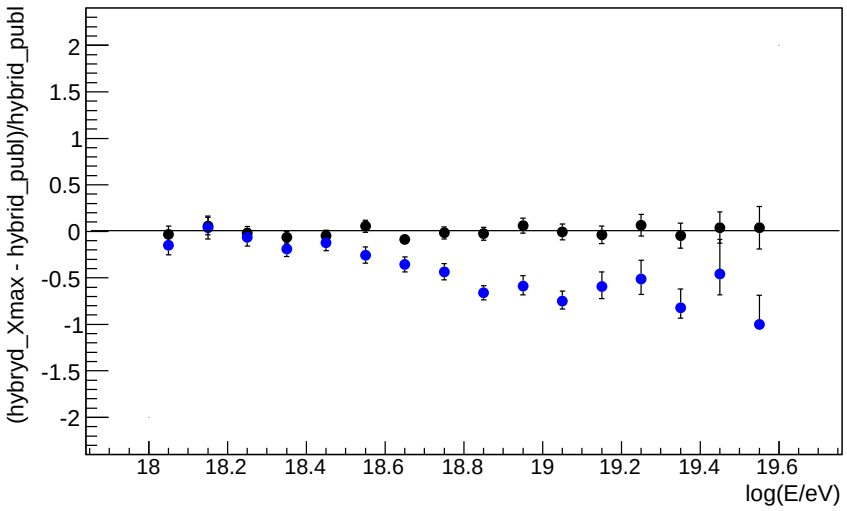

Figure 3.13: Black: relative difference between the hybrid energy spectrum of this analysis and the Auger combined energy spectrum. Blue: relstive difference between the energy spectrum of light elements obtained with the X_{max} cut optimized on Sibyll simulation and the Auger combined energy spectrum.

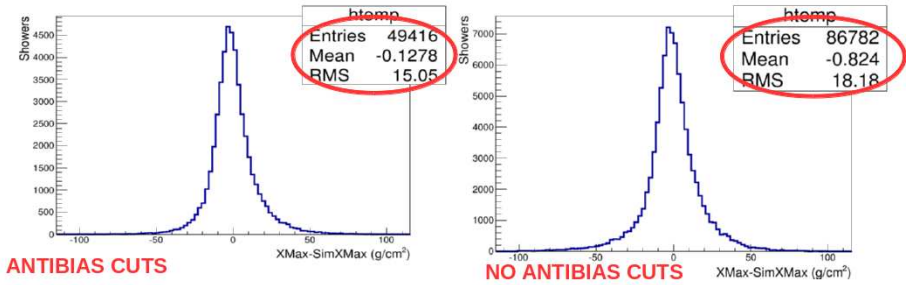

Figure 3.14: Distribution of the difference between the reconstructed and simulated X_{max} for proton-induced showers with (left) and without (right) fiducial cuts.

without fiducial cuts , but the statistic has almost doubled.
Moreover, fig. 3.15 shows the hybrid all masses energy spectrum calculated in this analysis with the fiducial cuts in red and the alike spectrum without these cuts in red. In the energy range of interest for this anlysis, the absence of the fiducial cuts does not much distort the spectrum. In fig. 3.16, the

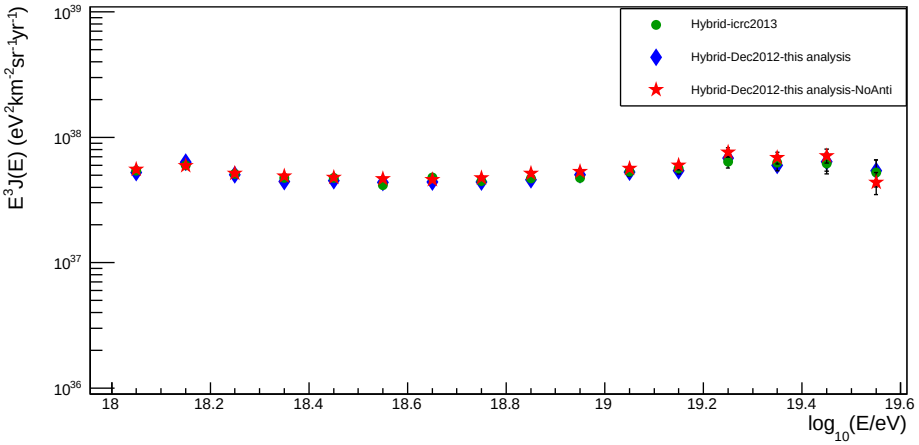

Figure 3.15: Hibryd all masses energy spectrum calculated in this analysis with (blue) and without (red) the fiducial cuts (or anti-bias cuts) in the enrgy range 18-19 log(E/eV). They are compared with the Auger hybrid spectrum.

light spectrum obtained without anti-bias cuts is shown. It is more regular with respect to the spectrum with fiducial cuts and shows clearly a cutoff after $10^{18.5}$ eV. The number of light events selected for each energy bin is listed in table 3.2.

Despite the spectrum has fewer fluctuations in this case, its slope observed at high energies is not significant yet due to the still low statistics after 10^{19}

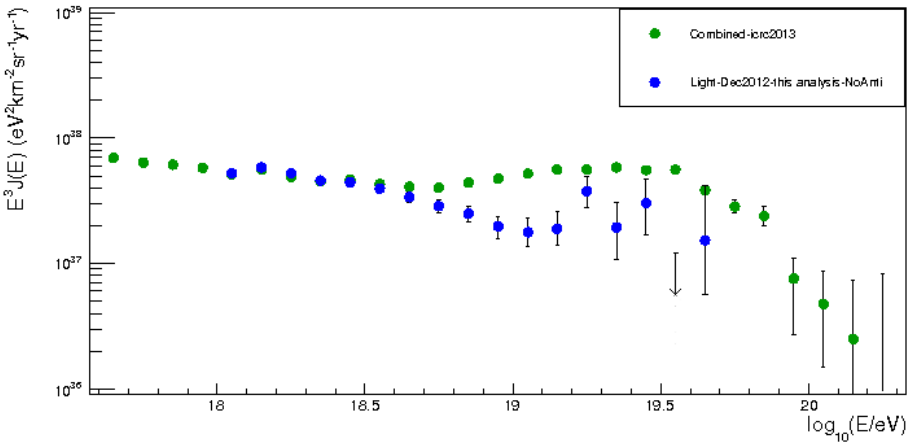

Figure 3.16: Hybrid spectrum of light elements calculated from a sample of events collected between January 2004 and December 2012. The fiducial cuts were removed and Sibyll was used as hadronic model.

energy (log(E/eV))	events	energy (log(E/eV))	events
18.0-18.1	1252	18.9-19.0	27
18.1-18.2	1016	19.0-19.1	16
18.2-18.3	770	19.1-19.2	12
18.3-18.4	543	19.2-19.3	14
18.4-18.5	405	19.3-19.4	5
18.5-18.6	239	19.4-19.5	5
18.6-18.7	146	19.5-19.6	0
18.7-18.8	87	19.6-19.7	1
18.8-18.9	52	19.7-19.8	0

Table 3.2: Number of light events that pass the all cuts, except the fiducial cuts.

eV. One more year of data was added in the calculation of the light spectrum shown in 3.17. The change in the number of light events selected can be seen

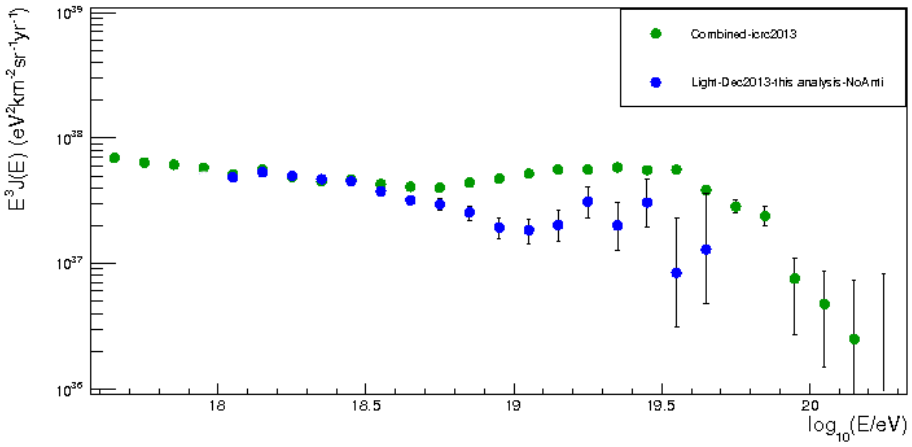

Figure 3.17: Hybrid spectrum of light elements calculated from a sample of events collected by the Pierre Auger Observatory between January 2004 and December 2013 (no anti-bias cuts, Sibyll). One more year data was added with respect to the all masses spectrum presented at ICRC 2013.

in table 4.1.

Now there is an event in the bin 19.5-19.6 log(E/eV), but to have a good statistics at high energies more than a year of data taking is necessary. To solve this problem, an attempt to use the SD data has been done as we will see in section 4.4.

3.3.3 Hadronic Model Dependence

As already pointed out, the X_{max} cut is model dependent, so the number of light events selected thanks to this cut will be different changing hadronic model. Thus far, Sibyll was used as hadronic model. At this point, we want to see as the light spectrum changes using EPOS_LHC. It predisicts a deeper X_{max} for the air showers, so we have a deeper cut as shown in fig. 3.18 (b) and a slightly lower exposure (fig. 3.11). In fig. 3.18 (a), the light spectra calculated with Sibyll (black) and EPOS_LHC (open red) are shown, while 3.18 (b) depicts the ratio between these spectra and the Auger combined spectrum. The light spectrum obtained with EPOS_LHC X_{max} cut is lower with respect to the light spectrum obtained with Sibyll and, in the first part of the spectrum, where the all masses Auger spectrum and Sibyll light spectrum are almost correspond and their ratio is close to 1

energy (log(E/eV))	events	energy (log(E/eV))	events
18.0-18.1	1429	18.9-19.0	31
18.1-18.2	1175	19.0-19.1	20
18.2-18.3	886	19.1-19.2	14
18.3-18.4	613	19.2-19.3	14
18.4-18.5	460	19.3-19.4	6
18.5-18.6	272	19.4-19.5	6
18.6-18.7	162	19.5-19.6	1
18.7-18.8	105	19.6-19.7	1
18.8-18.9	59	19.7-19.8	0

Table 3.3: Number of light events selected without the fiducial cuts.

(fig. 3.18 (b)), the ratio between EPOS_LHC light spectrum and all masses Auger spectrum is about 0.8. If the contamination of other elements is not able to overcome this discrepancy, this result could lead us to conclude that EPOS_LHC is not able to reproduce the Auger data.

3.3.4 The Contamination of Heavier Primaries

To understand the contamination of heavier primaries in the calculated spectrum of light elements, it is necessary to make assumptions about the composition of cosmic rays. Assuming that in each energy bin, cosmic rays are composed of the same quantity of proton, helium, CNO, and iron primaries, we can see the contribution and the contamination of helium- and CNO-induced showers respectively to the light spectrum. In table 3.4, the ratio between the number of events that pass the X_{max} cut in each energy bin and the number of events contained in the same bin is shown for these two primaries. Iron-induced showers contamination is totally negligible.

The contribution of helium-induced showers to the light spectrum is about 7% with respect to the 20% of proton-induced showers. The CNO contamination is very low.
At this point, we want to study a limit case. We want to observe the shape of light spectrum if the events detected by the Auger Observatory were all helium- or CNO-induced showers. The first step is to normalize the simulations to the Auger combined spectrum. The second step is to apply on the normalized showers the X_{max} cut used on the real Auger data to select the light events. The light spectra obtained in this way are shown in fig. 3.19.

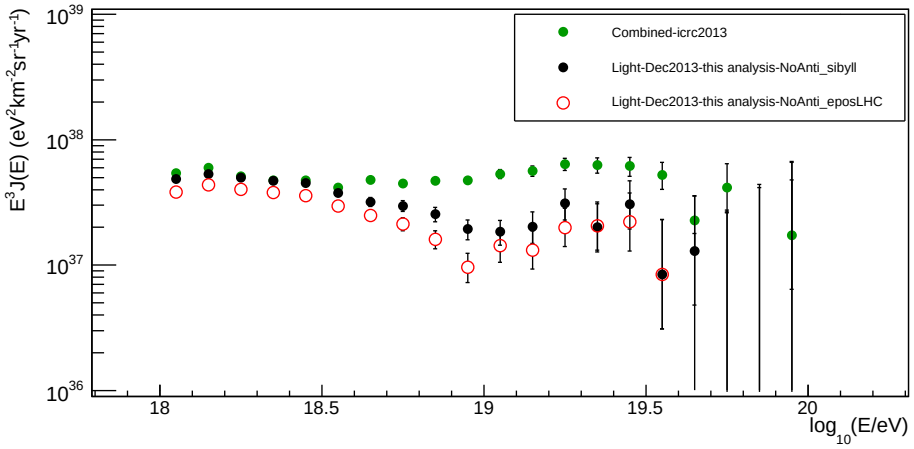

(a)

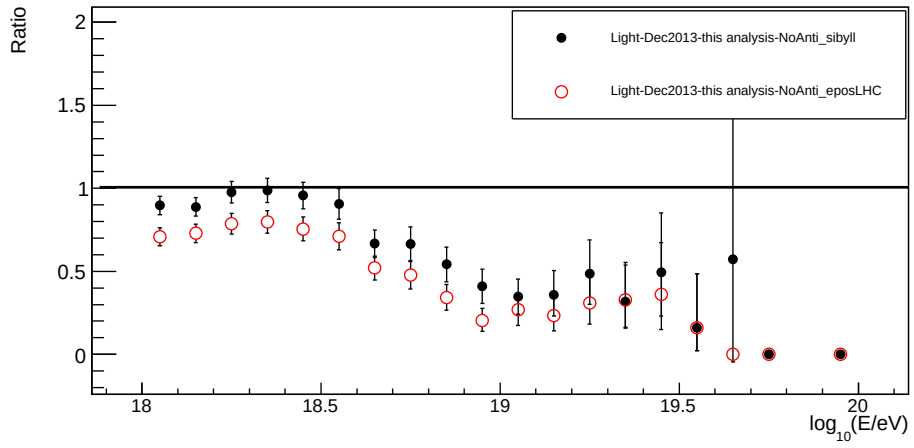

(b)

Figure 3.18: **(a)** Hybrid spectra of light elements obtained with two different hadronic models: Sibyll (black) and EPOS_LHC (open red). **(b)** Ratio between these two light spectra and the Auger combined spectrum.

At low energies, cosmic rays are constituted at least in part by protons. With increasing energy, proton primaries could disappear and the spectrum light could be dominated by helium nuclei if the proposed scenario was likely. The contribution of CNO primaries is negligible also in this limit case.
The last attempt was made to change the percentage used to establish the X_{max} cut. In this way, the constribution of helium-induced showers to the light spectrum changes. The percentages of 15, 25 and 30% were used in addition to the 20% used up to now. The spectra obtained with the 15% (black), 20% (blue), 25% (red), and 30% (violet) are shown in fig. 3.20 (a) and 3.21 (a) for EPOS_LHC and Sibyll respectivily. Ratios of the 20%,

energy (log(E/eV))	He	CNO	energy (log(E/eV))	He	CNO
18.0-18.1	0.058	0.007	19.0-19.1	0.059	0.003
18.1-18.2	0.087	0.004	19.1-19.2	0.076	0.001
18.2-18.3	0.089	0.004	19.2-19.3	0.065	0.0007
18.3-18.4	0.060	0.003	19.3-19.4	0.065	0.0002
18.4-18.5	0.065	0.007	19.4-19.5	0.066	0.002
18.5-18.6	0.071	0.003	19.5-19.6	0.061	0.0000
18.6-18.7	0.066	0.005	19.6-19.7	0.057	0.0008
18.7-18.8	0.074	0.003	19.7-19.8	0.075	0.001
18.8-18.9	0.078	0.005	19.8-19.9	0.071	0.0002
18.9-19.0	0.073	0.001	19.9-20.0	0.061	0.0006

Table 3.4: Number of light events selected without the fiducial cuts from a data sample collected between January 2004 and December 2013.

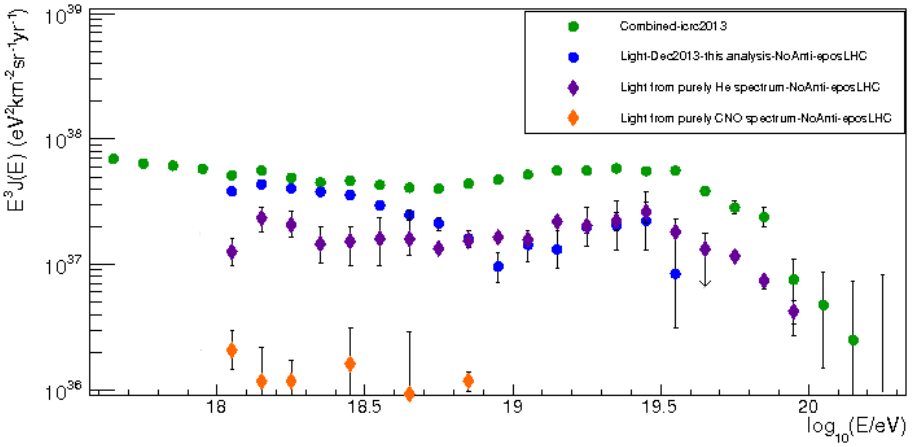

Figure 3.19: The Hybrid EPOS_LHC spectrum of light elements (blue) is compared with the light spectrum obtained assuming that all Auger data were helium nuclei (violet) or CNO nuclei (yellow).

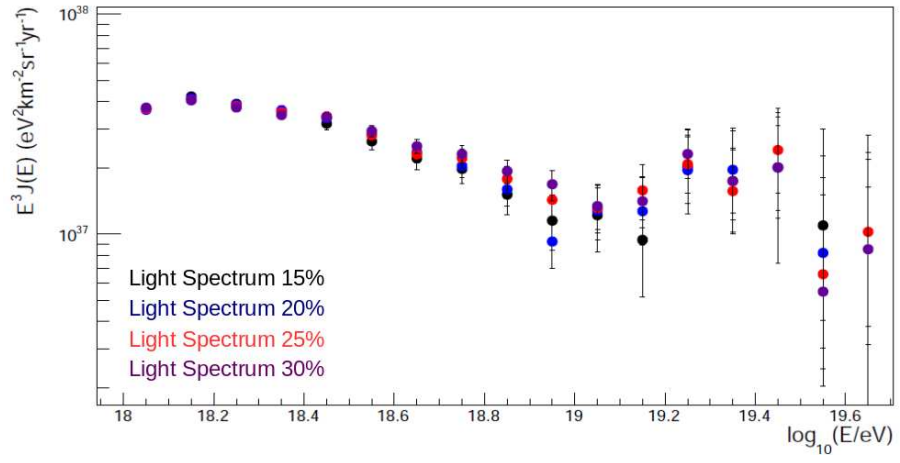

(a)

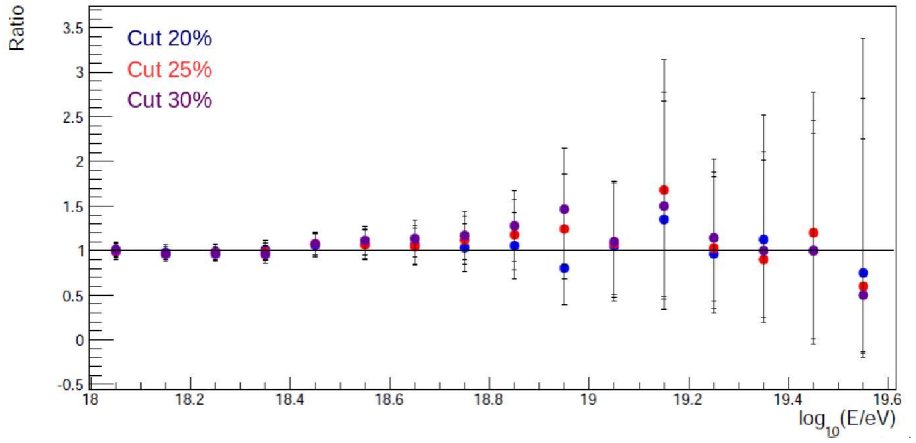

(b)

Figure 3.20: **(a)** Hybrid spectra of light elements obtained using different percentages to establish the X_{max} cut: 15% (black), 20% (blue), 25% (red), and 30% (violet). The hadronic model used in this case is EPOS_LHC. **(b)** Ratios of the 20%, 25%, and 30% spectra with respect to the 15% spectrum.

25%, and 30% spectra with respect to the 15% spectrum are shown in fig. 3.20 (b) and 3.21 (b) always for EPOS_LHC and Sibyll respectivily. Above $10^{18.4}$ eV and until 10^{19} eV, after this energy the fluctuations are too big, it is possible to see the effect of the change of percentage for both hadronic interaction models. The helium contribution increases and the spectrum is slightly higher. But at low energies, the spectra obtained with different percentages are overlapping. Therefore, remembering that the contamination of CNO-showers is negligible also in the limit case cosmic rays were all CNO nuclei, we can conclude that in the energy range 18-18.4 log(E/eV), comic ray composition is light, they are dominated by protons. Moreover,

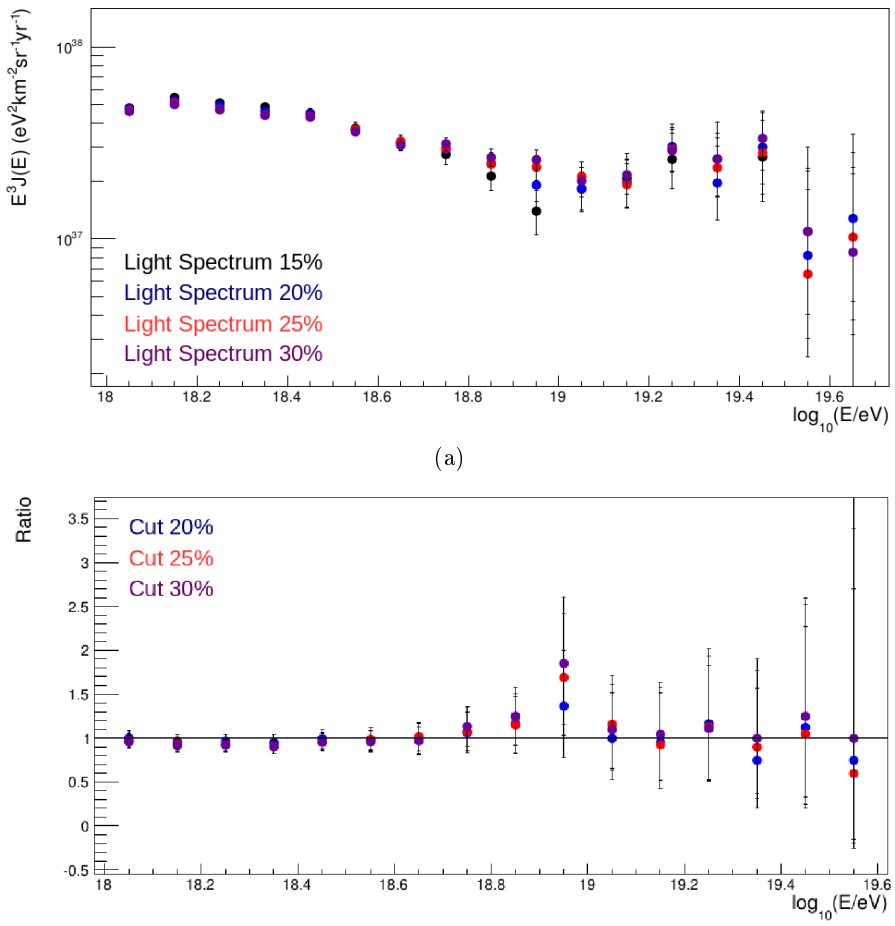

Figure 3.21: **(a)** Hybrid spectra of light elements obtained using different percentages to establish the X_{max} cut: 15% (black), 20% (blue), 25% (red), and 30% (violet). The hadronic model used in this case is Sibyll. **(b)** Ratios of the 20%, 25%, and 30% spectra with respect to the 15% spectrum.

we checked no heavier primary can overcome the discrepancy observed between the EPOS_LHC light spectrum and the Auger all masses spectrum, EPOS_LHC cannot probably describe the Auger data.

3.3.5 Comparison with another Auger mass composition work

A recent Auger analysis used the shape of the distribution of X_{max} data to infer UHECR composition [93]. For a given hadronic interaction model, the X_{max} distribution is compared to predictions made using Monte Carlo simulations formed with varying nuclear fractions, and a binned maximum-likelihood discriminator is used to choose the best-fit fractions. The data sample consists of hybrid Auger data with energy includes in the range

$E = 10^{17.8} - 10^{20}$ eV collected between December 2004 and December 2012. The cuts applied are those described in [92], the same used for the calculation of hybrid spectrum of light elements. Regardless of what interaction model is assumed, they find that Auger data are not well described by a mix of protons and iron nuclei over most of the energy range. Acceptable fits can be obtained when intermediate masses are included. The resulting proton fractions show a strong energy dependence and no significant contribution from iron nuclei is found using any model. Moreover, a significant disagreement between the models with respect to the relative contributions of the intermediate components is observed. Fig. 3.22 shows the fractions obtained for protons, helium nuclei, nitrogen nuclei, and iron nuclei with this analysis. The Auger spectrum can be multiplied by these fractions to obtain individual

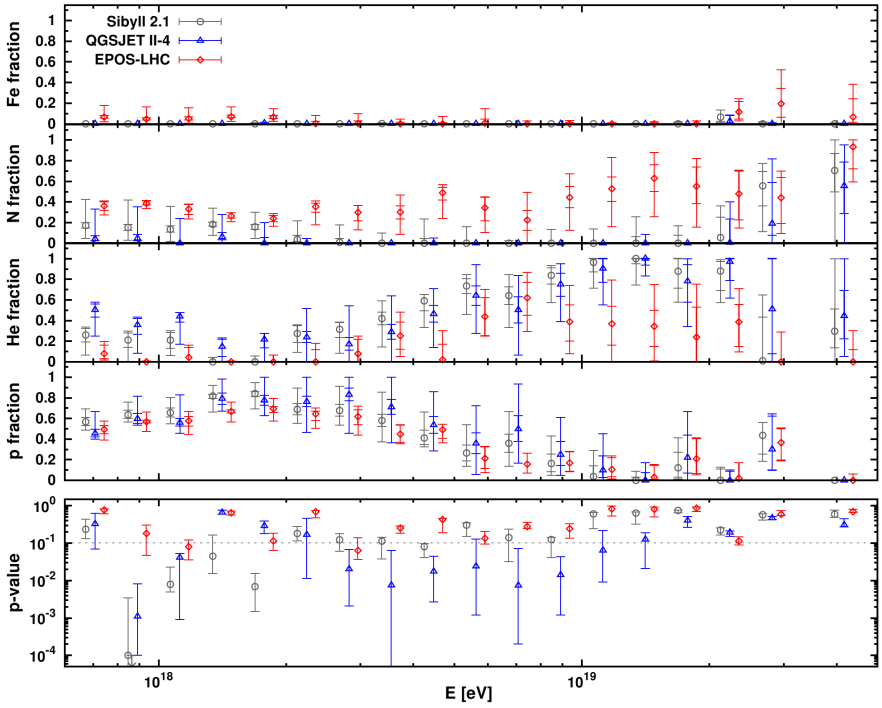

Figure 3.22: Fitted fraction and quality for the scenario of a complex mixture of protons, helium nuclei, nitrogen nuclei, and iron nuclei. The upper panels show the species fractions and the lower panel shows the p-values.

element spectra. In fig. 3.23, the spectrum of light elements obtained from the analysis described in this thesis is compared with the proton spectrum obtained from the proton fraction. At low energies, they are compatible, in fact our light spectrum is dominated by protons in the first part. In the second part, our spectrum shows the presence of helium nuclei.

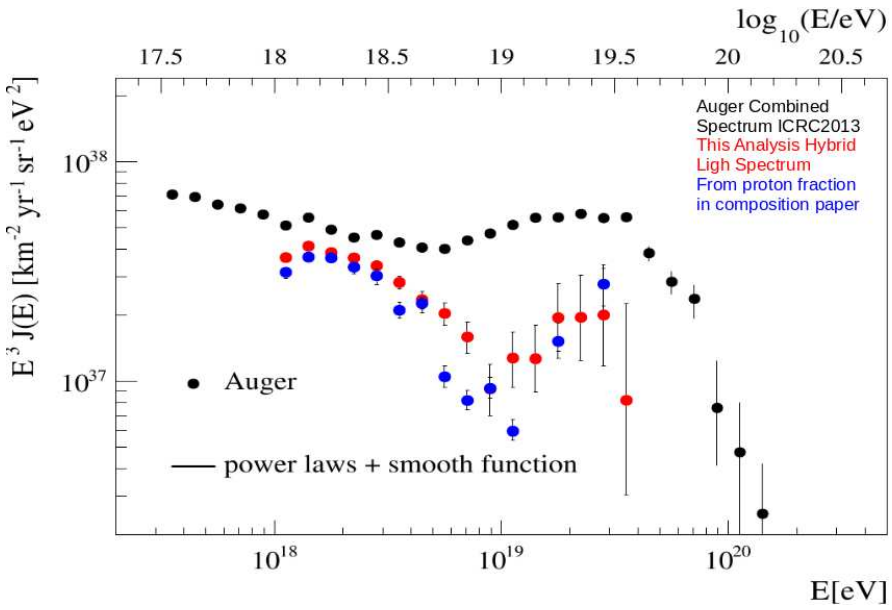

Figure 3.23: Auger combined spectrum in black. In red, the spectrum of light elements obtain from the analysis described in this thesis is shown. In blue, the proton spectrum obtain from the proton fraction estimate in [93]. EPOS_LHC is the hadronic model used for both analysis.

Chapter 4

The SD Light Spectrum

4.1 Naples Extensive Air Shower Library

For several years, the Auger Naples group have been producing the biggest library of CORSIKA showers in the Collaboration using the computing resources of the group and of S.Co.P.E. . It is an initiative of the University of Naples Federico II, founded with the goal of creating an infrastructure for supercomputing general purposes, based on the paradigm of the Grid and the latest technology of distributed computing. Several primaries were simulated: protons, helium nuclei, oxygen nuclei, and iron nuclei. The hadronic interaction model used at the low energies is fluka, at high energies EPOS_LHC, EPOS1.99, QGSJetII.03, and QGSJetII.04. Simulations covers the energy range 18.0-20.0 log(E/eV). About 5000 showers per energy bin (four bins 0.5 log(E/eV) width), per primary, and per hadronic model were produced. They follows an E^{-1} energy spectrum and are uniformly distributed in $cos^2\theta$ in zenith angle interval $\theta = 0°$-$65°$. EM component thinning was set to 10^{-6}, the observation level was at 870 g/cm^2 , geomagnetic field was set to the value of the site of the Auger Observatory in Malargüe. The development of the CORSIKA showers in the Auger detector were simulated with the v2r9p5 version of the Offline. Each shower was reused six times with the core randomly distributed over the SD array. The hybrid reconstruction of the showers was performed with the same Offline version used for the simulation, but also an only SD reconstruction was performed on a lot of these showers with the trunk-Offline version in which universality method was implemented. CORSIKA production finished, but some showers are still to be processed with the Offline. This library is available to Auger Collaboration.

4.2 Shower Universality

The *Shower Universality* says that the general features of an air shower are determined by only a few measurable quantities despite the very large number of particles it contains and the vast number of different interactions to which these particles are exposed. There is no direct dependence on primary mass, incoming direction or any other individual feature. Purely electromagnetic showers can be described knowing only their total energy E and the depth of shower maximum. The longitudinal and lateral development, the energy spectrum and the angular distribution of secondary particles around the shower axis can be predicted with these parameters. Hadronic showers, instead are described completily by N_μ and X_{max} These showers contain a large number and N_μ is a muon scale factor which accounts for the difference in the amount of muons depending on the primary mass and hadronic interaction model.
N_μ and X_{max} can be reconstructed from the SD data, that have a very higher statistics with respect to the hybrid data, thanks to the shower universality. A model of the signal in the water Cherenkov detectors (WCDs) can be developed. It allows to predict the time dependent signal $S(t)$for each shower. Two slightly different models have been developed by the Auger groups of Karlsruhe and Bariloche. Both approaches are implemented in the Offline. They starts from common assumptions, which are described below.
The relevant quantity to describe the longitudinal development of an air shower observed by a point on ground is the atmospheric grammage between this point and the position of the shower maximum, which is shown in fig. 4.1 (a) and defined as:

$$DX = X_{station} - Xmax$$

A universal model describes the electromagnetic signal by a function $S = f(X_{max}, E)$, independent of primary mass or hadronic interaction model, i.e. with no dependence on the overall muon content. Its size is given by the muonic signal simulated for a specific primary and interaction model referred to the expectation of the reference model (proton showers simulated with QGSJet II- 03) Simulations show that a significant fraction of the purely electromagnetic component stems from hadronic interactions at low-energy. This fraction is called the electromagnetic component from low-energy hadrons or the jet component. It is directly proportional to the muon content. In a very late stage of the shower development (close to the ground), jets with a high transverse momentum are produced. Those jets have a large angle with respect to the shower axis and point to stations far from the core.

Therefore, the signal recorded in a SD station must be described with four signal components: the muonic component, the purely electromagnetic component, the electromagnetic component stemming from muon interactions and muon decay, and the electromagnetic component stemming from

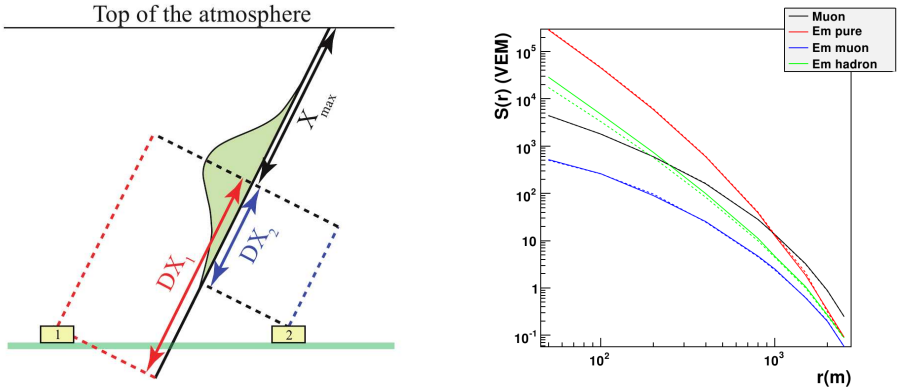

(a) (b)

Figure 4.1: **(a)** Calculation of the distance to X_{max} (DX). The density of the atmosphere is integrated from the shower maximum to the projected position of the station on the shower axis. The azimuthal asymmetry in the signal is accounted for automatically due to the difference in depth of late and early stations (DX_1 and DX_2). **(b)** The lateral distribution of the four signal components that describe the signal recorded by a SD station in the universal model.

low-energy hadrons. Their lateral shape are shown in fig. 4.1 (b).

The properties of incident particles depend on where a detector is located referred to the shower axis. The angular distribution of particles hitting detectors below the shower axis (early region) is more centered around the vertical axis than for detectors above the shower axis (late region). Furthermore, a part of the shower in the late region is absorbed by the ground before it can reach the detector. At a fixed distance to the shower core, the signal S_0 of each component is parametrized with a Gaisser-Hillas function as:

$$S_0(DX, E) = S_{max} \left(\frac{E}{10^{19} eV} \right)^{\gamma} \left(\frac{DX - DX_0}{DX_{max} - DX_0} \right)^{\frac{DX_{max} - DX_0}{\lambda(E)}} e^{\left(\frac{DX_{max} - DX}{\lambda(E)} \right)}.$$

S_{max}, γ, DX_0, DX_{max}, and λ are parametrized as a function of distance to the core.

Muons and electromagnetic particles have different propagation characteristics in the atmosphere, so the bulk of electromagnetic particles is delayed with respect to the muonic part and is spread out in time. The time structure of the four signal components depends on Xmax and distance to the core. Due to the limited number of particles in a station (except for small distances to the core), stations with the same θ, r, ψ are grouped by their distance to the shower maximum DX. Fig. 4.2 shows the time dependence of these four components in a station for proton showers at $10^{19.5}$ eV simulated with QGSJetII-03 on the left. The same dependence is shown as the average of all traces within one bin of DX on the right. The signal time-dependence

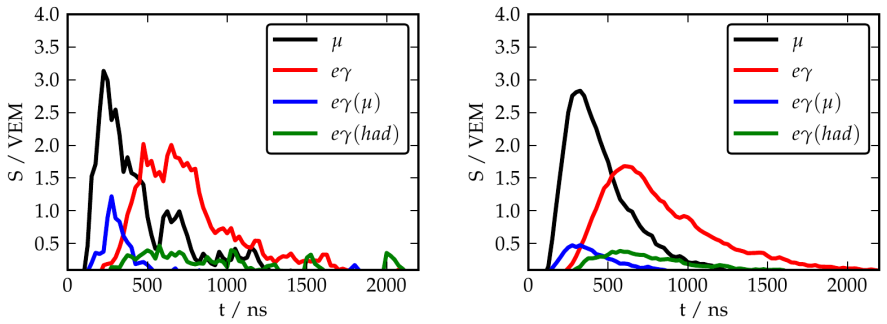

(a) Individual component traces (b) Average traces in one DX bin

Figure 4.2: Time dependence of four components used to create the universal model for proton showers at $10^{19.5}$ eV simulated with QGSJetII-03.

is described by a lognormal distribution:

$$f(t;t_0,m,s) = \begin{cases} f(t) = \frac{1}{(t-t_0 \cdot s \cdot \sqrt{2\pi})} e^{-\frac{(ln(t-t_0)-m)^2}{2s^2}} & \text{for } t > t_0 \\ 0 & \text{for } t \leq t_0 \end{cases} \tag{4.1}$$

where m represents the mean, and s the spread of the distribution, whose shape is shown in fig. 4.3. t_0 is calculated from the point of first interaction X_0. The dependence of m and s on DX is fitted.

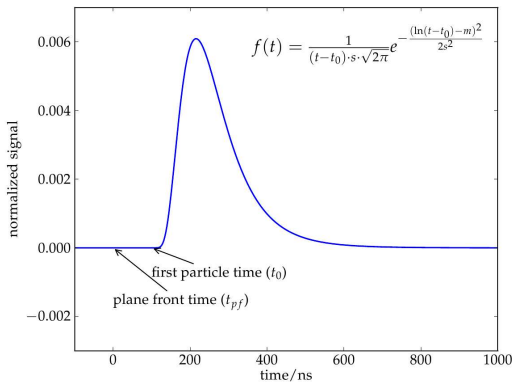

Figure 4.3: Functional shape of the lognormal distribution used to describe the time-dependence of the signal recorded by a SD station.

In the Karlsruhe reconstruction, the entire time trace is fitted with the log-normal distribution function and for the dependence of the m parameter a smoothly broken power law function is used:

$$m(DX) = p_0 \left(\frac{DX}{g/cm^2} + p_3 \right)^{-p_1} \left[1 + \left(\frac{\frac{DX}{g/cm^2} + p_3}{p_4 + p_3} \right)^{p_5} \right]^{-p2/p5} .$$

The dependence of m on DX can be attributed to p_1 and p_2 alone. Leaving the remaining parameters free does not improve the description, so they are fixed. The s parameter, instead, is fitted with a linear function:

$$s(DX) = q_0 + q_1 \cdot \frac{DX}{g/cm^2}$$

Each fit is done for all four signal components and for all combinations of r, ψ. An example of the fits for the purely muonic component at $\psi = 90°$ is given in fig. 4.4. knowing these parameterizations and fitting the various

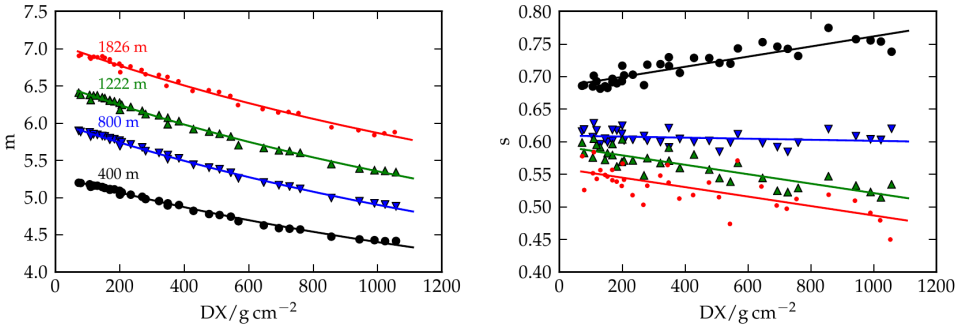

Figure 4.4: Fit of the shape parameters of the lognormal ditribution m (left) and s (right). The distance to the shower axis is color coded. Time traces from showers of all energies, primaries and hadronic interaction models are used.

components of the SD signal selected with optimized cuts , it is possible to reconstruct X_{max} also for the SD events.
In the Bariloche reconstruction, the start time is defined in a different way, it is not used the entrire trace, but the 10% and 50% quantiles and the parametrizion of the m and s dependence on DX is different. Moreover, while in the Karlsruhe reconstruction non saturated events with zenith angles up to 45° included are used and the calibration of the tank response is done using MC simulations, in the Bariloche reconstruction all events with zenith angles up to 45° included are used and the calibration is performed using golden hybrid events. I tested these two reconstruction. In the Offline version I used for the reconstruction of the showers, the Bariloche reconstruction is more robust, the bias on X_{max} introduced by the reconstruction is very small and the reconstruction is indipendent of the hadronic interaction model used for the simulations as we will se in the next section. For all these reasons, I chose to use the Bariloche reconstruction for my analysis.

4.3 The Estimated X_{max} Variable

The universality reconstruction can be used for showers with energies above $10^{18.8}$ eV. The X_{max} reconstructed from the showers collected by the sur-

face detector with the universality method will be the variable used to select showers initiated by light events. The distribution of the reconstructed X_{max} for EPOS_LHC proton-induced showers is shown in fig. 4.5. The distribution of the difference between the resconstructed and simulated X_{max} always for proton-induced showers in different energy bins (always bin 0.1 log(E/eV) width are used for spectrum analyses) is shown in fig. 4.6, 4.7, and 4.8 for QGSJetII.03, EPOS1.99, and EPOS_LHC respectivily. For all models,

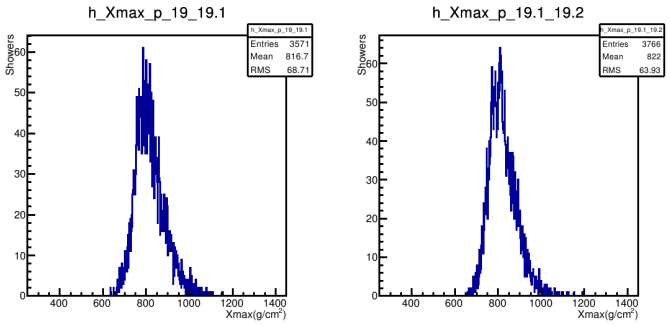

Figure 4.5: Distribution of the reconstructed X_{max} for EPOS_LHC proton-induced showers.

a small overestimation of a few g/cm^2 is observed. This offset increases at high energies but it is always lower than 15 g/cm^2.

4.3.1 SD Exposure

The aperture of the surface detector array is given by the effective area integrated over solid angle [70]. When the trigger and event selection have full efficiency, i.e. when the acceptance does not depend on the nature of the primary particle, its energy or arrival direction, the effective area coincides with the geometrical one. Fig. 4.9 (a) shows that this happens above 3 $\times$ 10^{18} eV for hadronic primaries. Above this energy, the calculation of the exposure is based only on the determination of the geometrical aperture and of the observation time. With respect to the aperture, the choice of a fiducial trigger based on hexagons, as explained in section 2.1.2, allows us to exploit the regularity of the array very simply. The aperture of the array is obtained as a multiple of the aperture of an elemental hexagon cell, acell , defined as any active detector with six active neighbours, as shown in fig. 4.9 (b). At full efficiency, the detection area per cell is 1.95 km^2 . The corresponding aperture for showers with θ<60° is then a$_{cell}$ $\simeq$ 4.59 km^2 sr. The number of cells, N$_{cell}$(t), is not constant over time due to temporary problems at the detectors (e. g. failures of electronics, power supply, communication system, etc...). N$_{cell}$(t) is monitored second by second: we show in fig. 4.10 the evolution of N$_{cell}$(t) between the start of the data taking, January 2004,

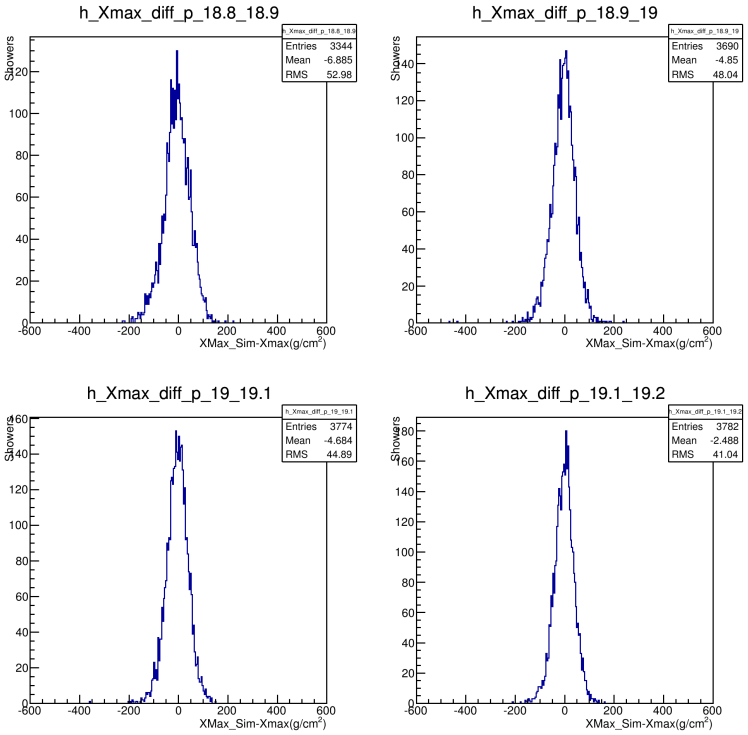

Figure 4.6: Distribution of the difference between the resconstructed and simulated X_{max} for proton-induced showers simulated with QGSJetII.03 in four different energy bins.

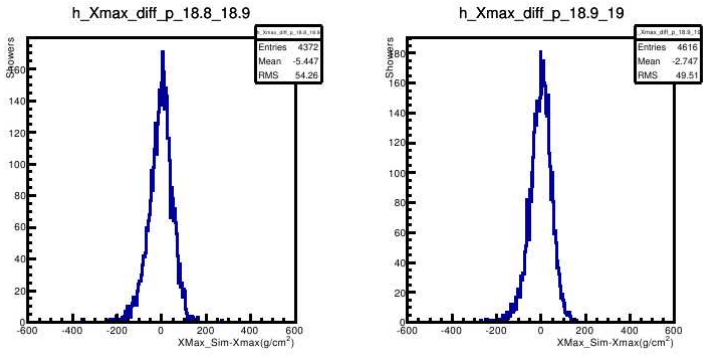

Figure 4.7: Distribution of the difference between the resconstructed and simulated X_{max} for proton-induced showers simulated with EPOS1.99 in four different energy bins.

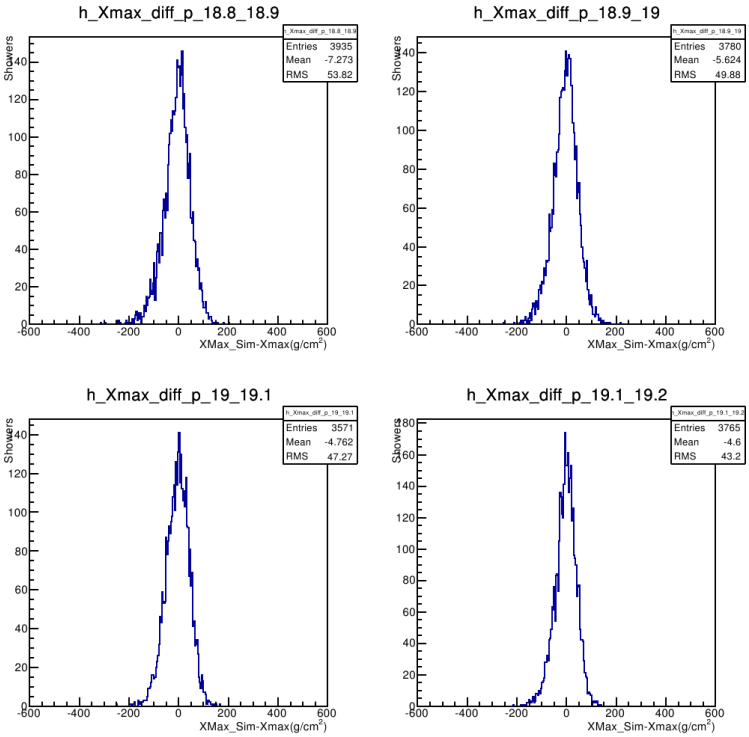

Figure 4.8: Distribution of the difference between the resconstructed and simulated X_{max} for proton-induced showers simulated with EPOS_LHC in four different energy bins.

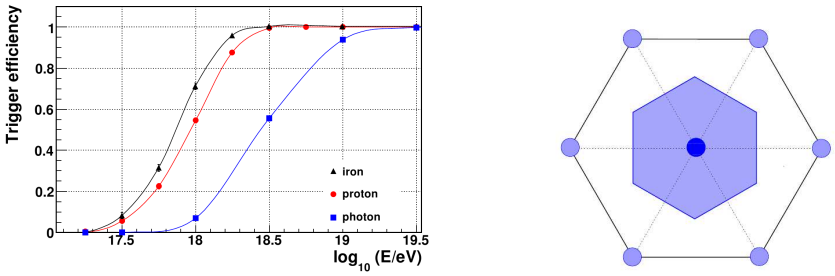

(a) (b)

Figure 4.9: **(a)** SD trigger efficiency as a function of Monte Carlo energy E for proton (circles), iron (triangles) and photon primaries (squares) and zenith angle integrated up to 60°. Lines are drawn only to guide the eyes. **(b)** Scheme of an hexagon of detectors: the elemental hexagon cell, acell , is the shaded area around the central detector.

and December 2008. The second-by-second monitoring provides at the same

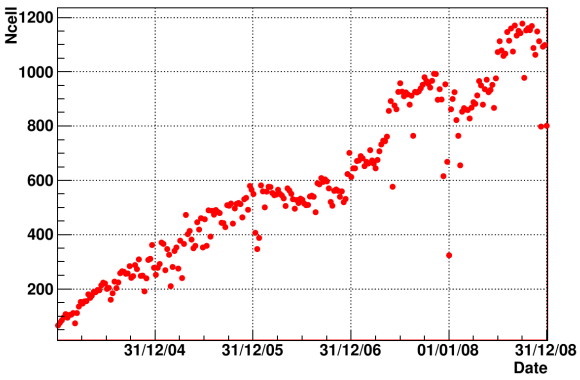

Figure 4.10: Evolution of the number of hexagonal cells (see text) between 1 January 2004 and 31 December 2008.

time the aperture of the array per second, $a_{cell} \times N_{cell}(t)$, as well as the observation time with high precision. To calculate the integrated exposure over a given period of time, the aperture of the array, $a_{cell} \times N_{cell}(t)$, is integrated over the number of live seconds. This calculation is expected to be very precise, since it is based on a purely geometrical aperture and a very good time precision. However both the determination of $N_{cell}(t)$ and of the observation time are affected by uncertainties.
Concerning the determination of $N_{cell}(t)$, to evaluate the uncertainty in the number of active detectors, a check of the consistency of the event rate of each detector with its running time, determined from the monitoring system, is performed. The uncertainty derived from this study is added to that due to errors of communication between the station and the DAQ, which are also monitored. Overall, the uncertainty on the determination of Ncell (t) amounts to about 1.5%.
For the determination of the observation time, and related uncertainty, the dead time that is unaccounted for in the second by second monitoring of the array, is taken into account. To determine these, an empirical technique is exploited, based on the study of the distribution of the arrival times of events, under the reasonable hypothesis that they follow a Poisson distribution. Given the constant rate λ for the T5 event rate per hexagon, $\lambda \approx 1.4 \times 10^{-5}$ event per second per hexagon, the probability P that the time interval T between two consecutive T5 events be larger than T is given by: $P(T) = e^{-\lambda T}$. We define intervals as dead time if the Poisson probability of their occurrance is less than 10^{-5}.
The light exposure will be the 20% of this total exposure.

4.4 The Auger SD Light Spectrum

First of all, the all particle energy spectrum from the event collected by the Auger surface detector from 1 January 2004 to 30 November 2014 was constructed. It is shown in fig. 4.11 and it represents an update of the SD energy spectrum presented at the ICRC2013. Almost two years of data taking were added. On the distributions of X_{max} reconstructed with the

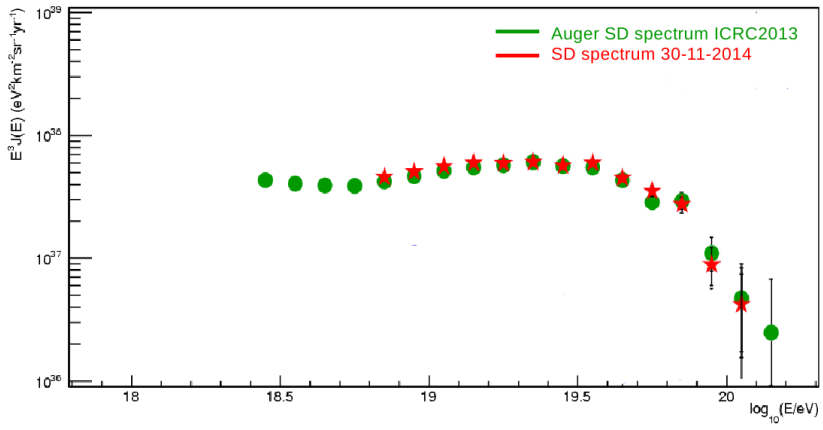

Figure 4.11: All particle energy spectrum constructed from events collected by the Auger surface detector from 1 January 2004 to 30 November 2014 (red markers). It is an update of the SD energy spectrum presented at the ICRC2013 (green markers – 1 January 2004 - 31 December 2012)

Bariloche universality method of EPOS_LHC proton-induced showers, the X_{max} cut was established in the same way described in section 3.2.1. Fig. 4.12 shows the trend of the cut with increasing energy.

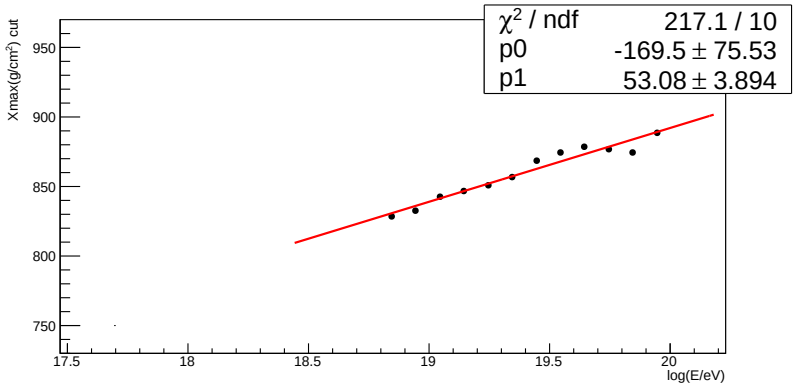

Figure 4.12: X_{max} as function of energy established from proton-induced showers simulated with EPOS_LHC.

energy (log(E/eV))	events	energy (log(E/eV))	events
18.8-18.9	444	19.4-19.5	7
18.9-19.0	269	19.5-19.6	1
19.0-19.1	157	19.6-19.7	1
19.1-19.2	73	19.7-19.8	0
19.2-19.3	46	19.8-19.9	1
19.3-19.4	15	19.9-20.0	0

Table 4.1: Number of light events selected without the fiducial cuts.

Fig.4.13 shows the X_{max} distributions of the Auger SD data in energy bins 0.1 log(E/eV) width for the whole energy range covered by this analysis, 18.8-20 log(E/eV). The energy spectrum of light elements constructed from these events is shown in fig. 4.14. The number of light elements selected with the X_{max} cut optimized on proton likely showers simulated with EPOS_LHC is listed in table 4.1.

The SD light spectrum confirms the decrease of the light component with increasing energy.

4.5 Comparison with the Hybrid Light Spectrum

Fig. 4.15 shows the comparison between the hybrid and SD light spectrum. They are compatible up to $10^{19.2}$ eV. After this energy, the SD spectrum continues to decrease and becomes hardly compatible to the hybrid one. This difference could be related to the offset of the reconstructed X_{max} as a function of the energy. This effect will be further investigated.

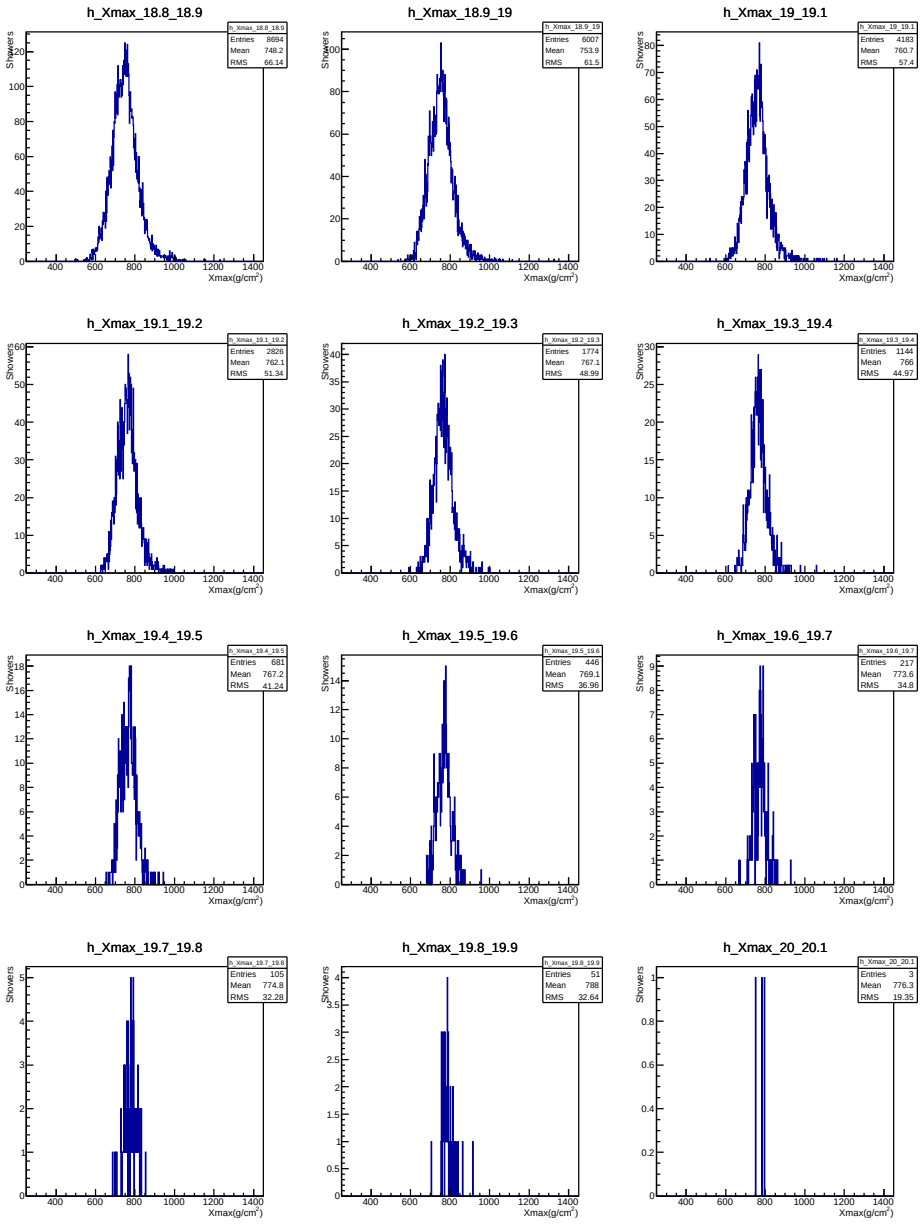

Figure 4.13: X_{max} distributions of the Auger SD data in energy bins 0.1 log(E/eV) width. For these events, X_{max} is not measured, but reconstructed with the universality method described in section 4.2.

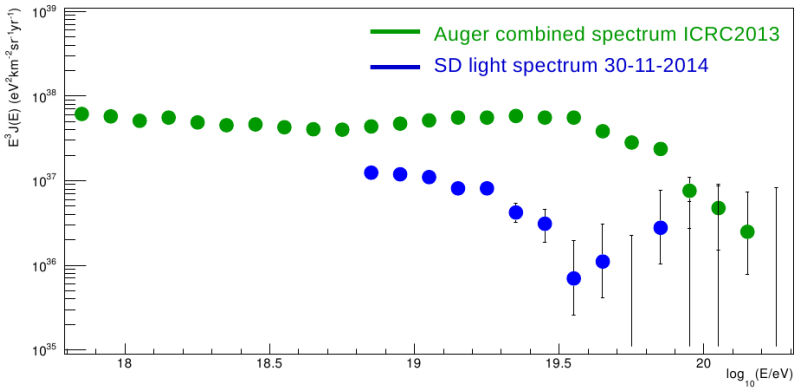

Figure 4.14: Energy spectrum initiated by light elements. It was constructed from events collected by the Auger surface detector from 1 January 2004 to 30 November 2014 on which an X_{max} cut to select light elements optimized on EPOS_LHC proton like showers was applied.

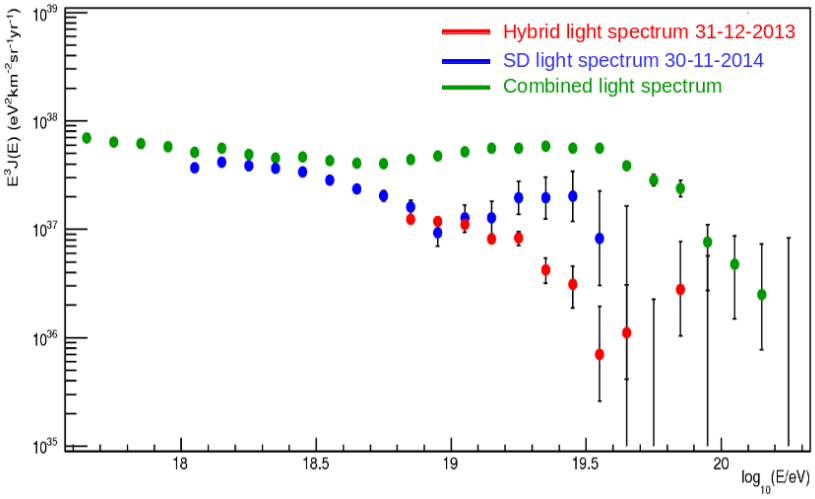

Figure 4.15: Auger Hybrid (blue) and SD (red) energy spectrum for light elements. At high energies, they are not compatible. See the text for a possible explanation.

Chapter 5

The Auger detector upgrade

In 10 years of data taking, Auger has given a lot of information about UHECRs, but many questions are still unanswered. Auger has observed clearly both the ankle at $10^{18.7}$ eV and a strong flux suppression at the highest energies. But it is not possible to understand if the suppression is related to the lack of sources which are able to accelerate CR up to these energies or to the loss of energy due to interaction of cosmic rays with CMB (GZK effect). Moreover, studying cosmic ray mass composition with the X_{max} distributions measured with the fluorescence telescopes, the presence of a large fraction of protons in the energy range of the ankle has been observed. At the same time, according to the Auger data, the anisotropy of the arrival directions of these protons cannot be larger than a few percent. This is in contradiction to the expectations for light particles produced in Galactic sources, given the current knowledge of propagation in the Galactic magnetic field. The protons at energies as low as 10^{18} eV are most likely of extragalactic origin or one has to accept rather extreme assumptions on the Galactic magnetic field. just below 10^{19} eV this proton component seems to disappear , while there may be the appearance of a component of helium component. There are also indications of a transition from helium to the nitrogen mass group at higher energy. We do not know the origin of these transitions, but most importantly we do not have enough composition-sensitive data to derive the composition at energies higher than 10^{19} eV even if we understood hadronic interactions much better than now. Finally, there are indications for a possible re-appearance of a proton component at high energy that could be related to the possible anisotropy on small angular scales observed above 5.5×10^{19} eV. The proof of the existence of a proton population at the highest energies would indicate a second class of sources, possibly distributed over cosmological distances.

About hadronic models, it is important to notice that actual models are not able to reproduce the muon content of Auger data. Auger detectors cannot measure this quantity, but they are sensitive to it. There are several methods

used to estimate the muonic component of an air shower and the result is a muonic component bigger than that produced by iron-induced showers as we can see in fig. 5.1.

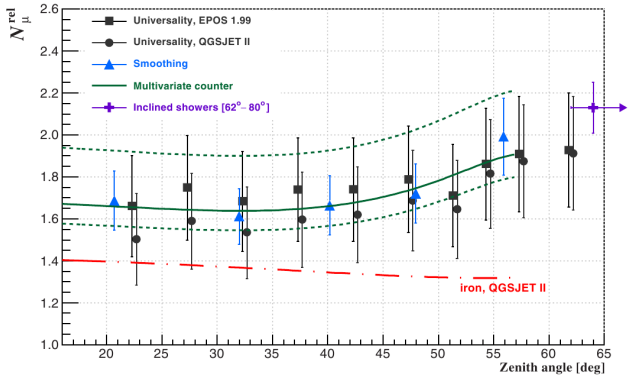

Figure 5.1: Number of muons estimated at 1000 m with several methods by the Auger data. It is relative to the predictions of simulations using QGSJET II with proton primaries at 10EeV, and it is compared to the number of muons produced by iron-induced showers. Iron nuclei are the heavier possible cosmic ray primaries.

It is planned to operate the Pierre Auger Observatory until 2023. This will triple the statistics respect data collected until end of 2012. However, increasing the statistics of the measured showers will not be sufficient to answer the key questions outlined above. So, an upgrade of the Pierre Auger Observatory has to provide additional variables which can help to investigate better the open problems.

5.1 The Scientific Goal

The Pierre Auger Observatory upgrade has to optimized to address the following questions:

1. the origin of the flux suppression and the mass composition at the highest energies have to be understood. This is a natural evolution of the original objective of the Pierre Auger Observatory, which was motivated primarily by the question of the existence of a GZK-like flux suppression. Understanding the origin of the flux suppression will provide fundamental constraints on the astrophysical sources and on the fluxes of neutrinos and gamma-rays at ultra-high energy;

2. the existence of a flux contribution of protons up to the highest energies has to be proved. To reach this aim, it is necessary a sensitivity to a contribution as small as 10%. The knowledge of the fraction of protons in UHECRs is of fundamental importance to estimate the physics

potential of existing and future cosmic ray, neutrino, and gamma-ray detectors and to predict better the flux of secondary gamma-rays and neutrinos due to proton energy loss processes;

3. the mass composition of UHECRs is strictly related to the understanding of extensive air showers and hadronic models. As already pointed out, actual models present a muon deficit respect to Auger data. Therefore the third key science objective will be the study of extensive air showers and hadronic multiparticle production.

To accomplish these science objectives, it needs to improve the sensitivity to the chemical composition until the region of the flux suppression. The most promising way to reach this aim is the discrimination between the electromagnetic and muonic components of the shower with ground-array measurements. The number of muons in an air shower is a very sensitive variable to mass composition and its measurements can help to put constrains on the hadronic interaction models. Moreover, thanks to the knowledge of the muonic component, it is possible to improve the selection of light elements to perform composition-enhanced anisotropy studies, and the discrimination power between photon- and neutrino-induced showers and hadronic showers.

5.2 MPD Reconstruction: General Considerations on Muon Detectors

Ultra High Energy Cosmic Rays can be studied only in an indirect way by extensive air showers. Shower longitudinal profile and shower particles at ground provide information about the nature and the energy of the primary particle and its interactions with the air nuclei, but unfortunately also the Auger Observatory, which is able to measure both the lateral distribution of an EAS with a water Cherenkov detectors arrays and the longitudina profile with a fluorescence detector, cannot permit a precise estimation of primary nature and hadron air cross section because there are no robust theoretical models available for energies beyond the accelerator limits. As already pointed out, detection of muons inside the shower front and the reconstruction of their heights of production along the shower axis can help to solve this problem. Muons are generated by the decay of pions produced in the hadronic interaction CR-air and carry information to the ground about this process. Reconstruction of the muon production profile along the shower axis contains information about the hard processes involved and on interaction parameters. High energy muons generated in the first interactions can be selected by reconstruction of their height of production permitting the study of primary interaction and primary mass. Fig. 5.2 shows on the left CORSIKA MPD (Muon Production Depth) distribution for a proton- and iron-induced shower. MPD seems to have a good discriminating power.

Moreover, it allows to extend the elongation rate studies at higher energies with respect to X_{max} as shown in fig. 5.2-right. The X^{μ}_{max}, the maximum depth of the MPD distribution, used for the analysis shown in this figure was reconstructed from the from the temporal trace of the signal collected in the Auger tanks. Muons which arrive at ground (Auger level) have energies

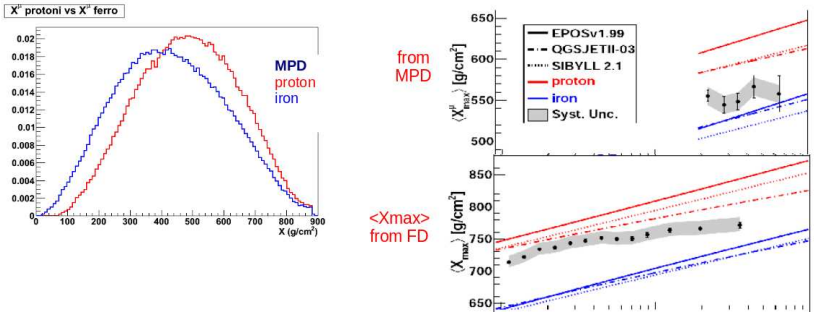

Figure 5.2: Left: CORSIKA MPD (Muon Production Depth) distribution for a proton- and iron-induced shower. Right: Elongation rate obtained from X_{max} (lower panel) and X^{μ}_{max} (upper panel). See the text for details.

greater than 200 MeV and the density of muons originating from proton and iron primary with energy E=10^{17} eV is shown in fig. 5.3.

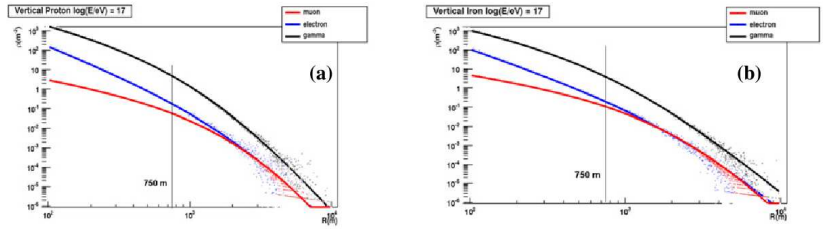

Figure 5.3: Particle density at the observation level of the Pierre Auger Observatory for vertical 10^{17} eV proton (a) and iron (b) nuclei.

Several methods to reconstruct MPDs have been proposed in literature, based on timing and geometrical properties (tracking) of EAS muons. Moreover, the Time Tracking Complementary (TTC) method was proposed by Linsley in 1990 [94]. The precision of the tracking method is reduced by the deflection of the muons in the atmosphere (effect of the geomagnetic field and of the multiple scattering) and in the detector. For the timing method, instead, the problem is muons are not relativistic as assumed by this method. Asking the coherence between the two reconstruction, it is possible to select that muons whose path in the atmosphere is compatible with the time employed to travel it, so it is possible to select the nearly relativistic and not much deflected muons. A comparison of the different

MPD reconstruction techniques at the energy of interest of the Pierre Auger Observatory was performed and the attempt to define the optimal cuts and detector requirements to measure muon component and to achieve the finest MPD reconstruction was done. Proton- and iron-induced showers simulated with CORSIKA using EPOS1.99 and QGSJET-II.03 as hadronic models were used for this purpouse. Their energy spectrum follows an E^{-1} power low and it extends from 10^{17} to 10^{20} eV. Simulations were performed in 6 energy bins 0.5 log(E/eV) width. 6000 showers per bin and primary were produced. This is an extensions to lower energies of the library used to study MARTA performances. A small sample of fixed geometry showers was used to debug and to test main properties of the reconstruction (Energy: 10^{17}, 5×10^{17}, 10^{18}, 5×10^{18}, 10^{19}, 5×10^{19}, 10^{20}; Zenith: 0, 30 and, 60°, Azimuth: 0 and 90°). A toy Monte Carlo was developed to consider reconstruction uncertainty. CORSIKA information are modified before MPD reconstruction. A gaussian fluctuation is added to core position (RMS=80 m), an angular resolution of 1.5 degree is used to fluctuate arrival direction, and the front arrival time is smeared with detector resolution. Three muon detector configurations have been considered:

- present tank: 25 ns/FADC bins;
- upgraded tank: 10 ns/FADC bins;
- RPC type muon detector: 2 ns timing accuracy, few centimeters position resolution, 1 degree direction accuracy for tracking

As first step , we will analyze the several MPD reconstruction methods ignoring uncertainties.

5.2.1 Timing

For the reconstruction with the arrival time, we use a method proposed by Cazon et al. [97].
We must start from three important assumptions: muons are produced in the shower axis, travel in a straight line and the muon velocity is the speed of light.
The muon arrival time structure is a transformation of the muon production depth distribution. Muons reach ground faster if their trajectories are parallel to the shower axis. When we fix an observation point at ground, muons produced at small MPD will deviate more from shower axis respect muons produced at large MPD, so they will cover more distance respect to muon that travel along the shower axis and there will be a major time difference between the arrival time of the core and the arrival time of muons. This difference is called *geometrical delay*. In the shower frame, the expression for the geometrical delay is:

$$ct = l - (z - \Delta) = \sqrt{r^2 + (z - \Delta)^2} - (z - \Delta) \tag{5.1}$$

where r is the distance of the muon from the shower axis, Δ is the distance between the arrival point at ground and the corrisponding point in the shower frame and z is the muon production height.
We can invert this expression to obtain the muon production height starting from the muon arrival time:

$$z = \frac{1}{2}\Big(\frac{r^2}{ct} - ct\Big) + \Delta \tag{5.2}$$

There is another delay we must take into account, a *kinematical delay*, owed to non relativistic nature of the muons (also if they reach ground with high energy). Their real velocity is lower than the speed of light, so we underestimate the real delay and overestimate the muon production height assuming relativistic muons. Kinematical delay plays an important role expecially for inclined showers. When the zenithal angle of the shower is between 30° and 60°, it is impossible to reproduce the simulated MPD if we do not take into account this delay.

A mean kinematical correction was proposed [98]. If muons lose energy, we will have a time difference respect to relativistic muons given by:

$$t_\epsilon = \frac{1}{c}\int_0^l dl' \Big[\frac{1}{\beta(E)} - 1\Big]$$

It is related to muon production energy. Since the energy distribution at a given position is known, it's possible to obtain a kinematical delay distribution and from this one, a mean kinematical delay for a given z:

$$< t_\epsilon >= \frac{1}{2c}\frac{r^2}{l}\epsilon(r, z - \Delta)$$

For practical purposes, a parametrization of the averaged kinematical delay as a function of z and r is used:

$$\epsilon(r, z) = p_0(z)^{\,p_1}$$

The new expression to calculate the muon production height will be:

$$z \sim \frac{1}{2}\Big(\frac{r^2}{ct - c < t_\epsilon >} - (ct - c < t_\epsilon >)\Big) + \Delta \tag{5.3}$$

Another method for the reconstruction with the arrival time was proposed by Erlykin et al. [95]. The difference with the technique just described is in the time definition (figure 5.4). In the Cazon et al. approach the arrival time is related to the shower front plane passing for "the detector" (red line in fig. 5.4); in the Erlykin et al. approach, instead, it is related to the front plane passing for the core. In the Ground Coordinate System, for the

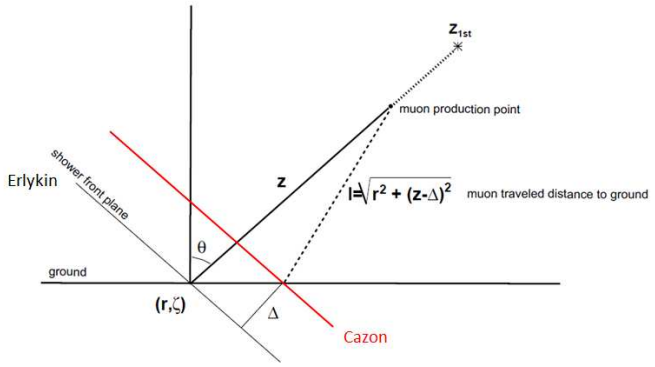

Figure 5.4: Different definition of arrival times in Cazon and Erkykin timing reconstruction methods.

Erlykin et al. approach, the muon production depth is determined in the following way:

$$h_\mu^{time} = \frac{[(x_\mu - x_s)^2 + (y_\mu - y_s)^2 - (ct_c)^2]cos\theta_s}{2ct_c + sin\theta_s[(x_\mu - x_0)cos\varphi_s + (y_\mu - y_s)sin\phi_s]} \tag{5.4}$$

where x_s and y_s are the coordinates of the shower core, θ_s e ϕ_s are the zenithal and azimuthal angle of the shower and t_c is the difference between the arrival time of the core and the arrival time of muons measured on the shower front plane passing for the core. We have a variable representation in the figure 5.5.

$$z = h_\mu^{time}/cos\theta_s$$

In the Shower Coordinate System or for vertical shower, this formula becomes:

$$z = \frac{1}{2}\left(\frac{r^2}{ct} - ct\right) \tag{5.5}$$

It is very similar to the expression (5.2) save Δ, that, how we can see in fig. 5.4, is exactly the distance between the front plane at the detector level and the front plane at the core level.
The three reconstruction are perfectly equivalent.

5.2.2 Tracking

In literature, there are two reconstructions that use the muon arrival directions. They start from a different definition of the muon production point. This ambiguity is (due to the fact that) because muons aren't produced on the shower axis.

Erlykin et al. approach exploits the triangulation method. It assumes the production point is at the minimum distance between two straight lines, the shower axis and the muon trajectory. In the Ground Coordinate System, the expression for the muon production height obtained with this method is:

$$h_\mu^{track} = \Big[(a_s^2 + b_s^2 + 1)(a_\mu(x_\mu - x_s) + b_\mu(y_\mu - y_s)) - (a_s a_\mu + b_s b_\mu + 1)(a_s(x_\mu - x_s) + b_s(y_\mu - y_s))\Big] \times \left[\frac{1}{(a_s a_\mu + b_s b_\mu + 1)^2 - (a_\mu^2 + b_\mu^2 + 1)(a_s^2 + b_s^2 + 1)}\right] \quad (5.6)$$

where $a_s = tan\theta_s cos\phi_s$, $b_s = tan\theta_s sin\phi_s$, $a_\mu = tan\theta_\mu cos\phi_\mu$, $b_\mu = tan\theta_\mu sin\phi_\mu$ (see figure 5.5 for angle representation).

In the Shower Coordinate System, this formula becomes:

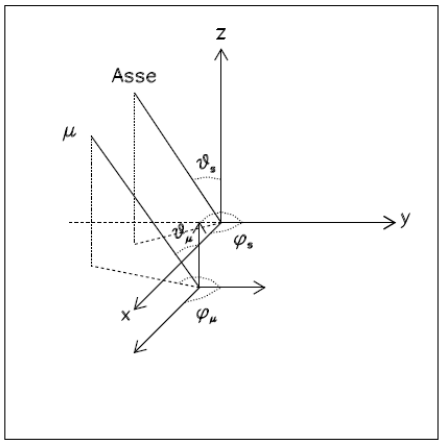

Figure 5.5: Variable representation.

$$z^{track} = -\frac{x'_\mu cos\phi'_\mu + y'_\mu sin\phi'_\mu}{tan\theta'_\mu} = -\frac{rr}{tan\theta'_\mu} \quad (5.7)$$

where x'_μ and y'_μ are the muon coordinate in the Shower Coordinate System and θ'_μ and ϕ'_μ represent the direction of the muons in the same reference system. To have a better reconstruction and select muons that are produced as near as possible to the shower axis, the following cut is used:

$$R_\mu = \frac{R - |rr|}{R} < 0.05$$

R is the distance of the muon from the core in the Shower Coordinate System. When $\varphi_\mu = \varphi_s$, so when the direction of muons is coincident with the shower

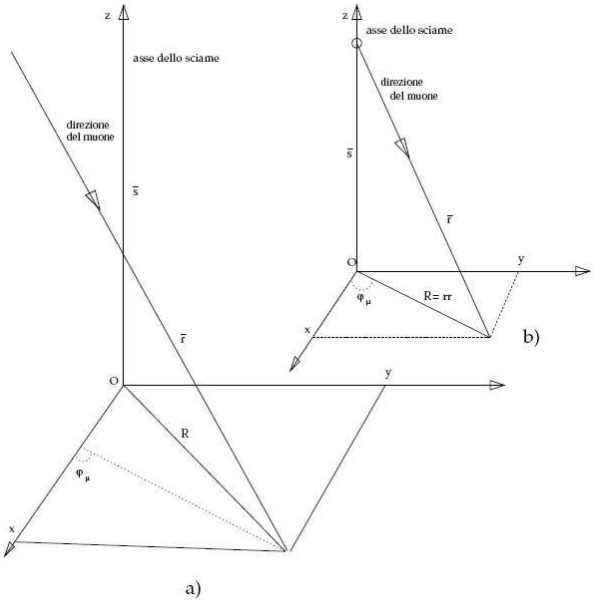

Figure 5.6: Representation of a muon which does not come from the shower axis (a) and of a muon produced on the shower axis (b).

axis, $rr = R$ (figure 5.6). For this reason, we ask rr will be nearly R.
In the Linsley approach, the muon production point is defined as the crossing point of the axis and the muon track projection on the plane connecting the axis and the point where the muon crosses the observation level. The expression for the muon production height in this approach is:

$$h_\mu^{Lin} = [(x_\mu - x_s)^2 + (y_\mu - y_s)^2](a_\mu^2 + b_\mu^2 + 1) - [a_\mu(x_\mu - x_s) + b_\mu(y_\mu - y_s)]^2 \times \frac{\sqrt{a_s^2 + b_s^2 + 1}}{[a_s(x_\mu - x_s) + b_s(y_\mu - y_s)](a_\mu^2 + b_\mu^2 + 1) - [a_\mu(x_\mu - x_s) + b_\mu(y_\mu - y_s)](a_s a_\mu + b_s b_\mu + 1)} \tag{5.8}$$

As we can see in the figure 5.7 obtained from an inclined shower with zenithal angle equal to 30°, the Linsley reconstruction gives a shift at smaller X_μ, so we have decided to use the Erlikyn et al. method.
The muon production height $h_\mu(cm)$ is turned into muon production depth $X^\mu(g/cm^2)$ with the exponential expression:

$$X^\mu = a + b \cdot e^{-h_\mu/c}$$

The parameters a, b and c change depending on atmospheric layer we are considering. In Corsika, the atmosphere is modeled by five layers. In the

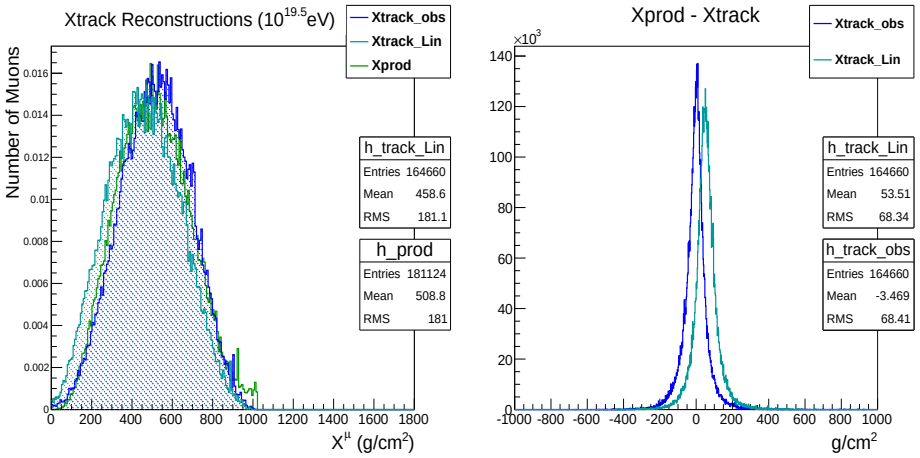

Figure 5.7: Erlykin et al.approach vs Linsley approach (MPD distribution on the left and residuals on the right).

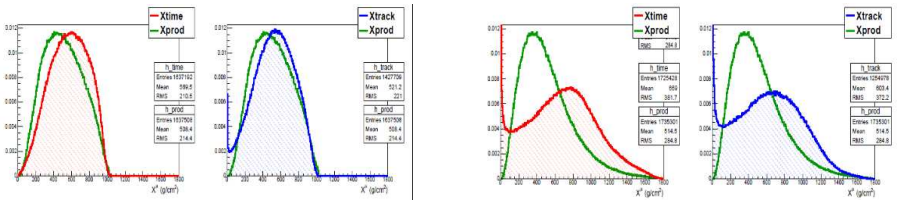

(a) (b)

Figure 5.8: Distributions of MPDs reconstructed with timing (red) and tracking (blue) method for muons with distance from the shower core greater than 500 m for a shower with $\theta = 0°$ on the left and for a shower with $\theta = 60°$ on the right.

fifth layer ($h > 100km$), there isn't an exponential dependence between h_μ and X^μ, but a linear dependence [34]:

$$X^\mu = a - b \cdot h_\mu / c$$

5.2.3 Comparison among Timing-Tracking-TTC methods

Timing and Tracking method do not work well for muon reaching ground too close to the shower core. Fig. 5.8 shows the distributions of MPDs reconstructed with timing (red) and tracking (blue) method for muons with distance from the shower core greater than 500 m for a shower with $\theta = 0°$ on the left and for a shower with $\theta = 60°$ on the right. In both cases, the distributions are distorted with respect to the CORSIKA distributions. For timing reconstruction method, close to the shower core, the geometrical delay on which the reconstruction is based is too small. Moreover, at distance lower than 500 m, other types of delay affect the time delay , only after

this distance geometric delay becomes dominant as shown in fig. ??. So the

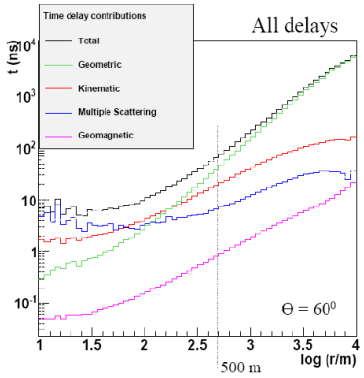

Figure 5.9: Time delay contributions as function of the distance from the shower core.

minimal cut is r>500 m. Also the tracking approach fails close to the core because of the effect of magnetic field. Muons closer to the core are the least energy. For these reasons and for reasons related to the uncertainty on the shower core that we will see later, we decided to work at distances from the shower core greater than 2000 m.
For vertical shower ($\theta = 0°$), assuming r>2000 m, both timing and tracking method work well as shown in fig. 5.10. The correction for the kinematical delay improves the timing MPD distribution, but this correction is not essential. For showers with $\theta = 60°$, the distributions are distorted respect to the simulated distribution (fig. 5.11). For the timing method, the correction for the kinematical delay eliminates the distortion, but we are applying an average correction so, in this way, we cannot recover informations on single muons. Requiring the coherence between timing and tracking reconstruction, i.e. asking that the difference between the timing and tacking reconstruction is less than 50 g/cm^2, the TTC reconstruction MPD distribution reproduce again the CORSIKA MPD shape (fig. 5.12). TTC muon production depth is defined as:

$$X_{TTC} = \frac{X_{time} + X_{track}}{2}, \qquad |X_{time} - X_{track}| < 50 g/cm^2$$

As already pointed out, the TTC request allows to select the nearly relativistic and not much deflected muons. The MPD distribution of these muons has a different shape with respect the total MPD distribution, but in fig. 5.13, it is possible to see that we are able to reproduce this new MPD distribution perfectly thanks to TTC method (cyan distribution with respect to pink distribution, that is the simulated MPD distribution on which TTC cut was applied). Observing the distribution of the difference between recontructed and simulated MPD for the three methods in fig. 5.13, we can conclude that

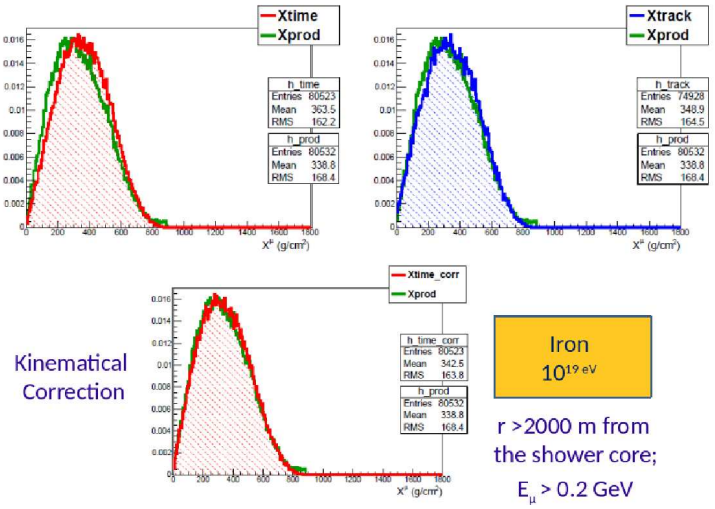

Figure 5.10: Reconstructed MPD with timing method in red with (bottom) and without (top) correction for kinematical delay. Reconstructed MPD with tracking method in blue. They are compared with the CORSIKA MPD in green. A vertical shower initiated by a iron nucleus with E=10^{19} eV was used. Only muons with a distance from the shower core greater than 2000 m and E>0.2 GeV were selected.

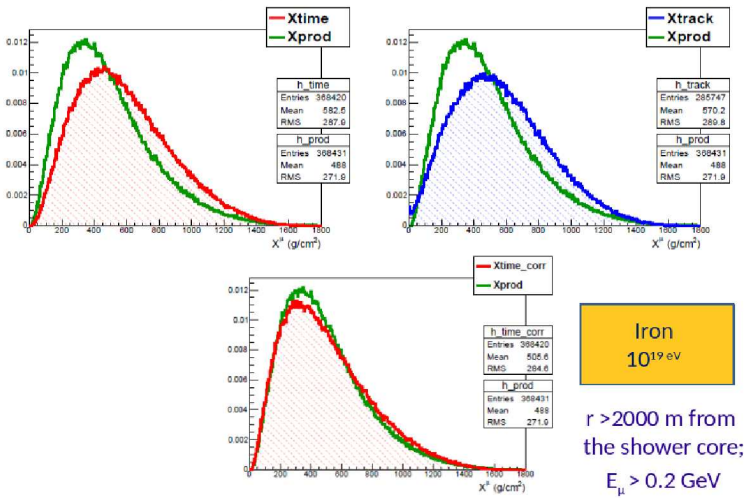

Figure 5.11: This figure is the equivalent of fig. 5.10 for a shower with $\theta = 60°$.

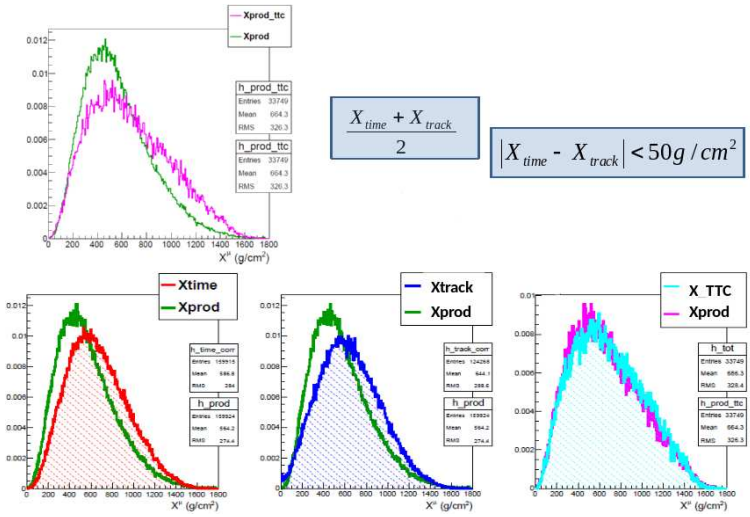

Figure 5.12: Top: CORSIKA MPD (green) compared with CORSIKA MPD on which TTC requests were applied. Bottom: MPD reconstructed with timing method (left), tracking method (centre), TTC method (right) for an iron-induced shower with $\theta = 60°$.

TTC method has the best performances, it improves the accuracy of the muon production depth estimate, and that it is probably the only way to work with the single muon for inclined events. In 2012, a possible evolution

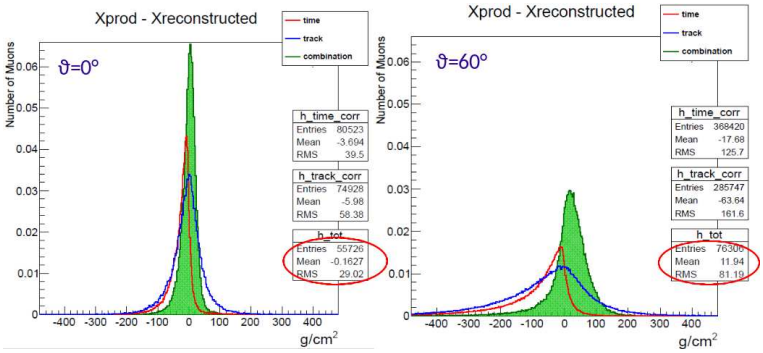

Figure 5.13: Difference between recontructed and simulated MPD for timing, tracking, and TTC method.

of the Auger infill subarray including seven RPC telescopes for tracking and timing of muons spaced according a 1.500 m grid [99], but this project has a cost too high , above all considering that it would be important to cover the whole surface of the Pierre Auger Observatory to arrive at the recostruction of MPD distribution for the showers of higher energy.

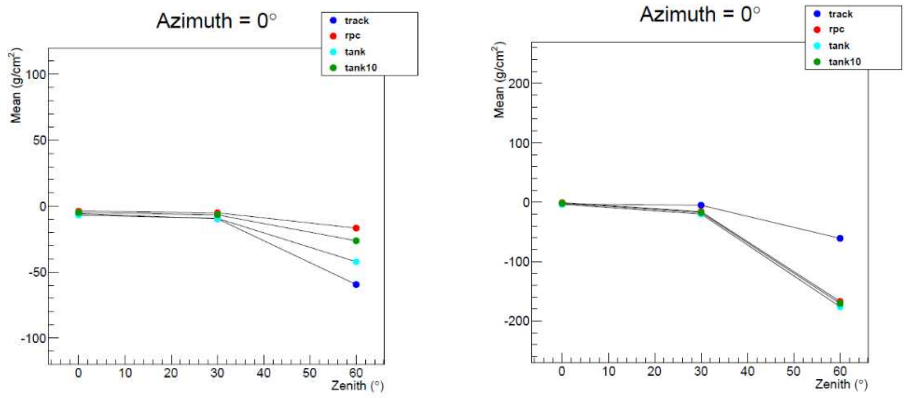

(a) (b)

Figure 5.14: Mean of the distributions of the difference between reconstructed and simulated MPD as function of the zenith angle is shown for showers detected by the present Auger tanks (cyan), the upgraded tanks (green) and RPCs (red) ignoring (a) and considering (b) the uncertainty on the shower core.

5.2.4 Detector Effect on the Timing Approach

At this point, we would like to understand what is the detector resolution to have the best MPD reconstruction. We tested three possible detectors as explained above and we can conclude that a faster detector can help, expecially at large angles, but only if the resolution of the reconstructed shower core it is not too big. In fig. 5.14 (a), the mean of the distributions of the difference between reconstructed and simulated MPD as function of the zenith angle is shown for showers detected by the present Auger tanks, the upgraded tanks and RPCs ignoring the uncertainty on the shower core. Fig. 5.14 (b) shows the same means, but in this case the uncertainty on the shower core is considered. It covers the improvement on the MPD reconstruction related to a better time resolution. This can be explained considering that for a vertical shower, and muons produced at ∼10 km, a core displacement of 50-100m, comparable with the Auger uncertainty on the shower core, easily produces uncertainties of tens of nanoseconds on their arrival time.
Therefore, for the MPD reconstruction, it is not important to have a muon detector with the best time resolution, but with the best muon idrntification capability.
The effect of the detector sampling must be considered yet. The Auger tank positions were added in our simple MC and the shower cores were randomly distributed in a 15km radius circle at the center of the array. For the unthinning [100], the same technique implemented in the Offline was used. The MPD distributions for timing and tracking method obtained from 100 vertical iron-induced showers at 10^{19} eV detected by the "Auger tanks" are shown in fig. 5.15 (a). Fig. 5.15 (b) shows the distribution

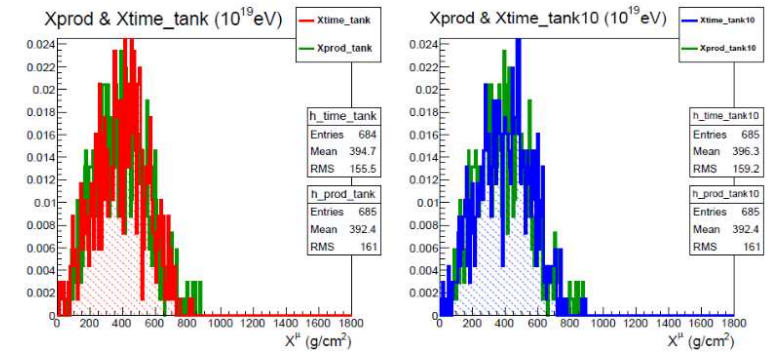

(a)

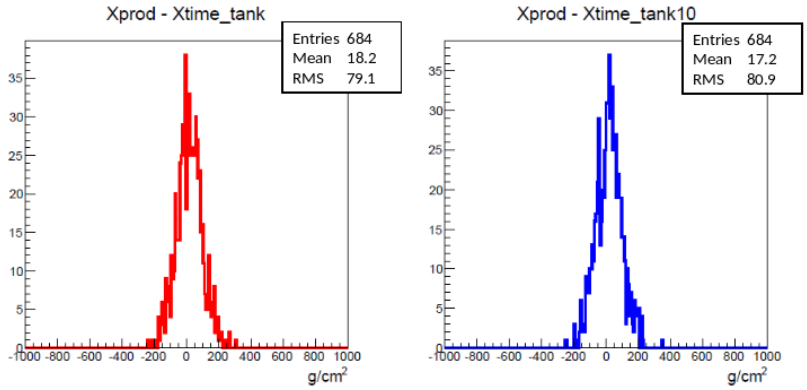

(b)

Figure 5.15: Timing and tracking MPD distributions (a) and distributions of the difference between reconstructed and simulated MPD (b) for 100 vertical iron-induced showers at 10^{19} eV detected by the "Auger tanks".

of the difference between reconstructed and simulated MPD for the same showers. Very few muons fall in a tank and for each shower, the tanks hit by muons are about 5 or 6 without analysis cuts (see fig. 5.17). The sampling effect on a single vertical shower is shown in fig. 5.16. Fig. 5.17 shows the tanks hit by muons and their multiplicity (number of muons per tank) for an iron-incuced shower at 10^{19} eV. A segmented detector could help dealing with high multiplicities. Moreover, the cuts used are very strong and, if the uncertainty on the shower reconstruction get smaller, we could try to make them less severe and recover muon statistics. In particular, we could try to release the cut on the distance from the shower core, r>2000 m. We decided this cut because only at distance larger than 2000 m, we have a geometric delay bigger than 10 ns, i.e. the uncertainty produced on the muon arrival time by the uncertainty on the shower core.

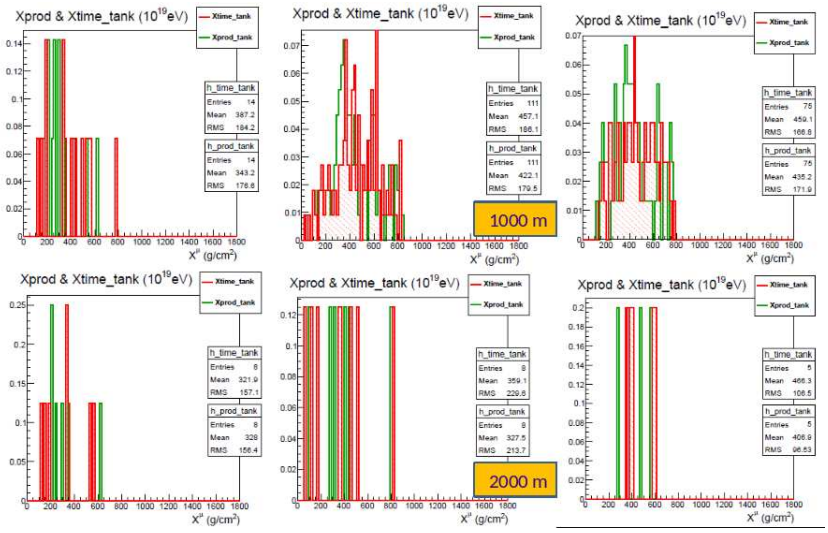

Figure 5.16: Effect of the detector sampling on a single vertical shower.

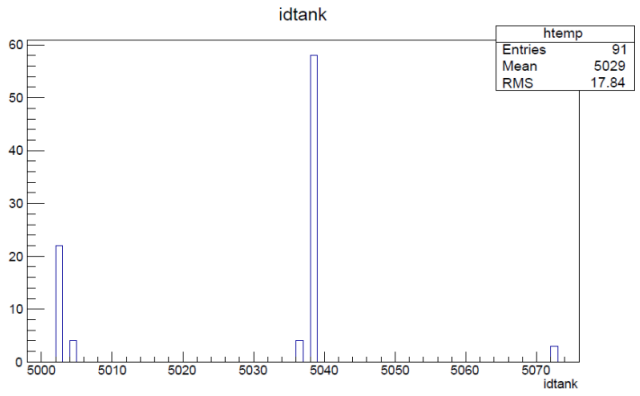

Figure 5.17: Tanks hit by muons and their multiplicity for an iron-incuced shower at 10^{19} eV.

5.3 Proposed Auger Detector Upgrade Options

The proposed upgrade includes two components: an enhancement of the muon identification capabilities of the SD array and an upgrade of the SD station electronics to provide interfaces and data handling necessary for the muon enhancement. The proposed electronics provides a flexible interface to allow the muon upgrades and other enhancements co-located with the surface detector stations to make use of the data processing and communications infrastructure of the stations. Moreover, the aim of the new electronics system is to increase the data quality with a faster sampling for ADC traces (120 MHz), a better timing accuracy, and an increased dynamic range, to enhance the local trigger and processing capabilities with more powerful local station processor and FPGA, and to improve calibration and monitoring capabilities of the Surface Detector stations.
Several detector designs were proposed to improve the muon identification and at least one prototype for each proposal has been installed in the field from the first half year of 2014. The selection of the final upgrade design was based on the experiences gained from operation in the field, the validated performance parameters, the overall costs, and the technical feasibility and the complexity of deployment. ASCII (section 5.3.2) was chosen as upgrade detectors for the full array. While for the Complementary Array, which is thought to make direct measurements of the muon component on a small area in order to check and calibrate the ASCII measurements, the Collaboration is thinking to a buried scintillator module. In the following, a brief description of the five evaluated proposals will be given to have a general panoramic and to understand better my work in two (MARTA and TOSCA) of these proposals. Fig. 5.18 shows a schematic overview of AMIGA-Grande, ASCII, LSD, MARTA, and TOSCA.

5.3.1 AMIGA Grande

The AMIGA-Grande proposal is very much based on the experience gained in building the AMIGA scintillator detectors. These are optimized to directily measure the muon component of EAS from $\sim 10^{17.5}$ eV over an area of 23.5 km^2, while AMIGA-Grande aims at measuring the number of muons of air showers from 10^{19} eV onwards, on a event-by-event basis fully covering the 3000 km^2 area of the Auger Observatory. AMIGA and AMIGA-Grande jointly could represent a simple solution that keeps the same muon detector system from the lowest to the highest energies. The AMIGA-Grande idea is to deploy scintillator detectors with an area of 10 m^2 at 1500 m and 2600 m spacings over the 3000 km^2 of the Observatory area. At best, these detectors should be buried close to surface stations to shield the electromagnetic component of the shower and to work in conjuction with the tanks. The chosen burial depth is 150 cm, that gives the best punch-through control without

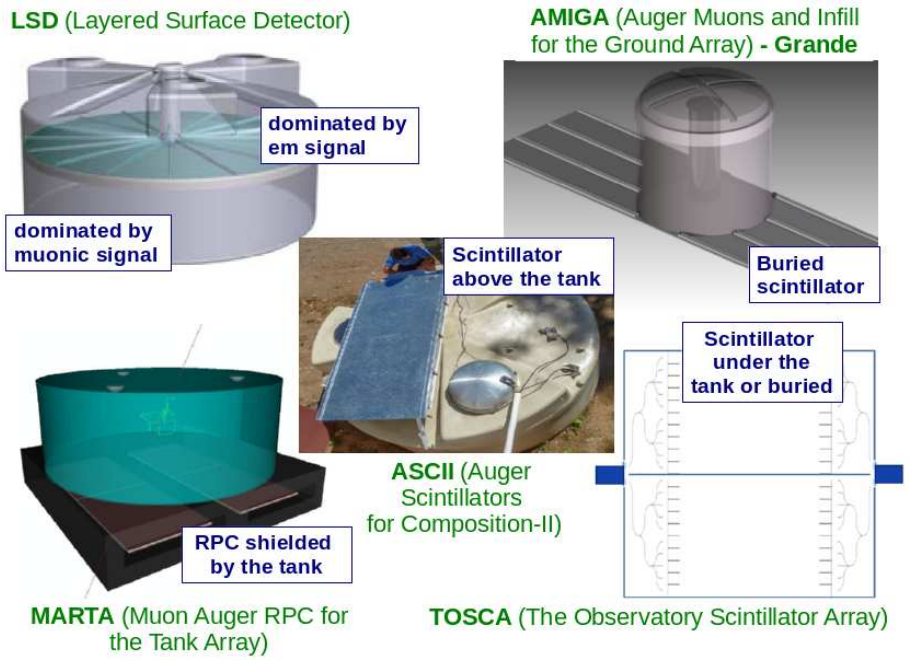

Figure 5.18: Schematic overview of the five evaluated proposals for the muon detector.

discarting a significant number of muons. The other solution is to deploy the scintillator detectors underneath the SD tanks (~ 170 g/cm^2) and add 20 cm thick slabs. The muon counters (MC) of AMIGA-Grande must be segmented systems to count muons on a very reliable and fast basis. They consist of 64 scintillators strips 400 cm long $\times$ 4.1 cm wide $\times$ 1.0 cm height with a groove on the top side where a wavelength shifter optical fiber is glued and covered with reflective foil. The fibers end at an optical connector matched and aligned to a 64 channel multi-anode photomultiplier tube. Muon counters sample scintillator signals at a frequency of 320 MHz, meaning that every 3.125 ns 64 bits are acquired. The 64 strips allows the measurement of up to 20 muons/25 ns. Following the original idea from TOSCA design concept, both AMIGA and AMIGA-Grande will now include a channel for signal integration to cope with saturated stations.

5.3.2 ASCII

The ASCII (Auger Scintillator for Composition - II) idea is to cover the water Cerenkov detectors (WCD), which are sensitive to the muonic component of the extensive air showers, with a scintillator detector, more sensitive to the electromagnetic component of the EAS, in order to have a complementary measurement. Given the large number of electrons and positrons in a cascade, its size need not be large, allowing it to be installed over the whole

array at a reasonable cost. A global fit of both detector signals based on the Universality (section 4.2) allows determination of an absolute energy scale and estimation of the muon number event by event.
The chosen design for ASCII is a 2 m^2 scintillator made by 27 bars. They are 1.8 m long, 4 cm width, and 1 cm thick and are equipped with green wavelength shifting optic fibre similar to those of AMIGA. The 27 fibres are put together and fed to a single PMT, integrating the total charge of all the bars. It is powered by a HV power supply, and the signal is split in two, one without amplification and one with an amplification of 40 to achieve a sufficient dynamic range. ASCII will sit on an aluminum structure fixed on top of Auger tank. The impact on the signal recorded by the tank is negligible because the ASCII tick is equivalent to about 2 g/cm^2.

5.3.3 LSD

Energy absorption in water Cherenkov detectors can be used to distinguish muons from the electromagnetic components of extensive air showers. LSD (Layered Surface Detector) is an application of this concept within the Auger WCD. Going more in detail, EAS electrons, positrons and photons are absorbed in water over lengths of the order of 30 cm while GeV muons can go through several meters without being stopped. Therefore, dividing the tank in two water volumes, we could have from each station a signal more sensitive to the electromagnetic component and one more sensitive to the muonic component. The bottom layer is partially shielded by the top one. The reconstruction of the EM and muonic component of the EAS relies on the fraction of the signal deposited by each component in each segment. Those fractions define a 2×2 matrix M that gives the measured top and bottom signal as a linear superposition of the EM and muon contributions:

$$\begin{pmatrix} S_{top} \\ S_{bot} \end{pmatrix} = M \begin{pmatrix} S_{em} \\ S_{\mu} \end{pmatrix} = \begin{pmatrix} a & b \\ 1-a & 1-b \end{pmatrix} \begin{pmatrix} S_{em} \\ S_{\mu} \end{pmatrix}$$

The coefficients a and b are independent of the UHECR primary type, the energy and the simulation model. They only depend on the water volume geometries.
According to the universaliy concept, the ground signal of EAS can be parametrized with a set of universal functions, from which the relevant information about the primary UHECR is retrieved. LSD allows to measure the macroscopic parameters with high precision: 10% for the visible energy, 1° for the arrival direction, 20 to 40 g/cm^2 for the shower maximum and better than 20% for the muon size. The signal from the upper layer, with its enhanced response to the EM component, can be used at the local trigger level to improve the sensitivity to photon primaries. Moreover, the measurements of the EM component has a calorimetric nature.

The two water volumes of the LSD are created by inserting a horizontal reflective layer, made of Tyvek, at an height of 80 cm from the WCD bottom. The layer is mounted on a light mechanical structure that is inserted from the top of the tank into the water volume and then unfolded like an umbrella. A central cylinder provides the mechanical structure as well as the enclosure for the phototube that collects the light from bottom layer. In the 40 cm upper layer, the light is collected by the 3 original PMTs of the tank.

5.3.4 MARTA

MARTA (Muon Auger RPC for the Tank Array) purpose is to detect muons by deploying RPCs under the tanks of the SD array. The tanks remain unchanged, and act as shielding for the electromagnetic shower component. Moreover, placing the muon detectors under the tanks allows combining the measurement of the water-Cherenkov tank and of the RPC. MARTA units will be deployed across the entire array, except for regions with loose soil or water. Triggering, timing, communication and power for the RPCs are provided by or shared with the WCDs. For each station, four RPC chambers will be installed inside the concrete structure supporting the tank. The structure is 20 cm thick (50 g/cm^2) and provides additional shielding from the shower electromagnetic component. The total area covered by RPCs is 8 m^2. Each RPC has a size of 1.2×1.6 m^2. The chamber structure is optimized for outdoor, low gas flux operation. The RPCs have two 1 mm gas gaps between 2 mm thick soda-lime glass layers which are enclosed in an aluminum case, and are equipped with 64 read-out pads of size 15×20 cm^2, for a total of 256 pads per tank. These pads allow an analogic and digital read-out. The baseline design of MARTA allows the measurement of muons with a position resolution of 15-20 cm (driven by the pad size), a time resolution of 5 ns (driven by the electronics and the GPS) and a very high efficiency. With the digital read-out only, the number of muons in each station can be directly measured down to about 400 m from the core and pile up corrections allow one to recover down to 200 m from the core. With the analog read-out (charge integration in about 100 ns for each pad) each station will accurately measure from 1 to at least 10000 muons per detector unit with no saturation. Detailed studies of the expected punch through have been performed. The material (water+concrete) which shields the RPC was mapped as a function of the position in the surface of the RPC for different direction of the incoming particles. These maps (two examples are shown in fig. 5.19) are used to define, in each case, the RPC fiducial area. The signal inside the fiducial area has a lower electromagnetic contamination with respect to the signal outside the fiducial area. The expected average number of muons in a MARTA station as a function of the distance to the shower axis is shown in fig. 5.20. For each event, the MARTA Lateral Distribution Function (LDF) is fit with the modified NKG in the range

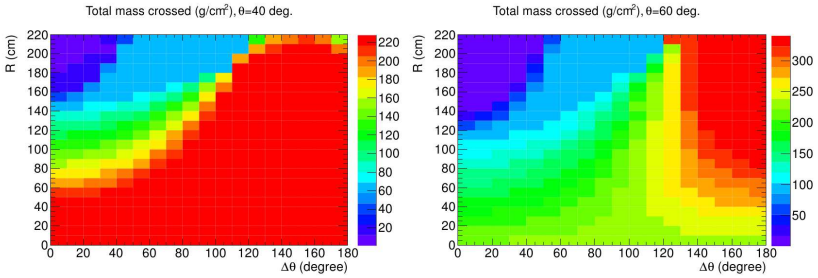

Figure 5.19: Material overburden (in g/cm^2) as a function of the position in the surface of the RPC, for zenith angles of the incoming particles of 40° (left) and 60° (right). (R, $\Delta\theta$) are the polar coordinates at the RPC surface (XOY plane) in the reference system with the origin in the tank axis (OZ) and OX corresponding to the projection of the incoming particle direction in the XOY plane. The maps were obtained by averaging over all particle azimuthal directions. For θ=0° the total material (water+concrete) amounts to 170 g/cm^2 for R $<$ 1.8 m. For θ=40°, the maximum crossed material amounts to about 220 g/cm^2 (340 g/cm^2 , for θ=60°).

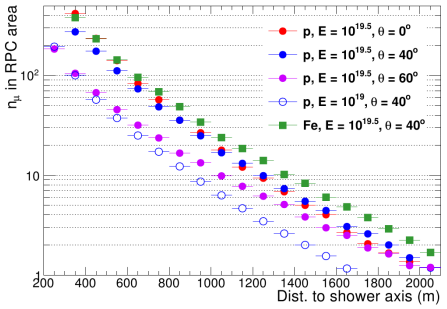

Figure 5.20: Average number of muons in a MARTA station as a function of the distance to the shower axis. Results obtained with CORSIKA showers using the full, GEANT4-based simulation of MARTA in the Offline.

[500 m,2000 m]. Fig. 5.21 shows an example of two fitted events. The

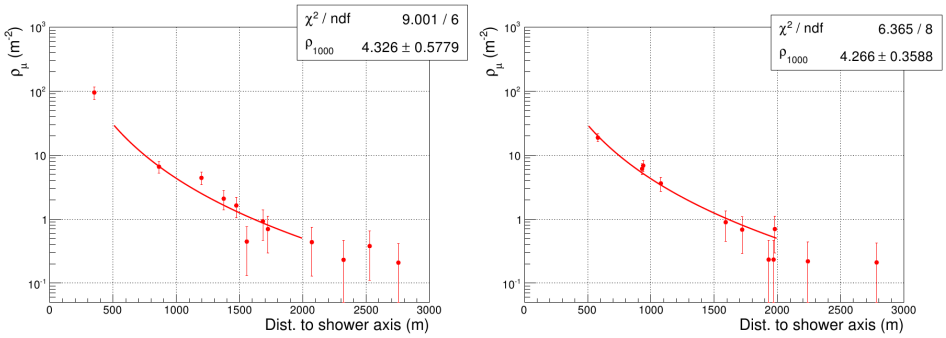

Figure 5.21: Fit to the MARTA LDF in two simulated $10^{19.5}$ eV proton showers at $\theta = 40°$.

number of muons in an air shower is obtained integrating the fitted LDF in the distance from the shower core range [500m,2000m]. The precision of MARTA in the reconstruction of the number of muons has been assessed by comparing on a event-by-event basis the number of muons reconstructed with MARTA (N_μ^{MARTA}) with the number of muons at ground in the CORSIKA simulations ($N_\mu^{CORSIKA}$), that is the sum of the weights of all muons in the same interval. There is variable effective energy threshold on the muons reaching MARTA imposed by the amount of material actually crossed by each particles, so before comparing N_μ^{MARTA} with $N_\mu^{CORSIKA}$ at ground, $N_\mu^{CORSIKA}$ must be corrected by a factor k_{Abs} accounting for the absorption of the low energy muons, which depends on the muon energy distribution and on the depth of traversed material. Fig. 5.22 shows the ratio between N_μ^{MARTA} and $N_\mu^{CORSIKA}$ before and after correcting $N_\mu^{CORSIKA}$ by k_{Abs} for $10^{19.5}$ eV proton showers at θ=40° and θ=60°.

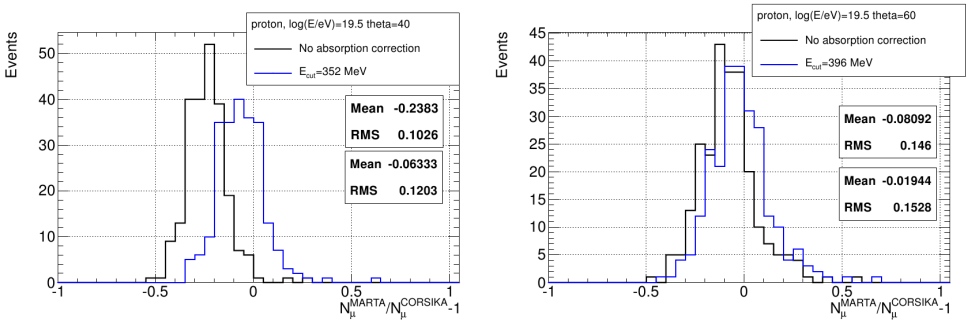

Figure 5.22: Distribution of $N_\mu^{MARTA}/N_\mu^{CORSIKA}$, before (black) and after (blue) correcting $N_\mu^{CORSIKA}$ by k_{Abs} for $10^{19.5}$ eV proton showers at θ=40° (left) and θ=60° (right). N_μ^{MARTA} was obtained by fitting the LDF for the muons in the full RPC area.

5.3.5 TOSCA

The TOSCA (The Observatory SCintillator Array) proposal aims at the measurement of the muonic component of extensive air showers using scintillator detectors equipped with Wave-Length Shifting (WLS) fibers, which can be deployed under the WCD stations. This simple and robust technique could be very effective and advantageous, especially when the muon detectors are exposed to very high particles densities near the shower core and their signals directly compared with high quality surface measurements. The suggested detector consists of a 4 m^2 plastic scintillator module, made by 50 scintillator bars holding optical fibers bundled together and read out with two small 1-1/8 inches single photocathode PMTs, one at each side. The dimensions of each bar are (4×200×1) cm. Due to the short light attenuation of the scintillator, the scintillation photons are collected by means of wave lenght shifting fibers of 1.2 mm diameter of the type proposed for the AMIGA experiment. The module electronics will be entirely integrated in the upgrade of the Surface Detector one, exploiting the 3 additional channels of the UUB (Upgraded Unified Board) dedicated to the muon module. The use of the same FADC type (120 MHz, 12 bits) both for the muon modules and the tank will allow a direct and easy comparison of the waveforms acquired in the scintillator and in the WCD station. The choice of a 4 m^2 area for the proposed module was done to have a complete shielding of the muon detector by the WCD, in order to minimize the electromagnetic punch-through. This configuration is called "Design A" and the TOSCA module is also shielded by 20 cm of concrete. In the "Design B", instead, the same module, with a larger surface of 10 m^2, is deployed close to the tank under a thicker shielding, with the obvious advantage of performing a really direct measurement of the muon component, with no electromagnetic contamination.
The merit factor of the TOSCA module, defined as the ratio between the electromagnetic component and the one depending on the muon production, is shown in fig. 5.23-left. For the "Design A", its value is $\leq$20% for core distances above 500 m. The resolution on the muon size at ground as a function of energy is shown in fig. 5.23-right. Details on the muon size estimation will be given in section 5.4. A value $\leq$30% is expected at $10^{18.6}$ eV, lowering to less than 20% above $10^{19.4}$ eV. This resolution has been obtained using the TOSCA modules alone and must be considered as an upper limit, as neither a contamination rejection was applied nor any universality based analysis was used. The performances of the array could be improved by exploiting the correlation among the signals of the WCD and those of TOSCA, following a similar technique as that suggested by the LSD team. The basic idea is to use the signal in the above WCD tank to estimate the electromagnetic contamination in the underlying scintillator and therefore to subtract the punch-through.

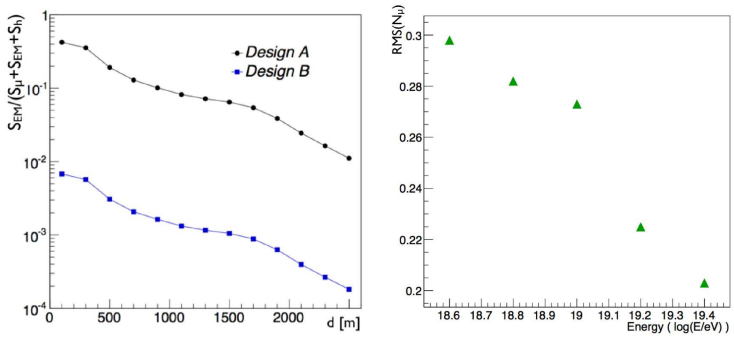

Figure 5.23: Left: Merit factor of the Tosca scintillators for the "Design A" and "Design B" for 10 EeV proton showers. Right: Resolution in the muon size with the scintillator modules as a function of energy.

5.4 TOSCA: Hadronic Discrimination

In the spring of 2013, a buried 10 m^2 muon detectors using scintillator bars with optical fibers read in integrated mode corresponding to the TOSCA "Design B" or TOSCA-B was proposed. A strong opposition to the possibility of digging holes in the 1660 positions in the Pampa was raised by the Collaboration. Therefore a second design, the "Design A" or TOSCA-A, that includes a much smaller similar detector under the tanks used as shield, has been considered in order to study the potentiality of this detector in muon meausurement anyway. In particular, I studied the performances of this detector in the proton-iron discrimination.
First of all, it is necessary to reconstruct the muon size of each shower, that is a very sensitive variable to the mass composition as already pointed out. Also in this case, to reconstruct the muon size, the muon density in the scintillator stations as function of the distance from the shower core must be fitted, in a define range of distance from the shower core, with the function:

$$\rho = k\Big(\frac{x}{1000}\Big)^{\beta}\Big(\frac{x+700}{1700}\Big)^{\gamma}. \tag{5.9}$$

k is the free parameter of the fit, while β and γ are fixed using the following functions:

$$\beta = -1.117 + 4.301cos(\theta) - 5.524cos^2(\theta) + 2.097cos^3(\theta) \tag{5.10}$$

$$\gamma = -2.178 - 5.331cos(\theta) + 2.316cos^2(\theta) \tag{5.11}$$

They are obtained fitting the β and γ dependence on cosθ shown in fig. 5.24 and 5.25 respectivily. β and γ parameters are obtained fitting the lateral distribution of CORSIKA muons in the shower reference system with

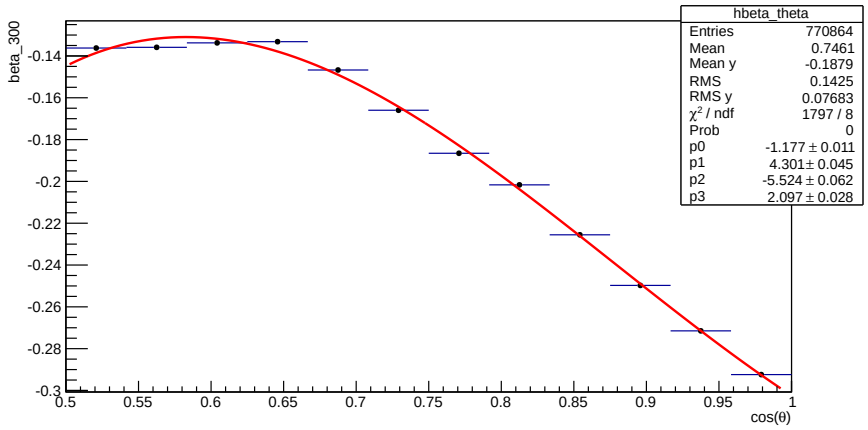

Figure 5.24: β parameters obtained by fits on CORSIKA muons at ground in the shower reference system as function of cosθ.

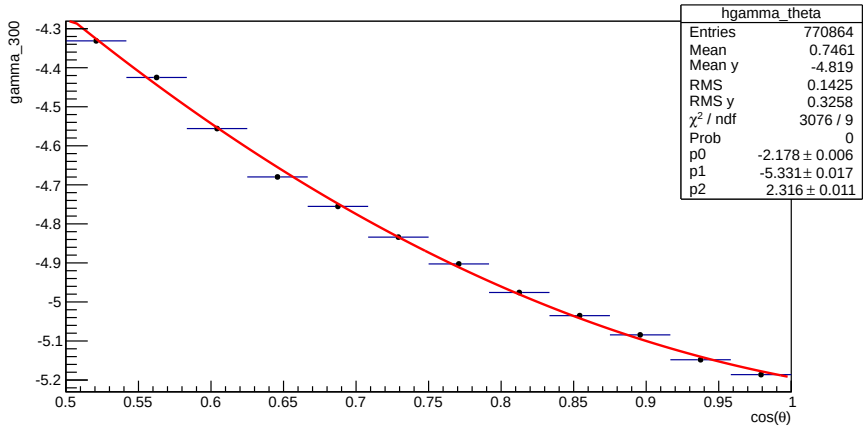

Figure 5.25: γ parameters obtained by the fit on CORSIKA muons at ground in the shower reference system as function of cosθ.

all parameters free. In this case, it is possible because without detector sampling, we have a continuous distribution. To have a reasonable muon size reconstruction, at least four stations must be used in the fit and the reduced chi-square must be less than 10. At this point, the muon size is obtained from the integral between r_{min} and 2000 m of the function:

$$2\pi x\Big[k\Big(\frac{x}{1000}\Big)^{\beta}\Big(\frac{x+700}{1700}\Big)^{\gamma}\Big],$$

where k, β, and γ have the values obtained from the previous fit. The upper limit of the integral is fixed considering the lateral dimension of the hadronic showers collected by Auger and the Auger sampling. The value of the lower limit will be defined with studies shown in the following. This muon detector should be able to work without saturating also when a great number of particles hits it. To obtain the shown example plots, we used $r_{min} = 300$ m. The calibration of the scintillator response was carried out fitting the ratio between the number of photoelectrons producing by muons collected by PMTs and the number of CORSIKA muons hitting the scintillator. The calibration curve is shown in fig. 5.26.

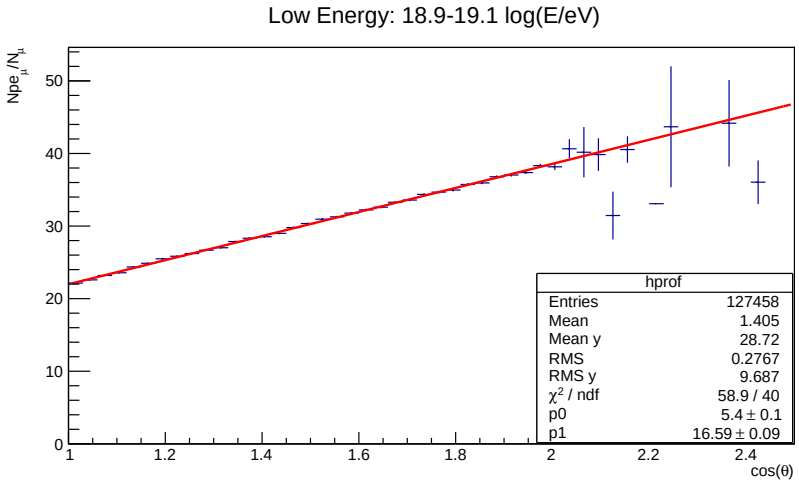

Figure 5.26: Scintillator response calibration curve.

The electromagnetic contamination level we face in the case of TOSCA-A does not allow to directly measure the muon signal in the scintillator. The reconstruction of the EM and muonic component of the EAS relies on the fraction of the energy ow deposited by each component in each of the two detectors, which are defined in the top detector (TD, the tank) as $A = S^{em}_{TD}/(S^{em}_{TD} + S^{em}_{BD})$ and $B = S^{\mu}_{TD}/(S^{\mu}_{TD} + S^{\mu}_{BD})$. By construction the fraction of the same signals in the bottom detector (BD, the scintillator) are (1-A) e (1-B). Those fractions define a 2×2 matrix M that provides the

measured signal in the tank and in the scintillator as a superposition of the EM and muon contributions (the column sum of the matrix is one by construction). We note that the B coefficient is directly defined by the relative calibration of the two detectors, so that only A must be derived from Monte Carlo. A and B depend only on the geometry of the TD and BD, and take into account the different area and response of the two detectors. This is demonstrated by their constant behaviour as a function of the parameters characterizing the showers, that is of energy, zenith angle, distance from the core and total signal.
The bias and the resolution of the reconstructed muon signal in the single scintillator is shown in the left panel of fig. 5.27. Minimal cuts have been

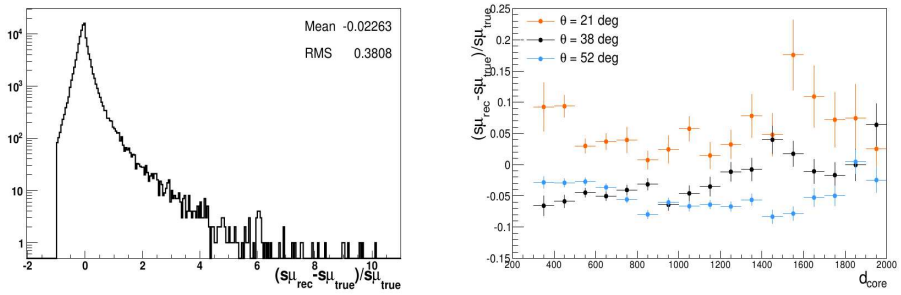

Figure 5.27: Left panel: The bias and the resolution in reconstructing the muon signal in a TOSCA detector. Right panel: the bias as a function of the core distance, for three different zenith angles.

applied in the present analysis, asking for a minimum detected signal in each detector $S_{BD} > 2$ VEM and $S_{TD} > 6$ VEM. If we make our cuts more demanding, by selecting i.e. all those events with $S_{BD} > 5$ VEM the signal resolution in each scintillator becomes better than 30% with a bias of 3%; however, such cuts obviously erase a lot of tanks in each event, compromising the muon size estimation. In the right panel of fig. 5.27 the same bias is shown as a function of the core distance, for three different zenith angles. No significant dependence on the core distance is found.
The distributions of the difference between the muon size reconstructed from the muonic signal obtained from the method described above and the simulated muon size for proton and iron likely showers are shown as an example in fig. 5.28 in the distance range 300-2000 m and in the energy range 19.7-19.9 log(E/eV). This is one of the two energy ranges in which we worked chosen by the Auger Collaboration to compare the peformances of the different proposed upgrade dectors in similar condition. The other bin considered is the low energy bin 18.9-19.1 log(E/eV). In this energy bin, the statistic is very low and the muon size resolutione is worse.
We studied as the muon reconstruction and its discriminating power change

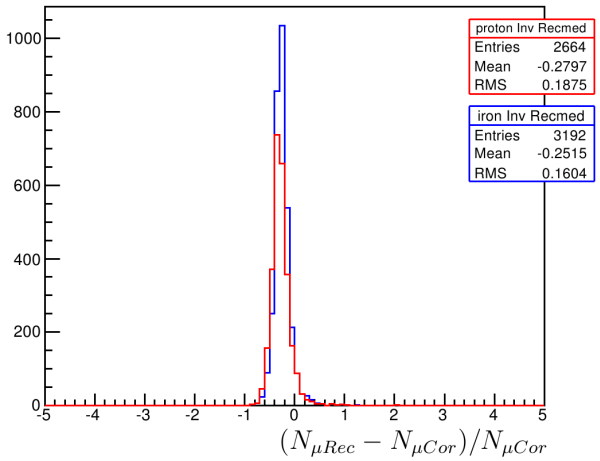

Figure 5.28: Distributions of the difference between the muon size reconstructed from the muonic signal obtained from the method described above and the simulated muon size for proton (red) and iron (blue) likely showers in the distance range 300-2000 m and in the energy range 19.7-19.9 log(E/eV). $N_{\mu Cor}$ is the muon size obtained fitting the lateral distribution of CORSIKA muons.

working in different distance range: 200-2000 m, 300-2000 m, and 500-2000 m. The muon size reconstruction improves when we use a larger distance range because the number of statios used in the fit is bigger and the fit better. Improving the resolution of the resolution of the muon size distributions, also the discriminating power of this variable increases. Anyway, we decided to work in the distance range 300-2000m becaus at 200 m from the shower core there may be saturation problems related to electronics also with this detector.

We tried to use a Fisher multivariate analysis to improve the proton-iron discrimination. Muon size was combined with SD variables as the curvature radius and the rise time, and with the variable SR3 ($SRb = \sum_i S_i \left(\frac{R_i}{R_{ref}}\right)^b, b = 3$) reconstructed from the scintillator muon signal S_i. R_i is the distance of the station from the shower core and R_{ref}=1000 m. The discrimanting power of this analysis is not very big as we can see from the fig. 5.29.

The biggest problem of the TOSCA-A detector is its small area. Too few muons are collected with 4 m^2. A lot of stations are not hit by muons or have a signal too low to assure a good reconstruction of the muon signal, so the reconstructed muon size, that is the more sensitive variable to mass composition, has not a resolution enough small to allow a good proton-iron discrimation.

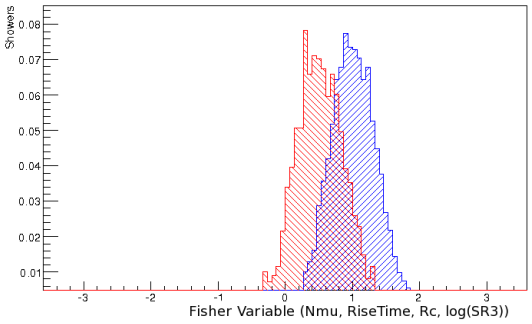

Figure 5.29: Fisher variable obtained combining muon size, log(SR3), rise time and radius of curvature.

5.5 MARTA: Photon Upper Limit

Among the aims of the Auger upgrade, there is also the improvement in photon sensitivity. In a search for photon primaries, a high discrimination from hadronic background and a high selection efficiency are the main ingredients. The upper limit on the flux of photons above a given energy is defined as:

$$\Phi_{CL}(E > E_{min}) = \frac{N_{\gamma}^{CL}(E_{\gamma} > E_{min}) \times \frac{1}{f} \times \frac{1}{\epsilon}}{A},$$

where N_{γ}^{CL} is the number of photon candidates with energy larger than E_{min} at a certain Confidence Level (CL), f is the photon selection efficiency, ϵ is the efficiency after the quality cuts, and A is the exposure of the detector. In collaboration with the Auger Lisbon group, an analysis was carried out to study the enhancements that the measurement of the muon component of an air shower, and in particular with the MARTA detector, leads to the search of photon primaries. The analysis ongoing in Lisbon is based on the reconstruction of the number of muons N_{μ} (truncated to the range between 500 to 2000 m distance to the shower axis) by looking at the RPC signal to obtain the local muon densities and integrating the fitted NKG-LDF function. In order to reduce the electromagnetic contamination, a fiducial area cut was applied to the detectors at distance to shower core below 1000 m, while for those further away the signal in the total RPC area is considered. Moreover, the ratio of the signal inside/outside the fiducial area with weights given by total hits in station was found to be a good variable for the discrimination between photons and protons. Fig. 5.30 on the left shows the asymmetry as function of the distance from the shower core for proton- and photon-induced showers with energies between 19-19.5 log(E/eV). On the right, instead, the asymmetry distributions for proton- and photon-induced showers with zenith angles between 0° and 40° are shown. In this angular

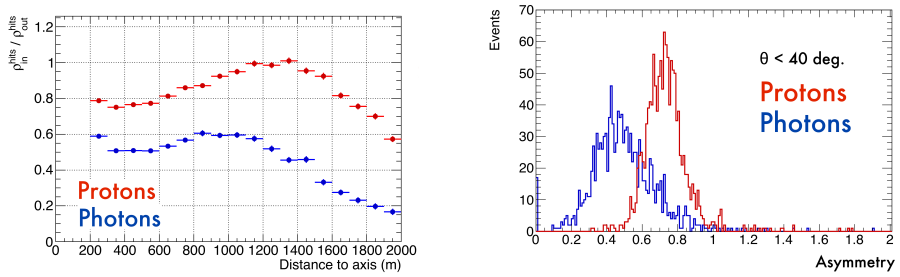

(a) (b)

Figure 5.30: **(a)** Asymmetry as function of the distance from the shower core for proton- and photon-induced showers with energies between 19-19.5 log(E/eV). **(b)** Asymmetry distributions for proton- and photon-induced showers with zenith angles between 0° and 40°.

range, asymmetry works better.
In this analysis, as hadronic background, a sample of only protons was considered to obtain a conservative result. Proton induced showers develop deeper and have less muons with respect to the other hadronic showers. Fig. 5.31 shows the elongation rate (left) and a scatter plot X_{max}-number of muons (right) for photon-, proton, and iron-induced showers. More details on electromagnetic and hadronic cascade was given in section 1.7.

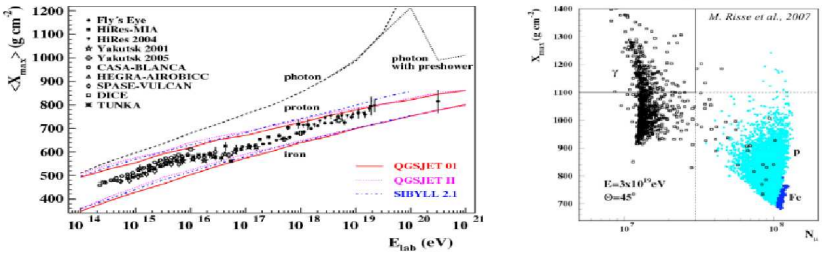

Figure 5.31: Elongation rate (left) and a scatter plot X_{max}-number of muons (right) for photon-, proton, and iron-induced showers.

Naples group produced simulated showers and performed a Fisher multivariate analysis to discriminate between proton and photon primaries.
The available MARTA dedicated simulations amount to 6000 photon and 6000 proton CORSIKA showers for each primary energy range considered: 18.5-19, 19-19.5, 19.5-20 log(E/eV). They were generated using QGSJET-II and EPOS1.99 as hadronic interaction models, with an energy spectrum E^{-1}, and zenith angles from 0° to 65°. Each shower was used six times, choosing the core position randomly in a region of 15 × 15 km^2 at the centre of the array. Each event was fully simulated and reconstructed with the MARTA Offline branch; simulation includes the full GEANT4 response of

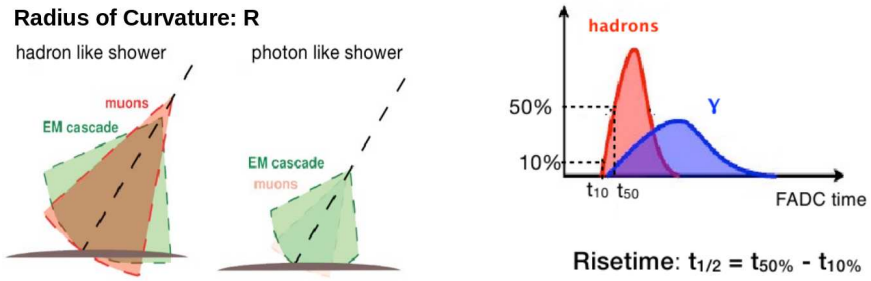

(a) (b)

Figure 5.32: Radius of curvature (a) and rise time (b) for hadron and photon like showers.

both tanks and RPCs. The simulated events are then reweighted to an $E^{-2.7}$ energy spectrum, that represent the Auger spectrum in the region between the ankle and the suppression.
Several multivariate analyses were performed combining variables obtained from the signal collected by the Auger tanks and from the MARTA RPC signal. Their discriminating power and efficiency were compared and the enhancements with respect the published Auger analysis on photon search with the SD data [16] were studied.
The SD analysis is based on two observables sensitive to the longitudinal shower development and to the muon content: the signal risetime, that is the time it takes to go from 10% to 50% of the total signal, and the curvature of the shower front. The radius of curvature for photon-initiated showers is smaller than that for hadronic showers, but the risetime is larger for deeper showers (section 1.7.1). These two variables are shown in fig. 5.32 for hadron and photon like showers. They are dependent on zenith angles, so in the published analysis they are theta corrected. In the multivariate analysis I performed to reproduce this analysis, I did not correct the rise time and radius of curvature, but added theta as discriminant variable. To a good rise time reconstruction, at least four tanks with a signal greater than 10 VEM are required, while for the radius of curvature (Rc) reconstruction, at least five tanks and a reduced chi-square from the fit to estimate below 10 are required. The SD analysis is restricted to primary energies ≥ 10 EeV and primary zenith angles of $30° - 60°$.
The most sensitive variable to mass composition obtained from RPC signal is the muon size. It is reconstructed with the method describe in section 5.3.4 considering the fiducial area. I worked on the optimization of the cuts required for a reasonable reconstruction of the muon size for proton- and photon-induced showers. First of all, the fit of the lateral distribution of the shower particles in the Auger tanks must have a reduced chi-square $\widetilde{\chi}^2_{LDF} \leq 10$ to assure a good reconstruction of the energy of the primary

particle. To a good reconstruction of the muon size, instead, at least four triggered RPC stations in the fit range [500,2000] m and a reduced chi-square of the MARTA lateral distribution fit $\widetilde{\chi}^{2MARTA}_{LDF} < 2$ are required. Fig. 5.33 shows the mean (upper panel) and the resolution (lower panel) of the gaussian distributions of the percentage difference between the reconstruction and simulated muon size as function of energy (0.2 log(E/eV) width bins) for photon-induced showers. Above $10^{18.6}$ eV, the mean is almost zero, while

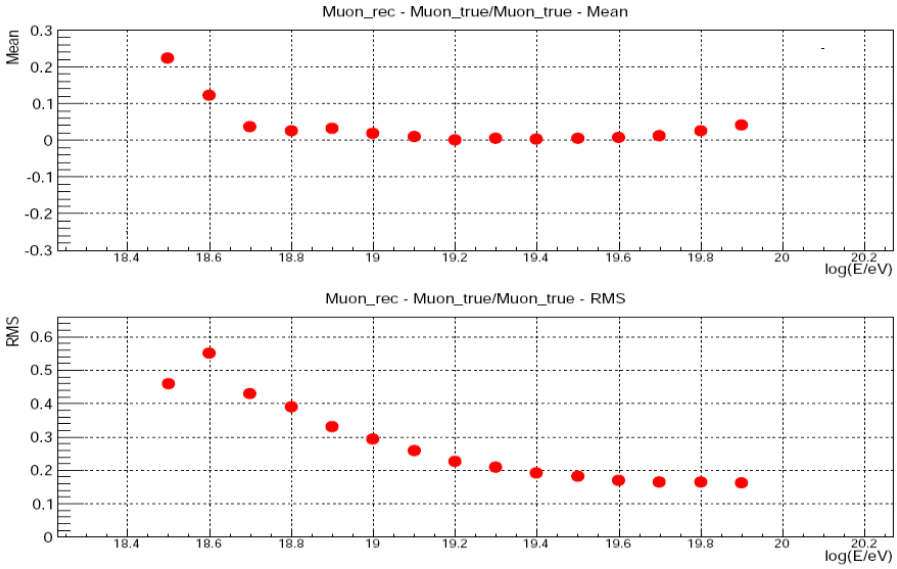

Figure 5.33: Mean (upper panel) and RMS (lower panel) of the gaussian distributions of the percentage difference between the reconstruction and simulated muon size as function of energy for photon-induced showers.

the RMS goes from 40% to 20%. The situation is very similar for proton-induced showers. The simulated muon size is calculated fitting the lateral distribution of CORSIKA muons at ground with the modified NKG in the range [500 m,2000 m].
The other variables obtained from the RPC signal are the asymmetry described above and $SR4$ defined as:

$$SR4 = \sum_i S_i \left(\frac{R_i}{R_{ref}} \right)^4 ,$$

where the sum runs over the triggered RPC stations, S_i is the signal recorded by the i-th station placed at a distance R_i from the hybrid shower core, and R_{ref} is a reference distance equal to 1000 m for this analysis. Distributions of muon size, asymmetry, and SR4 are shown in fig. 5.34 for proton and photon likely showers in the energy range 19.7-19.8 log(E/eV) and in the angular range 35°-45°.

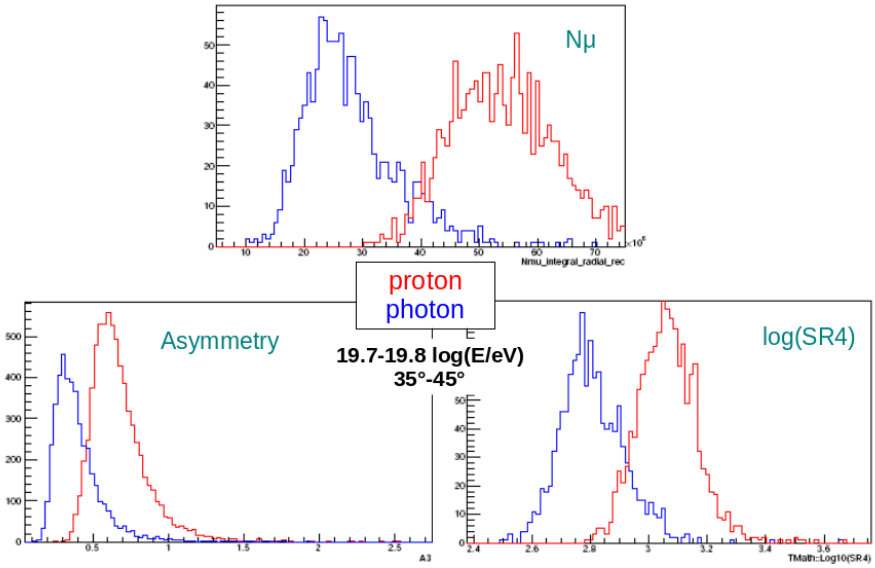

Figure 5.34: Distributions of muon size, asymmetry, and SR4 for proton and photon likely showers in the energy range 19.7-19.8 log(E/eV) and in the angular range 35°-45°

Thanks to the TMVA package provided by ROOT [1], multi-variable input information are condensed into a single scalar output variable, the Fisher variable in this analysis. The discrimination between signal and background is based on this variable. Fig. 5.35 shows the distribution of the Fisher variable obtained from one of the mutivariate analysis performed for signal (photons) and background (protons). The discriminating power of the

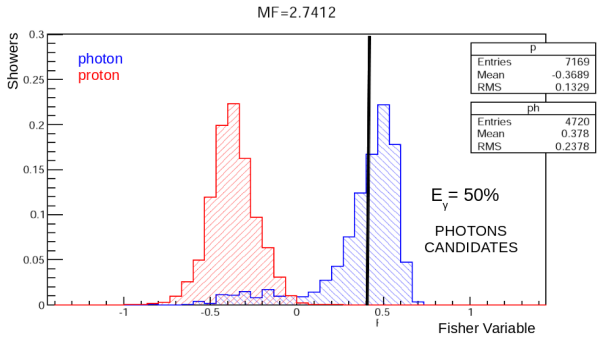

Figure 5.35: Distribution of Fisher variable for photons (blue) and protons (red) for the RPC only analysis in the energy bin log(E/eV) ∈ [19.3,19.4]. The set of variables used was N_μ, θ, and $S1000$.

[1] An object-oriented program and library for large scale data analysis developed by CERN.

analysis is evaluated with the Merit Factor (MF) defined as

$$MF = \frac{\overline{x}_s - \overline{x}_b}{\sqrt{\sigma_s^2 + \sigma_b^2}}, \tag{5.12}$$

where $\overline{x}_s$ and σ_s^2 are mean and RMS of the signal Fisher distribution and $\overline{x}_b$ and σ_b^2 are the corresponding quantities for the background.
The first three multivariate analysis were performed to study the effect that the MARTA detector sampling and electromagnetic contamination have on the muon size reconstruction, and so on the discriminating power of these analyses. Two variables are combined: muon size and $S1000$. The latter one, as seen in chapter 2, is reconstructed by the signal collected in the tank that is sensitive to the muon component, so $S1000$ is bigger for proton like showers. Fig. 5.36 shows the MF as function of energy for the analysis performed using the CORSIKA muon size (ideal case) in red, the muon size obtained from the CORSIKA muons injected in the RPCs in green, and the muon size from RPC signal in blue. The difference between red and green points

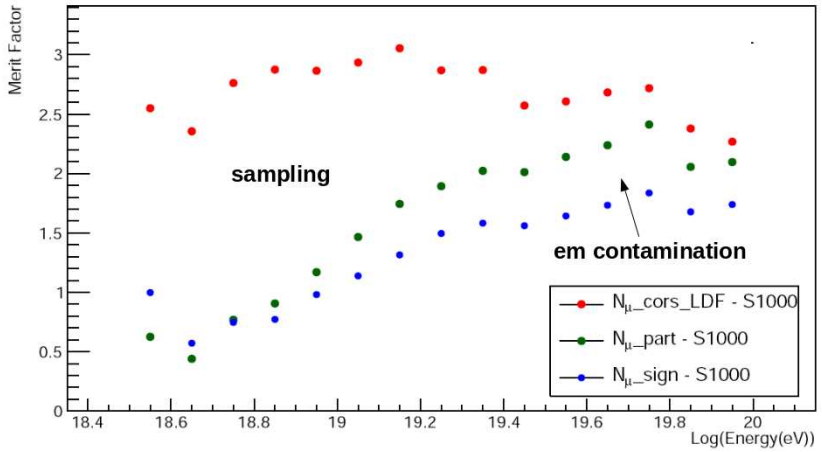

Figure 5.36: MF as function of energy for three Fisher analyses combining muon size and $S1000$. Red: CORSIKA muon size; green: muon size from the CORSIKA muons injected in the RPCs; blue: muon size from RPC signal.

is the detector sampling. The muon size is reconstructed worse when in the fit there are few stations and this happens at lower energies in particular. An array with a smaller spacing between stations would improve the muon size reconstruction, and so the proton-photon discrimination. Moreover, an additional shielding of the detector would produce a less contaminated signal and the discrimination would approach to the green case.
At this point, the asymmetry and SR4 were added as discriminating variable. Before they were added individually to the couple N_μ from RPC signal-$S1000$ of the previous analysis and then together. The MF obtained from these

analysis as function of energy are shown in fig. 5.37. Fig. 5.38 shows the efficiency curves for several variable combinations. In these analyses, also the

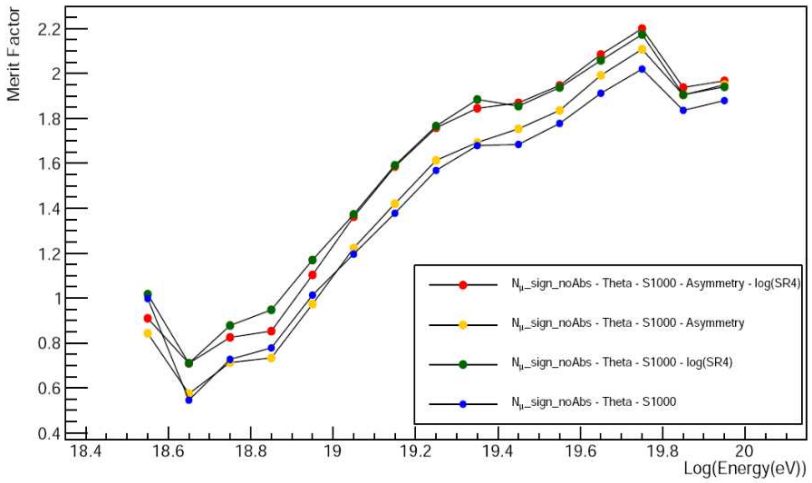

Figure 5.37: MF as function of energy for Fisher analyses performed to study the discriminating power of asymmetry and SR4.

zenith angle is used as discriminating variable. At high energies, it increases the photon-proton discrimination. Asymmetry adds discriminating power at energies above 10^{19} eV (see yellow markers (N_μ-θ-$S1000$-asymmetry) with respect to blue markers (N_μ-θ-$S1000$) in fig. 5.37), but it is not a strong variable with respect to SR4 (green markers (N_μ-θ-$S1000$-log(SR4))). Also the advantage of the analysis N_μ-θ-S1000-log(SR4)-asymmetry (red markers) in terms of MF is very small with respect to the analysis N_μ-θ-$S1000$-log(SR4) (green markers). Moreover, it is necessary to ask at least 5 stations with signal IN and OUT fiducial area, so the efficiency decreases as fig. 5.38 shows (cyan markers). Finally, asymmetry is not a very useful variable in photon search, while SR4 has a great discriminating power and its construction does not require particular conditions (red efficiency curve in fig. 5.38).
Fig. 5.39 represents a summary of the Fisher analyses performed. In the ideal case, muon size has a very big discriminating power (red markers in fig.5.39). In the real case, its discriminating power decreases because of the detector sampling (violet markers) and the residual electromagnetic component in the RPC signal (yellow markers). Using also log(SR4) in the Fisher analysis, MF increases again (green markers). The SD analysis perfomed using rise time and radius of curvature starts at a higher energy with respect to analyses performing with N_μ, but until $10^{19.1}$ its discriminating power (blue markers) is bigger than that one of the analysis N_μ^{RPC}-θ-$S1000$-log(SR4) (green markers). Above $10^{19.1}$, the two analyses are comparable in terms of MF, but the efficiency of the analysis N_μ^{RPC}-θ-$S1000$-log(SR4) (yellow curve in fig. 5.38) is very bigger than that one of the SD analysis (blue curve).

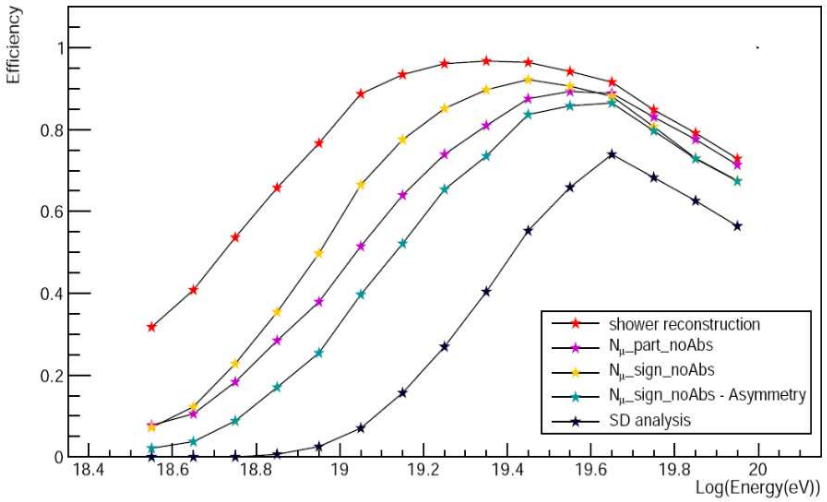

Figure 5.38: Efficiency curves for several variable combinations.

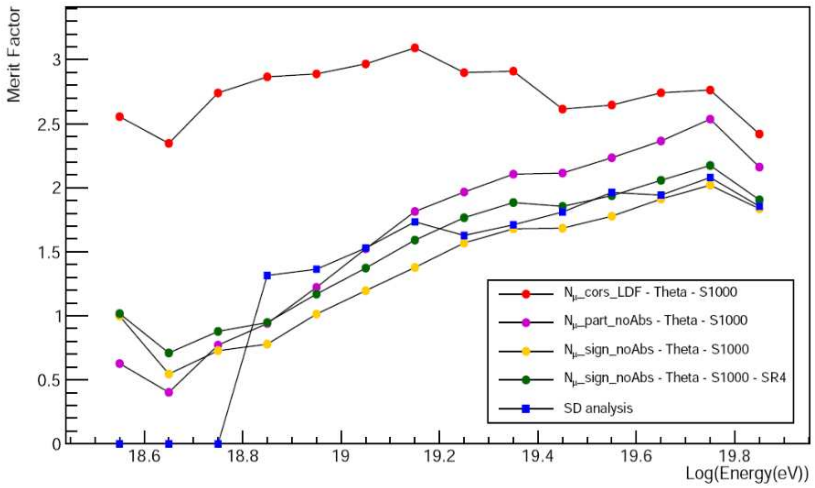

Figure 5.39: MF summary of the Fisher analyses performed using the simulated and reconstructed muon size and other variables obtained from signal in MARTA detector. Also the MF of the SD published analysis [16] is shown for comparison.

Therefore, we can conclude that MARTA detector could be used to put a stronger upper limit on the flux of photons.

Conclusions

This thesis mainly adresses to the measurement of the energy spectrum of light cosmic ray primaries with energies above 10^{18} eV. This measurements is very important because the energy-dependent elemental composition of cosmic rays is needed to distinguish among different theories on the origin of features observed in the all particle spectrum. Since the development of the extensive air showers is strictly related to the hadronic cross sections, that, at the Auger energies, can be only extrapoleted from the accelerators measurements, it is not easy to disentangle the mass composition from the influence of the hadronic models. Several hadronic interaction models exist corrisponding to different assumption on the hadronic interactions. Results obtained in this work are not independent of the particular choise of the model.
The energy spectrum of light primaries was constructed using hybrid data collected by the Pierre Auger Observatory from January 2004 to December 2013. Light elements, protons and helium nuclei, were selected with a cut on the depth of shower maximum, X_{max}, very sensitive to the mass composition, that is model dependent. Two hadronic models were used: Sibyll and EPOS_LHC. In both cases, the contamination of primaries heavier tha protons and helium nuclei is negligible, the Auger total spectrum is dominated by the light elements up to $10^{18.5}$ eV and , at this energy, a cutoff of the light component is observed. Finer details depend on the interaction model: in the case of Sibyll, protons with a possible small contamination of helium nuclei can account for the observed total flux, while EPOS_LHC, has some difficulties to reproduce the observed flux.
After 10^{19} eV, the light spectrum seems to flatten, but the fluctuations are too big due to the very low statistic, so no firm conclusion can be drawn about the shape of the light spectrum at these energies.
The statistics of the events collected by the Auger surface detector is higher, so an attempt was made to estimate a light spectrum using these events and the universality concept. In the universality approach, X_{max} can be reconstructed from the time trace of the signal collected by the water Cherenkov detectors. Several universality model were proposed in the Collaboration and they are still in a development phase. I used the reconstruction proposed by the Bariloche group. The reconstructed average X_{max} is very accurate. For

all models, a small overestimation of a few g/cm^2 is observed. This offset increases at high energies but it is always lower than 15 g/cm^2.
The SD light spectrum starts from $10^{18.8}$ eV and it was constructed from the events collected by the surface detector between 1 January 2004 and 31 November 2014. The X_{max} cut was optimized on simulations performed using EPOS_LHC as hadronic model. The SD light spectrum confirms the decrease of the light component with increasing energy and it is compatible with the hybrid light spectrum up to $10^{19.2}$ eV. Above this energy, it is hard to reconcile the two results, but the difference could be related to the offset of the reconstructed X_{max} as a function of the energy. This effect will be further investigated.
All mass sensitive analysis could be improved by the measurement of more mass sensitive observables. The number of muons in the shower, N_μ and the depth of the maximum of the muon production depth (MPD) distribution, X^μ_{max}, are the two most interesting variables. Present Auger tanks are sensitive to the muonic component, but they do not provide a direct measurement of the muons. The Auger Collaboration is defining a detector upgrade to achieve a reliable direct measurement of this component.
I performed a study on CORSIKA showers to test the possibility to reconstruct the MPD at the Auger energies using several methods proposed in the literature. A part from the experimental uncertainties, all proposed approaches were able to provide good reconstructions in a wide zenith angular range and the results were basically equivalent. Moreover, I tried to estimate the time resolution required to a muon detector for an accurate MPD reconstruction taking into account all the detector effects and experimental uncertainties. A time resolution beter than a few ns does not help since the uncertainty of the Auger reconstruction on the shower core spoiled the improvements of a better time resolution.
I also worked at the studying of the performances of two of the muon detectors proposed for the Auger upgrade.
I investigated the possibility to distinguish between proton and iron likely showers in TOSCA, which turned out to be too small to reconstruct the muons size with enough precision to have a satisfactory proton-iron discrimination.
Finally, I studied the performance of the MARTA RPC array in the search for primary photons. The muons size reconstructed from the signal in the RPCs has a good photon-proton discriminating power, especially combined with other variables defined from the RPC signal. This analysis has a discriminating power and an efficiency that could significantly improve present Auger upper limits on photon flux.

Bibliography

[1] Bruno Rossi, "Cosmic Rays", McGraw-Hill Book Company Inc. 1964

[2] J. Blümer, R. Engel, J. Hörandel, Prog. Part. Nucl. Phys., 63, 293 (2009)

[3] J. Abraham et al., Phys. Rev. Lett., 101, 061101 (2008)

[4] D. Allard, E. Parizot, E. Khan, S. Goriely, and A. V. Olinto, Astron. Astrophys. 443, L29 (2005)

[5] D. Allard, N. G. Busca, G. Decerprit, A. V. Olinto, and E. Parizot, JCAP 0810, 033 (2008), arXiv:0805.4779

[6] D. Hooper and A. M. Taylor, Astropart. Phys. 33, 151 (2010), arXiv:0910.1842

[7] A. M. Taylor, M. Ahlers, and F. A. Aharonian, Phys. Rev. D84, 105007 (2011), arXiv:1107.2055

[8] V. Berezinsky, A. Z. Gazizov, and S. I. Grigorieva, Phys. Rev. D74, 043005 (2006), hep-ph/0204357

[9] V. Berezinsky, A. Z. Gazizov, and S. I. Grigorieva, Phys. Lett. B612, 147 (2005), astro-ph/0502550

[10] T. Antoni, et al., KASCADE Collab., Astropart. Phys., 24, 1–25 (2005)

[11] E. Barcikowski et al. for the HiRes, Pierre Auger, Telescope Array and Yakutsk Collaborations, arXiv:1306.4430v1 [astro-ph.HE]

[12] A. Hillas, Annu. Rev. Astron. Astr., 22, 425 (1984)

[13] M. Kachelrieß, A. Vilenkin, Phys. Rev. Lett., 79, 4302 (1997)

[14] C. T. Hill, Nucl. Phys. B 224 (1983) 469

[15] G. Gelmini, O. Kalashev, D. Semikoz, J. Exp. Theor. Phys., 106, 1061-1082 (2008)

[16] Pierre Auger Collab., J. Abraham et al., Astropart. Phys., 27, 155 (2007), astro-ph/0606619

[17] Pierre Auger Collab., M. Settimo et al., Proc. of 32nd Int. Cosmic Ray Conf., Beijing, China 2, 55 (2011), arXiv:1107.4805

[18] Pierre Auger Collab., P. Pieroni, Proc. of 33rd Int. Cosmic Ray Conf., Rio de Janeiro, Brazil, arXiv:1307.5059

[19] The Pierre Auger Collaboration, Science, 318, 938 (2007)

[20] The Pierre Auger Collaboration, Astropart. Phys., 29, 188 (2008)

[21] The Pierre Auger Collaboration, Astroparticle Physics, 34, 314–326 (2010)

[22] IceCube Collab., R. Abbasi et al., Phys. Rev. D83, 092003 (2011), arXiv:1103.4250

[23] ANITA Collab., P. Gorham et al., Phys. Rev. Lett. 103, 051103 (2009), arXiv:0812.2715

[24] ANITA Collab., P. Gorham et al., Astropart. Phys. 32, 10 (2009), arXiv:0812.1920

[25] ANITA Collab., P. Gorham et al., Phys. Rev. D85, 049901 (2012), arXiv:1011.5004

[26] RICE Collab., I. Kravchenko et al., Phys. Rev. D85, 062004 (2012), arXiv:1106.1164

[27] HiRes Collab., R. U. Abbasi et al., Astrophys. J. 684, 790 (2008), arXiv:0803.0554 [astro-ph]

[28] E. Fermi, Phys. Rev., 75, 1169 (1949)

[29] K. Greisen, Phys. Rev. Lett., 16, 748-750 (1966)

[30] G.T. Zatsepin and V.A. Kuz'min, Journal of Experimental and Theoretical Physics Lett., 4, 78-80 (1966)

[31] M. Settimo, M. De Domenico, Astroparticle Physics, 62, 92-99 (2015)

[32] R. Engel, D. Heck, T.Pierog, Annu. Rev. Nucl. Part. S., 61, 467 (2011)

[33] A. Chen, J. Dwyer, and P. Kaaret, Astrophys. J., 463, 169 (1996); P. Sreekumar et al., Astrophys. J., 494, 523 (1998); P. Sreekumar, F. W. Stecker, and S. C. Kappadath, to appear in Proc. 4th Compton Symposium, Williamsburg (April 1997)

[34] Heck D, et al., Forsch. Karlsruhe Wiss. Ber., FZKA 6019. http://bibliothek.fzk.de/zb/berichte/FZKA6019.pdf (1998)

[35] Heitler W., "Quantum Theory of Radiation". Oxford: Oxford Univ. Press. 2nd ed. (1944)

[36] Matthews, J. Astropart. Phys., 22, 387 (2005)

[37] Meurer C, et al., Czech. J. Phys. A, 56, 211 (2006)

[38] F. Arqueros et al., Astron. Astroph., 359, 682 (2000)

[39] J. Fowler et al. (BLANCA Collab.), Astropart. Phys., 15, 49 (2001)

[40] O. Gress et al., Proc. of 25th Int. Cosmic Ray Conf., Durban 4 (1997) 129; Lubsandorzhiev, B. K. (for the TUNKA Collab.), Nucl. Instrum. Meth. A 595 (2008) 73

[41] J. Hinton, New Astronom. Rev., 48, 331 (2004)

[42] D. Ferenc, et al., Nucl. Instrum. Methods A, 553, 274 (2005)

[43] T. Weekes, et al., Astropart. Phys. 17, 221 (2002)

[44] S. Swordy, D. Kieda, Astropart. Phys. 13, 137 (2000)

[45] F. Arciprete, et al., Nuclear Phys. Proc. Suppl., 150, 186–189 (2006)

[46] M. Ave, et al., AIRFLY Collab., Nucl. Instrum. Methods A, 597, 41 (2008)

[47] T. Pierog, et al. in: Proc. 29th Int. Cosmic Ray Conf., Pune 7, 2005, p. 103

[48] Flys Eye Collaboration, D. J. Bird et al., Phys. Rev. Lett., 71, 3401 (Nov, 1993)

[49] The High Resolution Flys Eye Collaboration, R. U. Abbasi et al., Astrophys. J., 622, 910 (2005)

[50] H. Kawai, et al., TA Collab., Nuclear Phys. Proc. Suppl., 175–176, 221–226 (2008)

[51] M. Aglietta, et al., EAS-TOP Collab., Nucl. Instrum. Methods A, 336, 310 (1993)

[52] T. Antoni, et al., KASCADE Collab., Nucl. Instrum. Methods A, 513, 490 (2003)

[53] N. Chiba, et al., AGASA Collab., Nucl. Instrum. Methods A, 311, 338–349 (1992)

[54] G. Navarra, et al., KASCADE-Grande Collab., Nucl. Instrum. Methods A, 518, 207 (2004)

[55] Ranft J., Phys. Rev. D, 51, 64 (1995)

[56] Roesler S, Engel R, Ranft J., In Proceedings of the 27th International Cosmic Ray Conference, Hamburg, Ger. 2:439. Hamburg, Ger.: Int. Union Pure Appl. Phys. (2002); Bopp FW, Ranft J, Engel R, Roesler S., Phys. Rev. C, 77, 014904 (2008)

[57] Werner K, Liu FM, Pierog T., Phys. Rev. C, 74, 044902 (2006); Pierog T, Werner K., Nucl. Phys. Proc. Suppl., 196, 102 (2009)

[58] T. Pierog, Iu. Karpenko, J.M. Katzy, E. Yatsenko, K. Werner, arXiv:1306.0121 [hep-ph]

[59] Kalmykov NN, Ostapchenko SS, Pavlov AI., Nucl. Phys. Proc. Suppl. B, 52, 17 (1997); Kalmykov NN, Ostapchenko SS., Phys. Atom. Nucl., 56, 346 (1993)

[60] Ostapchenko S., Phys. Rev. D, 74, 014026 (2006); Ostapchenko S., Nucl. Phys. Proc. Suppl., 151, 143 (2006); Ostapchenko S. Am. Inst. Phys. Conf. Proc. 928:118 (2007)

[61] Ostapchenko S., Phys. Rev. D, 83, 014018 (2011)

[62] Engel J, Gaisser TK, Stanev T, Lipari P., Phys. Rev. D, 46, 5013 (1992)

[63] Ahn EJ, et al., Phys. Rev. D, 80, 094003 (2009)

[64] Fletcher RS, Gaisser TK, Lipari P, Stanev T., Phys. Rev. D, 50, 5710 (1994)

[65] Fesefeldt H., PITHA-85/02 (1985)

[66] Ferrari A, et al., CERN-2005-010 (2005)

[67] Bleicher M, et al., J. Phys. G: Nucl. Part. Phys., 25, 1859 (1999)

[68] The Pierre Auger Collaboration, Submitted to: Nucl.Instrum.Meth., FERMILAB-PUB-15-034-AD-AE-CD-TD, arXiv:1502.01323

[69] I. Allekotte et al. (Pierre Auger Collaboration), Nucl. Instr. and Meth. A, 586, 409 (2008)

[70] The Pierre Auger Collaboration, Nucl. Instr. Meth. Phys. Res. A, 613, 29-39 (2010)

[71] The Pierre Auger Collaboration, Nucl. Instr. Meth. Phys. Res. A, 620, 227-251 (2010)

[72] GEANT4 Collaboration, Nucl. Instr. and Meth. A, 506, 250-303 (2003)

[73] GEANT4 Collaboration, IEEE Transactions on Nuclear Science, 53, issue 1, 270-278 (2006)

[74] The Pierre Auger Collaboration, Astropart.Phys., 35, 591–607 (2012), arXiv:1201.2276, doi:10.1016/j.astropartphys.2011.12.002

[75] The Pierre Auger Collaboration, JINST, 8, P04009 (2013), arXiv:1303.5576, doi:10.1088/1748-0221/8/04/P04009

[76] M. Unger, B.R. Dawson, R. Engel, F. Schussler, R. Ulrich, Nucl. Instr. and Meth. A, 588, 433 (2008)

[77] M. Tueros, Pierre Auger Collaboration, "Estimate of the non-calorimetric energy of showers observed with the fluorescence and surface detectors of the Pierre Auger Observatory", in: Aab et al. [89], p. 11. arXiv:1307.5059

[78] V. Verzi, Pierre Auger Collaboration, "The Energy Scale of the Pierre Auger Observatory", in: Aab et al. [89], p. 7. arXiv:1307.5059.

[79] Darko Veberič and Markus Roth, "SD Reconstruction", GAP-2005-035

[80] C. Bonifazi, A. Letessier-Selvon, E. Santos, Pierre Auger Collaboration, Astropart. Phys., 28, 523–528 (2008). arXiv:0705.1856, doi:10.1016/j.astropartphys.2007.09.007

[81] J. Hersil, I. Escobar, D. Scott, G. Clark, S. Olbert, Phys. Rev. Lett., 6, 22–23 (1961). doi:10.1103/PhysRevLett.6.22

[82] R. Pesce, Pierre Auger Collaboration, "Energy calibration of data recorded with the surface detectors of the Pierre Auger Observatory": an update, in: Abreu et al. [90], p. 13. arXiv:1107.4809.

[83] A. Schulz, Pierre Auger Collaboration, "Measurement of the Energy Spectrum of Cosmic Rays above 3×10^{17} eV with the Pierre Auger Observatory", in: Aab et al. [89], p. 27. arXiv:1307.5059

[84] H. Dembinski, Pierre Auger Collaboration, "The Cosmic Ray Spectrum above 4×10^{18} eV as measured with inclined showers recorded at the Pierre Auger Observatory", in: Abreu et al. [90], p. 5. arXiv:1107.4809

[85] I. Valino, Pierre Auger Collaboration, "A measurement of the muon number in showers using inclined events recorded at the Pierre Auger Observatory", in: Aab et al. [89], p. 44. arXiv:1307.5059

[86] I. Maris, Pierre Auger Collaboration, "The AMIGA infill detector of the Pierre Auger Observatory: performance and first data", in: Abreu et al. [90], p. 9. arXiv:1107.4809

[87] D. Ravignani, Pierre Auger Collaboration, "Measurement of the energy spectrum of cosmic rays above 3×10^{17} eV using the AMIGA 750 m surface detector array of the Pierre Auger Observatory", in: Aab et al. [89], p. 4. arXiv:1307.5059

[88] S. Argiro, S. Barroso, J. Gonzalez, L. Nellen, T. C. Paul, et al., Nucl.Instrum.Meth. A, 580, 1485–1496 (2007). arXiv:0707.1652, doi:10.1016/j.nima.2007.07.010

[89] A. Aab, et al. (Eds.), The Pierre Auger Observatory: Contributions to the 33rd International Cosmic Ray Conference (ICRC 2013), 33rd International Cosmic Ray Conference (ICRC) 2013, Rio de Janeiro, Brazil, 2013. arXiv:1307.5059

[90] P. Abreu, et al. (Eds.), The Pierre Auger Observatory I: The Cosmic Ray Energy Spectrum and Related Measurements, 32nd International Cosmic Ray Conference (ICRC) 2011, Beijing, China, 2011. arXiv:1107.4809

[91] The Pierre Auger Collaboration, Astroparticle Physics, 34, issue 6, 368–381 (2011), arXiv:1010.6162 [astro-ph.HE]

[92] The Pierre Auger Collaboration, Phys.Rev. D, 90, 122005 (2014), arXiv:1409.4809 [astro-ph.HE]

[93] The Pierre Auger Collaboration, Phys.Rev. D, 90, 122006 (2014), arXiv:1409.5083 [astro-ph.HE]

[94] Linsley J, 1990 *6th Int. Symp.on Very High Energy Cosmic Ray Interactions (Turbes)* unpublished; 1991 *22nd Int.Cosm. Ray Conf. (Dublin)* p 873 (conference abstract)

[95] Danilova, Erlykin et al., J. Phys. G: Nucl. Part. Phys., 20, 961-978 (1994)

[96] Ambrosio, Aramo et al, J. Phys. G.: Nucl. Part. Phys. 23 (1997) 219-236

[97] Cazon et al., GAP-Note 2006-029

[98] Gamez PHD Thesis, GAP-Note 2011-104

[99] Ambrosio M., Aramo C., Cilmo M., Colalillo R., et al., EPJ Web Conf. 53 (2013) 08003, DOI:10.1051/epjconf/20135308003

[100] P. Billoir, Astroparticle Physics, 30, 270–285 (2008)